

Involute Working Group – Validation of CFD Turbulence Models for Steady-State Safety Analysis of Corner Geometry

Nuclear Science & Engineering Division

About Argonne National Laboratory

Argonne is a U.S. Department of Energy laboratory managed by UChicago Argonne, LLC under contract DE-AC02-06CH11357. The Laboratory's main facility is outside Chicago, at 9700 South Cass Avenue, Argonne, Illinois 60439. For information about Argonne and its pioneering science and technology programs, see www.anl.gov.

DOCUMENT AVAILABILITY

Online Access: U.S. Department of Energy (DOE) reports produced after 1991 and a growing number of pre-1991 documents are available free at OSTI.GOV (<http://www.osti.gov/>), a service of the U.S. Dept. of Energy's Office of Scientific and Technical Information.

Reports not in digital format may be purchased by the public from the National Technical Information Service (NTIS):

U.S. Department of Commerce
National Technical Information Service
5301 Shawnee Rd
Alexandria, VA 22312
www.ntis.gov
Phone: (800) 553-NTIS (6847) or (703)
605-6000 Fax: (703) 605-6900
Email: **orders@ntis.gov**

Reports not in digital format are available to DOE and DOE contractors from the Office of Scientific and Technical Information (OSTI):

U.S. Department of Energy
Office of Scientific and Technical Information
P.O. Box 62
Oak Ridge, TN 37831-0062
www.osti.gov
Phone: (865) 576-8401
Fax: (865) 576-5728
Email: **reports@osti.gov**
Disclaimer

Disclaimer

This report was prepared as an account of work sponsored by an agency of the United States Government. Neither the United States Government nor any agency thereof, nor UChicago Argonne, LLC, nor any of their employees or officers, makes any warranty, express or implied, or assumes any legal liability or responsibility for the accuracy, completeness, or usefulness of any information, apparatus, product, or process disclosed, or represents that its use would not infringe privately owned rights. Reference herein to any specific commercial product, process, or service by trade name, trademark, manufacturer, or otherwise, does not necessarily constitute or imply its endorsement, recommendation, or favoring by the United States Government or any agency thereof. The views and opinions of document authors expressed herein do not necessarily state or reflect those of the United States Government or any agency thereof, Argonne National Laboratory, or UChicago Argonne, LLC.

Involute Working Group – Validation of CFD Turbulence Models for Steady-State Safety Analysis of Corner Geometry

prepared by
C. Bojanowski, A. Bergeron, M. Sitek, and J. Licht

Nuclear Science & Engineering Division, Argonne National Laboratory

October 2021

(This page left intentionally blank)

Executive Summary

Worldwide, three research reactors have fuel plates curved as a circle-involute (a spiral generated around a circle):

- Oak Ridge National Laboratory High Flux Isotope Reactor located in Tennessee, U.S.A. [1],
- Institut Laue-Langevin High Flux Reactor located in Grenoble, France [2], and
- Technical University of Munich Research Neutron Source Heinz Maier-Leibnitz located in Garching, Germany [3].

All three reactors are currently using highly enriched uranium ($^{235}\text{U}/\text{U} \geq 20 \text{ wt}\%$) as fuel, and all three are actively engaged in activities to convert to low-enriched uranium ($^{235}\text{U}/\text{U} < 20 \text{ wt}\%$) fuel.

The operators of these reactors have expressed interest in using Computational Fluid Dynamics (CFD) tools to perform their Steady-State Thermal-Hydraulic (SSTH) safety calculations. Using CFD tools for SSTH analysis generally represents a significant departure from traditional methods and requires thorough verification and validation (V&V) to be accepted by regulators. Therefore, Argonne National Laboratory and the involute-reactor operators formed an informal group to help each other in this endeavor. This so-called Involute Working Group (IWG) aims at supporting the qualification of CFD tools for SSTH safety calculations. Activities include benchmarking, code-to-code comparison, and V&V, as well as technical support.

Qualifying CFD tools for involute-plate reactors implies providing solid justifications for the appropriateness of all aspects of the CFD analysis. For this type of application, one of the key requirements is to demonstrate the ability of CFD to model the fluid-flow and heat-transfer characteristics near the edge of coolant channels, where the minimum safety margins typically occur. While “classic,” one-dimensional thermal-hydraulic analysis typically makes use of empirical correlations (e.g., Dittus-Boelter, Sieder-Tate), CFD analyses rely on turbulence models and an appropriate discretization of the physical space (i.e., meshing) to characterize the flow and solid-to-liquid heat transfer.

As part of the IWG scope of work, the analysis presented in [4] focused on assessing the relevance of Reynolds Average Navier-Stokes (RANS) turbulence model choice for cladding/coolant heat-transfer analysis in the middle of the channel, away from the fuel edges. A comparison of results simulated with several turbulence models implemented in a commercial CFD code vs. the experimental data reported by Gambill and Bundy [5] was used for that purpose. The results showed a good agreement between CFD results and the experimental data, and close proximity to the well-known empirical correlation of Sieder-Tate and Hausen. The numerical results obtained with the use of the k-omega (KW) turbulence matched the experimental results particularly well, followed by the realizable k-epsilon (RKE) and Reynolds-Stress (RS) models.

The current study focuses on testing and validating the turbulence models in the corners of the coolant channel. For that purpose, initially, a set of analyses was performed with a simplified (flattened) single-plate model and coolant channels around it. Various positions of the fuel core within the plate were considered, and the effect of that geometrical change on the maximum predicted temperature in the cladding was studied. When the fuel core was less than two hydraulic diameters from the corner of the channel (side plate), the peak temperature started to increase. Subsequently, several experiments measuring the flow parameters in square and rectangular ducts were reviewed to select benchmark data for testing the turbulence models in the corners. It was

found that the historical journal articles and reports frequently lacked the raw data needed as input for equivalent numerical simulations. Thus, many landmark experiments had to be rejected as candidates for software validation benchmarks. This was especially true for the heated experiments. Ultimately, three experiments were selected for benchmarking:

1. Launder and Ying's isothermal experiment with air,
2. Melling and Whitelaw's isothermal experiment with water, and
3. Hirota et al.'s heated experiment with air heated via constant wall temperature.

The simulations of the isothermal experiments aimed at replicating the experimentally obtained velocity profiles that, in square ducts, are known to be affected by secondary flows. Although all tested turbulence models gave relatively good results, the linear eddy viscosity turbulence models (RKE and KW) were found to be less accurate, as they inherently describe turbulence in an isotropic fashion and are not able to capture some of the effects, like the mean flow distortions in the corners induced by secondary flows. The KW-QCR model, with quadratic terms, performed better than the above-mentioned linear models, but the best match between the simulated and experimental data was obtained with the RST elliptic blending (RST-EB) turbulence model.

The simulations of the heated experiment revealed some deficiencies of the RST-EB turbulence model that previously was giving a superior match with the experimental data. For coarser grids, this model significantly overpredicted the T^+ values. The performance of RST-QPS model for this case was also tested and the model provided closer match to the experimental data. However, RST-QPS model cannot be used universally for all near wall mesh sizes as it has only been implemented in STAR-CCM+ for high- y^+ wall treatment (that is using wall functions) without resolving the viscous-affected near-wall region.

Although all models struggled in replicating the isolines of velocity and temperature in the heated experiment, it was concluded that this problem may be due to the scaling of the raw data used in the original journal articles and lack of access to the raw data from these experiments. Some of the simulation setup parameters were also unknown and had to be assumed based on limited data.

Scaling of the results to the wall parameters y^+ , U^+ , and T^+ provides nondimensional data that should be insensitive to differences between assumed and actual input to the simulations. Simulations with almost all turbulence models were able to replicate the non-dimensional U^+ and T^+ experimental measurements, regardless of their ability to capture anisotropic effects of turbulence. A notable outlier was the KW-CUBIC model, which vastly overpredicted both quantities. The RST-EB turbulence model showed poor performance in predicting T^+ with the use of a coarse grid.

Overall, it can be stated that KW-QCR was the most universal turbulence model, giving good predictions of the isolines as well as velocity and temperature profiles in all three benchmarks. For the non-heated experiments, the RST-EB model provided the best match between the simulated and the experimental data. Based on the previous work [4], it provided consistently conservative results for wide ranges of Reynolds number in heated simulations. However, due the inconsistencies in the predicted results for the Hirota et al. heated experiment, it should be used with caution.

Abbreviations

CFD	Computational Fluid Dynamics
D_h	Hydraulic diameter
FRM II	Research Neutron Source Heinz Maier-Leibnitz
HEU	Highly enriched uranium
HFIR	High Flux Isotope Reactor
IWG	Involute Working Group
KE	k-epsilon
KW	k-omega SST
KW-CUBIC	KW SST with cubic terms
KW-QCR	KW SST with quadratic terms
LEU	Low-enriched uranium
RANS	Reynolds Average Navier Stokes
Re	Reynolds number
RHF	High Flux Reactor
RKE	Realizable KE turbulence
RS	Reynolds stress
RST-EB	RS transport turbulence with elliptic blending
RST-LPS2L	RS transport turbulence with linear pressure strain, two-layer model
RST-QPS	RS transport turbulence with quadratic pressure strain
SC model	Single channel model
SKE	Standard KE
SKE-CUBIC	Standard KE with cubic terms
SST	Shear stress transport
SSTH	Steady-state thermal-hydraulic
V&V	Verification and validation

Table of Contents

Executive Summary	i
Abbreviations	iii
Table of Contents	iv
List of Figures	v
List of Tables	ix
1 Introduction.....	1
1.1 Involute-Plate Reactors	1
1.2 Involute Working Group.....	5
1.3 Anisotropic Turbulence Effects in the Corners of Non-Circular Ducts	8
1.4 Initial Selection of Benchmark Experiments	9
2 Simulations of a Generic Fuel Plate	13
2.1 Base Simulations	13
2.2 Simulations with Shifted Fuel Core	20
3 Simulations of Launder and Ying’s Experiment	26
3.1 Description of Launder and Ying’s Experiment	26
3.2 Description of the CFD Model.....	27
3.3 Results	28
4 Simulations of Melling and Whitelaw’s Experiment	33
4.1 Description of the Experiment	33
4.2 Description of the CFD Model.....	34
4.3 Results	34
5 Simulations of the Experiment of Hirota et al.....	45
5.1 Description of the Experiment	45
5.2 Description of the CFD Model.....	49
5.3 Results	50
6 Conclusions	76
Acknowledgment	79
References	80
APPENDIX A: References for the Used Turbulence Models	83
APPENDIX B: Material Properties	84
B.1 Material Properties of Fuel and Cladding	84
B.2 Material Properties of Water.....	84
B.3 Material Properties of Air	87

List of Figures

Figure 1.1. From left to right, top view of the HFIR, RHF and FRM II fuel elements (close to true proportionality).	2
Figure 1.2. Detailed view of RHF fuel plates curved as involutes and welded between the two annular side-plates (photo is of a mockup and not a real element; the finish is therefore not representative of a real element).	2
Figure 1.3. Schematic representation (view from top) of an involute coolant channel modeled as a rectangle heated on both sides by two half fuel plates.	3
Figure 1.4. RHF power density distribution at beginning of cycle: (left) plate cross section; (right, top) lateral power density distribution at top, midplane, and bottom of the fuel; (right, bottom) axial power density distribution at the inner edge, mid-width and outer edge of the fuel.	4
Figure 1.5. Schematic representation (view from top) of an involute coolant channel modeled as a rectangle and divided into several independent sub-channels with unidimensional heat flux (noted as “q” on the figure).	6
Figure 1.6. Illustration of the effect of modeling heat conduction in one (blue curve) or three dimensions in conjunction with the unfueled regions (dark gray curve) on the heat flux at the coolant/cladding interface. Based on data from [15].	6
Figure 1.7. Secondary velocity patterns in non-circular cross sections [18].	8
Figure 1.8. Scaled velocity in the center of the duct in the benchmark experiments.	11
Figure 2.1. The geometry of the generic SC model of plate and coolant channel.	13
Figure 2.2. Side view of the SC model.	14
Figure 2.3. Power density distribution in the fuel (W/cm^3) at the (upper right) leading edge, (center right) middle, and (lower right) trailing edge of the plate.	15
Figure 2.4. Computational grid details for two near-wall densities: (left) $y^+ > 30$; (right) $1 < y^+ < 5$	16
Figure 2.5. The magnitude of (top) axial velocity and (bottom) in-plane velocities in generic CFD model with linear RKE turbulence model (units of m/s).	16
Figure 2.6. The magnitude of (top) axial velocity and (bottom) in-plane velocities in generic CFD model with KW-QCR (quadratic terms) turbulence model (units of m/s).	17
Figure 2.7. The magnitude of (top) axial velocity and (bottom) in-plane velocities in generic CFD model with RST-EB (elliptic blending) turbulence model (units of m/s).	17
Figure 2.8. The magnitude of in-plane velocities in a generic CFD model with (left) KW-QCR and (right) RST-EB turbulence models (units of m/s).	17
Figure 2.9. Locations of interest on the cladding-coolant interface for peak temperature and heat flux measurements.	18
Figure 2.10. Maximum heat flux on the cladding-coolant interface in generic CFD models: (left) full range and (right) close-up of the peak.	18
Figure 2.11. Maximum temperature at the cladding-coolant interface in generic CFD models: (left) full range and (right) close-up of the peak.	19
Figure 2.12. Maximum temperature at the cladding-coolant interface in generic CFD models, for models with (left) $y^+ > 30$ mesh (left) and (right) $1 < y^+ < 5$ mesh.	20

Figure 2.13. Heat flux in models with RKE turbulence and near-wall mesh size $y^+ > 30$.	21
Figure 2.14. Heat flux in models with KW-QCR turbulence and near-wall mesh size $y^+ > 30$.	21
Figure 2.15. Heat flux in models with RST-EB turbulence and near-wall mesh size $y^+ > 30$.	22
Figure 2.16. Temperature in models with RKE turbulence and near-wall mesh size $y^+ > 30$.	22
Figure 2.17. Temperature in models with KW-QCR turbulence and near-wall mesh size $y^+ > 30$.	23
Figure 2.18. Temperature in models with RST-EB turbulence and near-wall mesh size $y^+ > 30$.	23
Figure 2.19. Dependency of peak heat flux on the distance between the fuel edge and the side plate for various turbulence models.	24
Figure 2.20. Dependency of peak temperature at the cladding-coolant interface on the distance between the fuel edge and the side plate for various turbulence models.	24
Figure 3.1. (Left) Digitized axial velocity profiles in a smooth square duct (source [24]); (right) location of the cross sections of interest for velocity reporting.	26
Figure 3.2. Cross section through three computational grids used to model the duct in [24]: (left) 90 by 90 cells with near-wall element size of $y^+ 1$; (center) 70 by 70 cells with $1 < y^+ < 5$; (right) 50 by 50 cells with $y^+ > 30$.	27
Figure 3.3. Constant-velocity contours for near-wall mesh size of $y^+ 30$, compared to the experimental data, for (from top left) RST-EB, KW-QCR, RST-LPS2L, RKE, and KW models.	29
Figure 3.4. Axial velocity profiles for near-wall mesh size of $y^+ > 30$ compared to the experimental data for (from the top left) RST-EB, KW-QCR, RST-LPS2L, RKE, and KW models.	30
Figure 3.5. Axial velocity profiles for near-wall mesh size of $1 < y^+ < 5$ compared to the experimental data for (from the top left) RST-EB, KW-QCR, RST-LPS2L, RKE, and KW models.	31
Figure 3.6. Axial velocity profiles for near-wall mesh size of $y^+ < 1$ compared to the experimental data for (from the top left) RST-EB, KW-QCR, RST-LPS2L, RKE, and KW models.	32
Figure 4.1. (Left) Digitized experimental axial velocity profiles at $x/D_h = 29.0$ (source [26]), and (right) locations of the measurements.	33
Figure 4.2. Cross section through three meshes used to model the duct in [26]: (left) 90 by 90 elements with near-wall element size of $y^+ < 1$, (center) 70 by 70 elements with $1 < y^+ < 5$, (right) 50 by 50 elements with $y^+ > 30$.	34
Figure 4.3. Scaled velocity at the center of the duct for various turbulence models and $y^+ > 30$, compared to the experimental data.	35
Figure 4.4. Scaled velocity at the center of the duct for the RST-EB turbulence model and various mesh densities, compared to the experimental data.	36
Figure 4.5. Vector plot of secondary velocity field in the duct at $x/D_h = 36.8$ for the five indicated models.	37
Figure 4.6. Constant-velocity contours for near-wall mesh size of $y^+ > 30$ compared to the experimental data, for (from the top left) RST-EB, KW-QCR, RST-LPS2L, RKE, and KW models.	38
Figure 4.7. Constant-velocity contours for near-wall mesh size of $1 < y^+ < 5$ compared to the experimental data, for (from the top left) RST-EB, KW-QCR, RST-LPS2L, RKE, and KW models.	39
Figure 4.8. Constant-velocity contours for near-wall mesh size of $y^+ < 1$ compared to the experimental data, for (from the top left) RST-EB, KW-QCR, RST-LPS2L, RKE, and KW models.	40

Figure 4.9. Axial velocity profiles for near-wall mesh size $y^+ > 30$ compared to the experimental data, for (from the top left) RST-EB, KW-QCR, RST-LPS2L, RKE, and KW models.....	42
Figure 4.10. Axial velocity profiles for near-wall mesh size $1 < y^+ < 5$ compared to the experimental data, for (from the top left) RST-EB, KW-QCR, RST-LPS2L, RKE, and KW models.....	43
Figure 4.11. Axial velocity profiles for near-wall mesh size $y^+ < 1$ compared to the experimental data, for (from the top left) RST-EB, KW-QCR, RST-LPS2L, RKE, and KW models.....	44
Figure 5.1. Isolines in the testing section: (left) scaled velocity and (right) scaled temperature [29].	47
Figure 5.2. Mean primary flow velocity distribution in wall parameters [29].	47
Figure 5.3. Mean temperature distribution in wall parameters [29].	48
Figure 5.4. Locations of the data-gathering lines in the duct cross section for Ref. [29].	48
Figure 5.5. Cross-sections through the mesh used to model the duct in [29]: (left) fine, with $y^+ < 1$; (center) medium, with $1 < y^+ < 5$; and (right) coarse, with $y^+ > 30$.	50
Figure 5.6. Local wall heat flux on $1/8^{\text{th}}$ of the wall in models with near-wall mesh size $y^+ > 30$.	51
Figure 5.7. Constant velocity (left) and temperature (right) contours for near-wall mesh size of $y^+ > 30$ compared to the experimental data for the RKE turbulence model. Experiment - red dashed lines, CFD - black solid lines.	52
Figure 5.8. Constant velocity (left) and temperature (right) contours for near-wall mesh size of $y^+ > 30$ compared to the experimental data for the SKE-CUBIC turbulence model. Experiment - red dashed lines, CFD - black solid lines.	53
Figure 5.9. Constant velocity (left) and temperature (right) contours for near-wall mesh size of $y^+ > 30$ compared to the experimental data for the KW-QCR turbulence model. Experiment - red dashed lines, CFD - black solid lines.	53
Figure 5.10. Constant velocity (left) and temperature (right) contours for near-wall mesh size of $y^+ > 30$ compared to the experimental data for the KW-CUBIC turbulence model. Experiment - red dashed lines, CFD - black solid lines.	54
Figure 5.11. Constant velocity (left) and temperature (right) contours for near-wall mesh size of $y^+ > 30$ compared to the experimental data for the RST-EB turbulence model. Experiment - red dashed lines, CFD - black solid lines.	54
Figure 5.12. Constant velocity (left) and temperature (right) contours for near-wall mesh size of $y^+ > 30$ compared to the experimental data for the RST-QPS turbulence model. Experiment - red dashed lines, CFD - black solid lines.	55
Figure 5.13. Constant velocity (left) and temperature (right) contours for near-wall mesh size of $y^+ > 30$ compared to the experimental data for the RST-LPS2L turbulence model. Experiment - red dashed lines, CFD - black solid lines.	55
Figure 5.14. Constant-velocity contours for near-wall mesh size of $y^+ > 30$ compared to the experimental data, for the KW-QCR turbulence model scaled by (left) the lowest center velocity, (center) the average center velocity, and (right) the highest center velocity. Experiment - red dashed lines, CFD - black solid lines.	57
Figure 5.15. Constant-temperature contours for near-wall mesh size of $y^+ > 30$ compared to the experimental data, for the KW-QCR turbulence model scaled by (left) the lowest center temperature, (center) the average center temperature, and (right) the highest center temperature. Experiment - red dashed lines, CFD - black solid lines.	58

Figure 5.16. Computational grid with $y^+ > 30$ overlaid with the digitized experimental velocity isolines [29].	59
Figure 5.17. U + in simulations with the RKE turbulence model and near-wall cell size (a) $y^+ < 1$, (b) $y^+ < 5$, and (c) $y^+ > 30$, as compared to the experimental data.	61
Figure 5.18. U + in simulations with the SKE-CUBIC turbulence model and near-wall cell size (a) $y^+ < 1$, (b) $y^+ < 5$, and (c) $y^+ > 30$, as compared to the experimental data.	62
Figure 5.19. U + in simulations with the KW-QCR turbulence model and near-wall cell size (a) $y^+ < 1$, (b) $y^+ < 5$, and (c) $y^+ > 30$, as compared to the experimental data.	63
Figure 5.20. U + in simulations with the KW-CUBIC turbulence model and near-wall cell size (a) $y^+ < 1$, (b) $y^+ < 5$, and (c) $y^+ > 30$, as compared to the experimental data.	64
Figure 5.21. U + in simulations with the RST-LPS2L turbulence model and near-wall cell size (a) $y^+ < 1$, (b) $y^+ < 5$, and (c) $y^+ > 30$, as compared to the experimental data.	65
Figure 5.22. U + in simulations with the RST-EB turbulence model and near-wall cell size (a) $y^+ < 1$, (b) $y^+ < 5$, and (c) $y^+ > 30$, as compared to the experimental data.	66
Figure 5.23. U + in simulations with the RST-QPS turbulence model and near-wall cell size $y^+ > 30$, as compared to the experimental data.	67
Figure 5.24. T + in simulations with the RKE turbulence model and near-wall cell size (a) $y^+ < 1$, (b) $y^+ < 5$, and (c) $y^+ > 30$, as compared to the experimental data.	69
Figure 5.25. T + in simulations with the SKE-CUBIC turbulence model and near-wall cell size (a) $y^+ < 1$, (b) $y^+ < 5$, and (c) $y^+ > 30$, as compared to the experimental data.	70
Figure 5.26. T + in simulations with the KW-QCR turbulence model and near-wall cell size (a) $y^+ < 1$, (b) $y^+ < 5$, and (c) $y^+ > 30$, as compared to the experimental data.	71
Figure 5.27. T + in simulations with the KW-CUBIC turbulence model and near-wall cell size (a) $y^+ < 1$, (b) $y^+ < 5$, and (c) $y^+ > 30$, as compared to the experimental data.	72
Figure 5.28. T + in simulations with the RST-LPS2L turbulence model and near-wall cell size (a) $y^+ < 1$, (b) $y^+ < 5$, and (c) $y^+ > 30$, as compared to the experimental data.	73
Figure 5.29. T + in simulations with the RST-EB turbulence model and near-wall cell size (a) $y^+ < 1$, (b) $y^+ < 5$, and (c) $y^+ > 30$, as compared to the experimental data.	74
Figure 5.30. T + in simulations with the RST-QPS turbulence model and near-wall cell size $y^+ > 30$, as compared to the experimental data.	75

List of Tables

Table 1.1. Key parameters of fuel elements in involute reactors.	3
Table 1.2. Key thermal-hydraulic parameters in involute reactors.....	3
Table 1.3. Description of the candidate benchmark experiments.	12
Table 2.1. Distance between the fuel core and the side plate in the analyzed cases.....	14
Table 5.1. Uncertainties in the heated-duct experiments of Hirota et al. and Fujita et al.....	45
Table 5.2. Matrix of runs for the simulations of the experiment of Hirota et al. [29].....	50
Table 5.3. Comparison of the center velocity in the experiment and simulations from models with wall $y^+ > 30$ and various turbulence models.....	56
Table 5.4. Comparison of the center temperature in the simulations from models with wall $y^+ > 30$ and various turbulence models.	57
Table 6.1. Summary of turbulence models used in simulations of each experiment and their qualitative performance	78

(This page left intentionally blank)

1 Introduction

There are three research reactors in the world having fuel plates curved as a circle-involute (a spiral generated around a circle):

- Oak Ridge National Laboratory High Flux Isotope Reactor (HFIR) located in Tennessee, U.S.A. [1],
- Institut Laue-Langevin High Flux Reactor (RHF) located in Grenoble, France [2], and
- Technical University of Munich Research Neutron Source Heinz Maier-Leibnitz (FRM II) located in Garching, Germany [3].

All three reactors are currently using highly enriched uranium (HEU, $^{235}\text{U}/\text{U} \geq 20$ wt. %) as fuel, and all three are actively engaged in activities to convert to low-enriched uranium (LEU, $^{235}\text{U}/\text{U} < 20$ wt. %) fuel.

The operators of these reactors have expressed interest in using Computational Fluid Dynamics (CFD) tools to perform their Steady-State Thermal-Hydraulic (SSTH) safety calculations. Using CFD tools for SSTH analysis generally represents a significant departure from traditional methods and requires thorough verification and validation (V&V) to be accepted by regulators. Therefore, Argonne National Laboratory and the involute reactors formed an informal group to help each other in this endeavor. This so-called Involute Working Group (IWG) aims at supporting the qualification of CFD tools for SSTH safety calculations. Activities include benchmarking, code-to-code comparison, and V&V, as well as technical support.

Qualifying CFD tools for involute-plate reactors implies providing solid justifications for the appropriateness of all aspects of the CFD analysis. For this type of application, one of the key requirements is to demonstrate the ability of CFD to model the fluid flow and heat transfer characteristics near the edge of coolant channels, where the minimum safety margins typically occur. While “classic,” one-dimensional thermal-hydraulic analysis typically makes use of empirical correlations (e.g., Dittus-Boelter [6], Sieder-Tate [7]), CFD analyses rely on turbulence models and an appropriate discretization of the physical space (i.e., meshing) to characterize the flow and solid-to-liquid heat transfer.

1.1 Involute-Plate Reactors

The fuel elements of involute-plate reactors have an annular shape, as depicted in Figure 1.1, which shows a top view, from left to right, of the HFIR, RHF, and FRM II fuel elements. HFIR has two concentric elements, while RHF and FRM II have only one. For each of the reactors, the fuel elements must be replaced at every new core cycle. Figure 1.2 provides a more detailed view of the RHF plates and channels. As one can see in this figure, the fuel plates, curved as involutes, are attached (welded) to two concentric tubes (commonly referred to as side-plates). The space between two adjacent fuel plates forms a coolant channel through which water passes at substantial velocity (~ 15 m/s) to evacuate the heat generated in the fuel plates by nuclear reactions.

The fuel plates are very thin (1.27–1.36 mm) and have a sandwich composite type structure. The fuel is made of HEU (93 wt%) mixed with aluminum. The fuel core is surrounded by aluminum alloy cladding on each side. RHF uses heavy water as coolant, while FRM II and HFIR use light water. The coolant flows from top to bottom in all three reactors. More information on these reactors and fuel elements can be found in Table 1.1, Table 1.2 and references listed in these tables.

The involute shape of the plates allows for:

- the thickness of a coolant channel to be constant from the inner to the outer edge of the element,
- all the channels to be identical (granted some local deviations introduced during the manufacturing process), and
- all the fuel plates to experience very similar irradiation conditions (granted some possible local azimuthal variations induced by the presence of safety or experimental components located in the vicinity of the fuel elements).

These features are particularly advantageous for SSTH analysis, since it requires modeling only one or a few channels, and not all of them, to characterize the entire element. Moreover, one could argue that the constant channel thickness allows for modeling of the involute-shaped channel as a simple rectangular channel heated on both sides, as depicted in Figure 1.3. This simplistic approach is particularly suited for low-level modeling (i.e., one-dimensional heat transfer) but may miss second-order effects (e.g., concave/convex heat-flux distribution, non-straight corners) and may therefore tend to lead to conservative results. As part of the IWG scope of work, the plan is to study the differences between a straight and an involute-plate channel in more depth under a separate activity.



Figure 1.1. From left to right, top view of the HFIR, RHF and FRM II fuel elements (close to true proportionality).



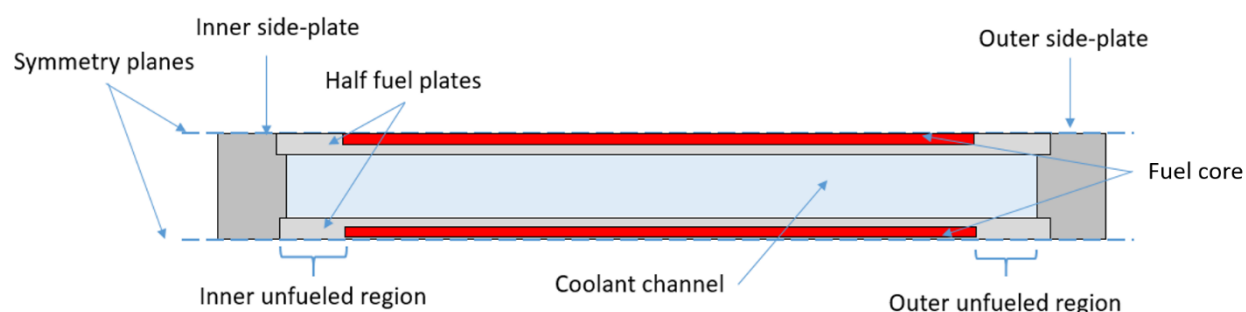
Figure 1.2. Detailed view of RHF fuel plates curved as involutes and welded between the two annular side-plates (photo is of a mockup and not a real element; the finish is therefore not representative of a real element).

Table 1.1. Key parameters of fuel elements in involute reactors.

Parameters	HFIR [8]	RHF [9]	FRM II [10]
Fuel type	U_3O_8 / Al	UAl_x / Al	U_3Si_2 / Al
Number of elements	2	1	1
Number of plates	540 (171+369)	280	113
Plate thickness (mm)	1.27	1.27	1.36
Plate length (cm)	60.96	90.30	72.00
Channel width between side plates (cm)	8.548 / 7.679	7.594	6.940
Channel thickness (mm)	1.27	1.80	2.20
Cladding thickness (mm)	0.254	0.380	0.380
Meat thickness (mm)	Varies along width, max: 0.693	0.51	0.60
Meat width (cm)	7.798 / 7.087	6.734	6.240
Width of inner unfueled region (from outer radius of inner side-plate to inner fuel radius, cm)	0.234 / 0.218	0.314	0.259
Width of outer unfueled region (from outer fuel radius to inner radius of outer side-plate, cm)	0.516 / 0.374	0.547	0.441

Table 1.2. Key thermal-hydraulic parameters in involute reactors.

Parameter	HFIR [11]	RHF [12]	FRM II [13]
Average coolant velocity (m/s)	15.5	17	15.9
Nominal inlet / outlet bulk temperature (Celsius)	49 / 69	30 / 50	38 / 53
Nominal inlet / outlet pressure (Bar)	33.3 / 25.72	14 / 4	8.8 / 2.3
Reynolds number, Re	$\sim 100,000$	$\sim 100,000$	$\sim 100,000$
Peak heat flux (W/cm^2)	< 400	< 400	382.3

**Figure 1.3. Schematic representation (view from top) of an involute coolant channel modeled as a rectangle heated on both sides by two half fuel plates.**

The fuel element is located at the center of a larger vessel that contains the reflector (heavy water for RHF and FRM II, beryllium for HFIR) as well as experimental and safety devices. The cylindrical volume located at the center of the annular fuel elements is often referred to as the central cavity. FRM II and RHF use this space for the control elements, which move vertically to control the reactivity during each cycle. HFIR uses this central cavity for isotope production. HFIR reactivity control is ensured by an inner and outer shroud located near the outer edge of the outer element.

Owing to these geometric characteristics, fast neutrons generated from fission thermalize in the reflector and the central cavity. Because the fuel plates are “edge-on,” thermalized neutrons that come

back to the fuel elements tend to be captured more frequently on the edges of the fuel, where more fissions, and therefore more heat, will be generated. This behavior leads to a non-uniform distribution of power within the plates, where the power tends to spike at the edges. To illustrate this point, Figure 1.4 shows a typical power density distribution within the fuel of an RHF plate at beginning of an irradiation cycle. It can be noted that large power gradients exist, and for this reactor, the fuel outer edge is where the limiting safety margin typically occurs.

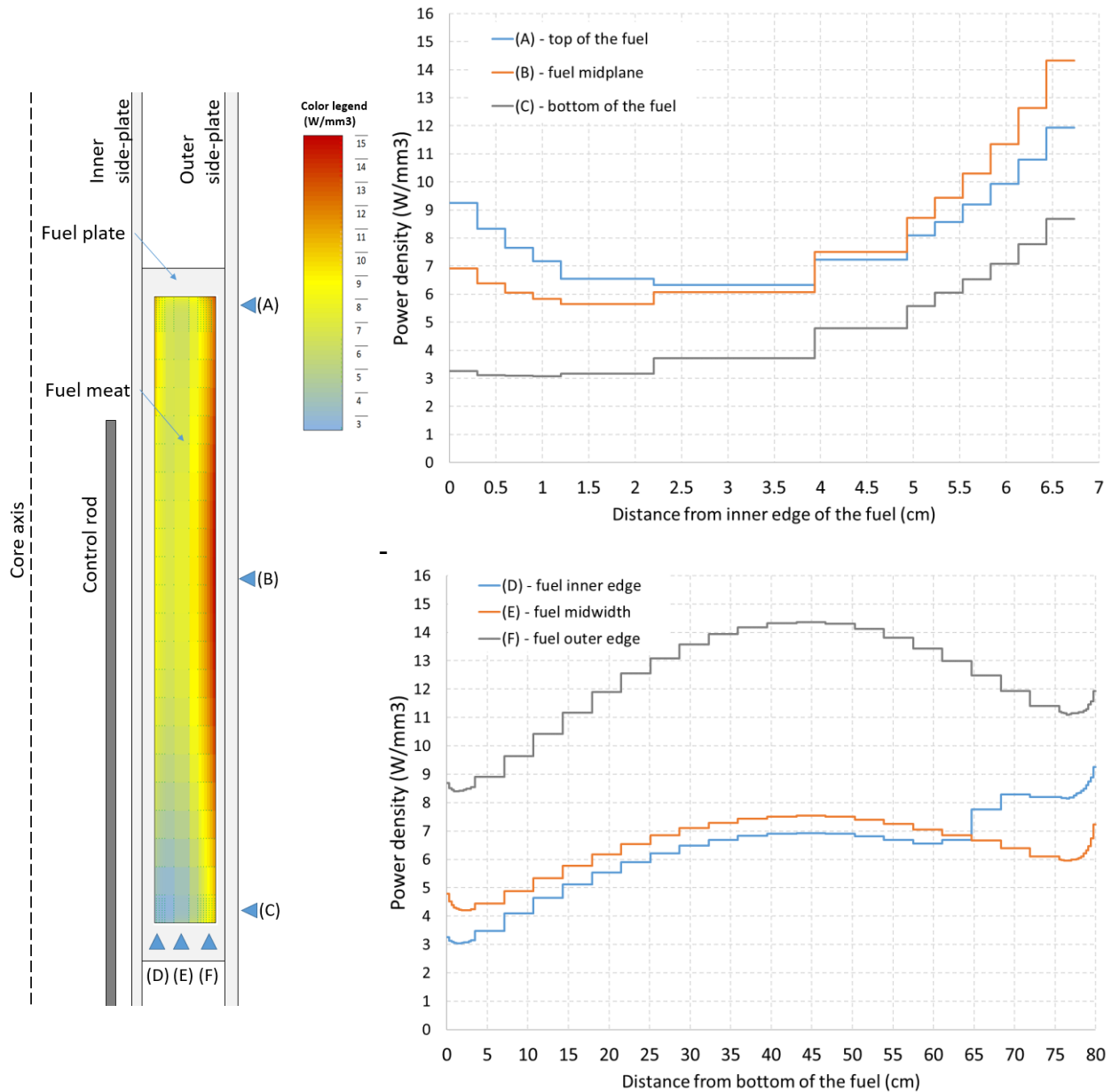


Figure 1.4. RHF power density distribution at beginning of cycle: (left) plate cross section; (right, top) lateral power density distribution at top, midplane, and bottom of the fuel; (right, bottom) axial power density distribution at the inner edge, mid-width and outer edge of the fuel.

1.2 Involute Working Group

Historically, SSTH analysis is carried out using simple but conservative methods in which the coolant channel is divided into several independent sub-channels (no energy exchange between sub-channels). Heat, in this simplified representation, comes only from the direction normal to the plates, as illustrated in Figure 1.5. Lateral and axial heat conduction, heat-induced mass flow redistribution, or the effect of the unfueled region is often ignored, leading to a relatively conservative physical representation of the heat transfer in the coolant channel. This representation, in turn, results in a relatively conservative estimation of the safety margin.

In the framework of non-proliferation policies, the international community aims at eliminating the use of HEU fuel in civilian facilities such as research reactors [14]. Many organizations worldwide are developing high-density LEU fuel to replace the HEU fuel. All three involute reactor operators are actively engaged in the conversion to LEU as well.

Conversion to LEU implies changing the fuel design and therefore changing the material properties, which influence the thermal-hydraulic behavior of the elements. In many cases, it also implies making geometric modifications to the fuel element (plate and channel gap thickness, and other geometric parameters), which also affect the thermal-hydraulic performance of the fuel elements. LEU fuels are denser than HEU fuels, power peaking is typically aggravated for this type of fuel, increasing the heat flux on the cladding to coolant interface and therefore reducing safety margins. The conversion-related thermal-hydraulic analysis revealed that the legacy codes lack the flexibility to model some of the effects of the described changes

To overcome these limitations, the three involute-reactor operators expressed interest in using CFD codes to perform their thermal-hydraulic safety calculations. These simulation tools can model virtually any kind of geometry and also can model complex physical phenomena more accurately than the currently used legacy codes. This ability can eliminate some unnecessary conservatism inherently present with legacy methods and can recover some of the safety margin losses.

For instance, the ability of CFD to easily model the unfueled region of the plates and to model heat conduction in three dimensions allowed quantifying the amount of heat transferred to the unfueled regions of the plate [15]. It was shown that a non-negligible fraction of heat is conducted through these unfueled regions, which in turn causes a substantial decrease of the heat flux at the cladding to coolant interface near the fuel edges, as illustrated in Figure 1.6. Because the fuel edges are often the regions of the plates having less margin to boiling-related phenomena, the decreased heat flux tends to increase the safety margins substantially.

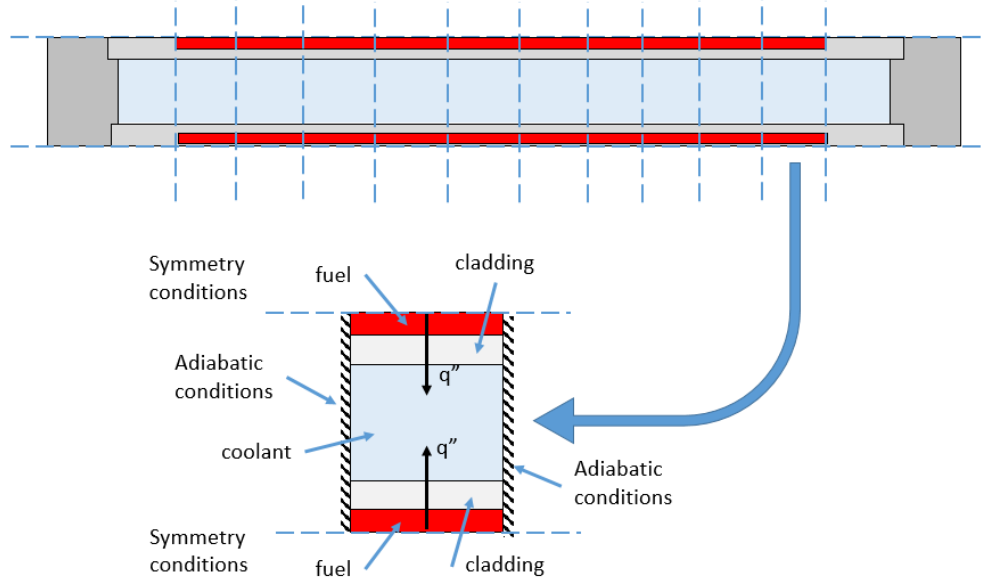


Figure 1.5. Schematic representation (view from top) of an involute coolant channel modeled as a rectangle and divided into several independent sub-channels with unidimensional heat flux (noted as “q” on the figure).

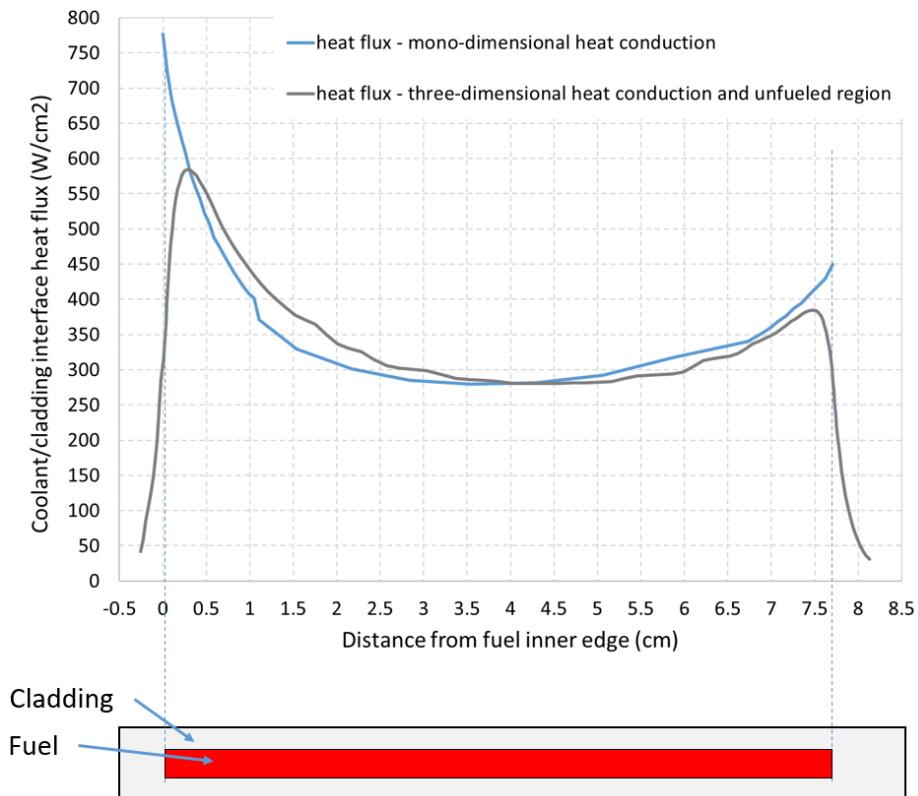


Figure 1.6. Illustration of the effect of modeling heat conduction in one (blue curve) or three dimensions in conjunction with the unfueled regions (dark gray curve) on the heat flux at the coolant/cladding interface. Based on data from [15].

Using CFD for SSTH analysis represents, however, a significant departure from traditional methods and requires thorough V&V to be accepted by regulators. Therefore, Argonne National Laboratory and the operators of the involute reactors formed an informal group to help each other in this endeavor. The IWG aims at, among other goals, supporting the qualification of CFD tools for thermal-hydraulic safety calculations [15], [16]. Activities include benchmarking, code-to-code comparison, and V&V, as well as technical support.

As part of the IWG scope of work, the analysis presented in [4] focused on assessing the relevance of the RANS turbulence model choice to the cladding/coolant heat transfer analysis in the middle of the channel away from the fuel edges. The following three turbulence models were tested in the CFD model of the Gambill and Bundy experiment [5] (see Appendix A):

- RKE (Realizable k-epsilon model with two-layer all-y+ wall treatment),
- KW Menter's SST k-omega model with all-y+ wall treatment), and
- RST-EB (Reynolds Stress elliptic blending with all-y+ wall treatment).

Overall, it was concluded that the selected turbulence models were able to accurately represent the heat transfer of involute-plate reactors. The CFD results displayed a good agreement with the experimental data, and a close proximity to the well-known empirical correlations of Sieder-Tate and Hausen. The results obtained with the KW turbulence model matched the experimental results particularly well, followed by the RKE and RST-EB models, both of which tended to predict more conservative results.

To account for lowering the uranium enrichment without changing the coolant channel gap thickness, wider and thicker fuel cores within the plates were proposed in the LEU designs. This change may translate into even larger power peaking near the channel edges, and safety margin reduction. Thus, it is important to model this region in CFD accurately, as it informs design and fuel specifications regarding the influence of core changes on the safety margins of boiling-related phenomena.

Flow in the corners of non-circular straight ducts is characterized by distortions of the mean velocity field in cross sections perpendicular to the mean flow direction towards the corners. These distortions are caused by secondary flows of the second kind, which are a result of the three-dimensionality of the flow, which in turn results from the anisotropy of the Reynolds stress tensor (see Section 1.3 for details and references). The main goal of the present study is to test turbulence models commonly implemented in commercial software (e.g., KW, KE, and RS), and to assess their relevance in capturing these fluid flow characteristics near coolant channel edges in involute-plate reactors.

To compare the performance of various turbulence models under such conditions, a generic CFD model of a fuel plate and coolant was built, with five positions of the fuel with respect to the side plate distance. For this purpose, the previously developed CFD model in [17] was used. The assumed power profile in the plate had a shape characteristic of involute reactor plates. The channel geometry and the flow conditions were representative of involute reactor conditions, but both the plate and the channels were represented as flat. This is a greatly simplifying assumption, but the model was sufficient to study the phenomena of interest, meaning turbulence modeling in CFD and its influence on the cladding temperature distribution and therefore on the safety margins.

Subsequently, to validate these turbulence models, simulations of five historical experiments of flow in square and rectangular ducts were performed. The simulation results of three of these experiments, two isothermal and one heated study, are presented in this report.

1.3 Anisotropic Turbulence Effects in the Corners of Non-Circular Ducts

Secondary flows and their influence on axial velocity contours in straight rectangular and square ducts were first noticed almost a century ago by Prandtl [18] and his student Nikuradse [19]. Nikuradse studied velocity distributions in fully developed turbulent flows of water in non-circular ducts. They were the first to present, for ducts with rectangular and triangular cross sections, velocity isolines that followed the shape of the ducts instead of being rounded as for the laminar flows, indicating larger than expected mean velocity in the corners [19]. However, this work did not provide a complete explanation of the origins of these distortions. Prandtl was the first to identify “secondary motions” that are superimposed on the primary axial flows in uniform non-circular channels. These motions, according to his description, force the fluid to flow along the line dividing the corner into two halves (bisectors) and towards the corner on both sides of that line [18]. Subsequently, the fluid is transported away from the corners along the walls and then back to the center of the channel, near the middle of all three walls in triangular ducts and the short walls in rectangular ducts. Similarly, vorticity and energy are transported from the center of the duct to the corners. These secondary flow patterns are shown schematically in Figure 1.7, which is based on Prandtl’s original work [18]. Further experimental work, including [20], [21] and [22], confirmed the conclusions of Nikuradse and Prandtl about the existence of secondary flows.

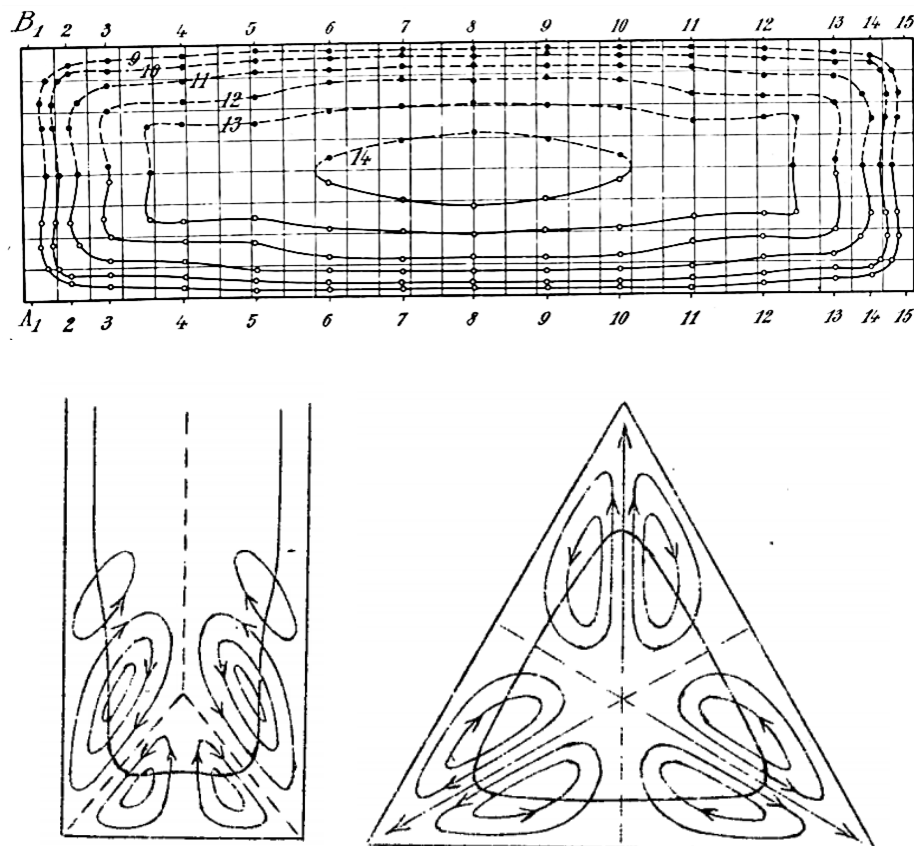


Figure 1.7. Secondary velocity patterns in non-circular cross sections [18].

Although visualization of these effects was relatively easy, precise measurement of the secondary velocities was difficult, since they are in the range of a couple of percent of the primary flow velocities. The first notable work in which these effects were measured was performed by Hoagland [23] in

1960. In 1971, Launder and Ying [24] pointed out that Hoagland's results, although pioneering, were affected by the presence of measurement apparatus in the flow. They used an improved technique and performed one of the experiments referenced in the present report as a benchmark for validation purposes (see Section 3 for details). Multiple experiments were performed in the 1960s and 1970s that improved upon these initial studies, including some notable ones by Leutheuser [25], Brundrett and Baines [21], and Melling and Whitelaw [26] (see Section 4 for details).

Brundrett and Baines [21] provided the first complete theoretical description of the secondary flows and their relationship to the Reynolds stress tensor. They showed that the line bisecting the corner always separates two independent circulations and that neglecting the secondary flows in very wide and thin channels is well justified away from the channel edges. They also showed that axial vorticity is the main contributor to the turbulent secondary flows in straight non-circular ducts [27]. The axial vorticity source term is defined as

$$\Phi_{\zeta} = \frac{\partial^2(\tau_{xx} - \tau_{yy})}{\partial x \partial y} + \frac{\partial^2 \tau_{xy}}{\partial y^2} - \frac{\partial^2 \tau_{xy}}{\partial x^2} \quad (1)$$

where τ_{xx} , τ_{yy} are normal, and τ_{xy} are shear, stress components.

This definition implies that linear turbulence models based on the eddy viscosity concept, such as KE, KW, and Spalart-Allmaras, are inherently unable to predict the secondary flows in non-circular ducts. For these isotropic models, Reynolds stress components are as follows:

$$\begin{aligned} \tau_{xx} &= \tau_{yy}, \\ \tau_{xy} &= \tau_{yx} = 0. \end{aligned} \quad (2)$$

Thus, the vorticity source term becomes zero, and the secondary flows vanish. On the contrary, for anisotropic eddy viscosity models, and RS turbulence models, initially developed by Launder [28], the axial vorticity source term is non-zero and, as a result, these models are capable of predicting the secondary flows in straight non-circular ducts.

The studies on heat transfer in square and rectangular ducts indicate that the contours of turbulent heat flux are also sharply distorted toward the channel edges because of the secondary flows [29], [30] (see Section 5 for details).

It is one of the objectives of the present work to select benchmark experiments that allow testing of the performance of various turbulence models available in commercial codes for flow and heat transfer near the edges of coolant channels since this can be a region where minimum safety margins occur for involute plate reactors.

1.4 Initial Selection of Benchmark Experiments

While many experiments studying the topic of flow in straight non-circular ducts were performed in the past, not all of them are suitable for CFD benchmarking. Most frequently, the reason behind it is the lack of a sufficient number of input parameters. The experimental data are not always provided in a raw format. Some crucial flow parameters, like inlet velocity and maximum temperature in the test channels, is convoluted or simply omitted in the reports. Usually, a normalization of the data is performed by the authors to achieve non-dimensional results, which are understandably more useful for comparisons with experiments conducted by other researchers. This process of normalizing

without listing all raw data has implications on the usefulness of the data for CFD code validation. For some experiments, although the inputs were provided, the bias error between the simulated results and the experimental data was too big to be explained by uncertainties of the inputs. This observation does not necessarily imply that the CFD calculations were wrong, but rather that some aspects of the experiment were not understood by the modelers or were not reported in the original references.

Launder and Ying [24] studied experimentally induced secondary flows in air in straight square ducts. They performed experiments for smooth and rough walls to verify the hypothesis that the secondary velocity profiles normalized by the average friction velocity are independent of the channel wall roughness. As a result, an implied conclusion of their study was that for flow in smooth and rough ducts, velocity normalized by friction velocity is independent of Reynolds number (Re). Additional information on their experimental and theoretical work can be found in [31]. In the current work, as presented in Section 3, only the experimental results obtained for smooth channels were used to test the performance of several turbulence models for various near-wall mesh sizes.

In the experiment conducted by Launder and Ying, the inlet velocity was not specified; only the Re of the flow was given. However, to define the inlet conditions in the CFD model, bulk velocity or flow rate must be specified. To do so, required an assumption about the value of the room temperature in the experiment, and the inlet velocity that needed to be calculated based on the Re and air viscosity at the assumed room temperature. Thus, an unnecessary error was introduced. Luckily, the results, in the form of a scaled velocity field, were presented as a function of bulk velocity (as opposed to the duct center value). Thus, it is assumed that the error of the abovementioned assumption cancels out in the comparison of the results.

Melling and Whitelaw's experiment was primarily designed to provide experimental data for mathematical turbulence modeling and for evaluating the performance of anemometers for detailed flow measurements [26], [32]. In their experiment, water was used as a working fluid. In contrast to the experiment conducted by Launder and Ying, the experiment conducted by Melling and Whitelaw, presented in Section 4 of the present report, uses scaling of the velocity profiles with respect to the velocity in the center of the channel (maximum velocity). Such scaling is very sensitive to that single point measurement and may lead to an offset or bias error in all results if the center point velocity is not accurately estimated in either the experiment or the simulation, or if the center of the duct in the experiment is not properly located. From that perspective, scaling of the velocity profiles with respect to the average, or bulk, velocity is again a better option, as the bulk velocity in both the experiment and especially the simulation is well controlled. While the scaling of the results was performed with respect to the unspecified center velocity, the bulk velocity at the inlet was provided by the authors of this work in [26], [32]. Thus, the inputs were properly defined and CFD simulations could be executed without additional assumptions.

To show how the value of the maximum velocity of the flow changes along the duct, Figure 1.8 presents a cumulative plot of scaled center velocities by respective bulk velocity in the ducts of several experiments discussed here, as a function of normalized distance from the duct entrance. These plots were obtained with the use of computational models (URANS, RS-EB with $y^+ > 30$, see Sections 3, 4, and 5 for models description).

Melling and Whitelaw reported their measurements for $x/D_h = 36.8$ which, based on the plot Figure 1.8, is in the zone of the developing flow. Around this location, the normalized velocities change significantly, which indicates that the variations in the measurements of the center velocity may still be significant at that location and influence the results presented as scaled values.

While the authors of the other experiments claimed that the measurements were performed at the sections of the duct where the flow was fully developed, variations in the center velocity can still be noticed (see Figure 1.8). The effect of the measurement location on the results was not reported for most of the experiments.

The presence of the devices upstream of the testing ducts (fans, flow straighteners, diffusers) was also not reported. For the Launder and Ying's experiment, an effect of a diffuser was numerically studied. There are notable differences in the scaled center velocities in the developing part of the flow. For most of these experiments, the details of the geometry of the upstream components are not reported and for that reason cannot be modeled precisely.

In the search for a suitable benchmark for corner flow analysis that would also contain a heat transfer component, this scaling issue became even more problematic. Many experiments deal with very small temperature gradients between the heated walls and the center of the duct as compared to the gradients expected between the fuel plates and the coolants in the reactor flows. While the normalized experimental temperature profiles usually range between 0 (minimum value) and 1 (maximum value), the absolute temperature range is within a small range of a few degrees Celsius. This makes benchmarking quite challenging, and a suitable validation experiment dealing with heat transfer is hard to find. In the present work, the experiment conducted by Hirota et al. [29] was selected, as it is free of some of these deficiencies impacting the modeling. In that experiment, the walls of a square duct were heated using steam in an outer channel surrounding the testing duct. This led to constant temperature on the walls of the testing duct that allowed for a much larger gradient of temperatures than some other experiments that were considered. Although some of the input parameters had to be assumed by the modelers, other work published by these authors and their co-workers, allowed for numerical model development.

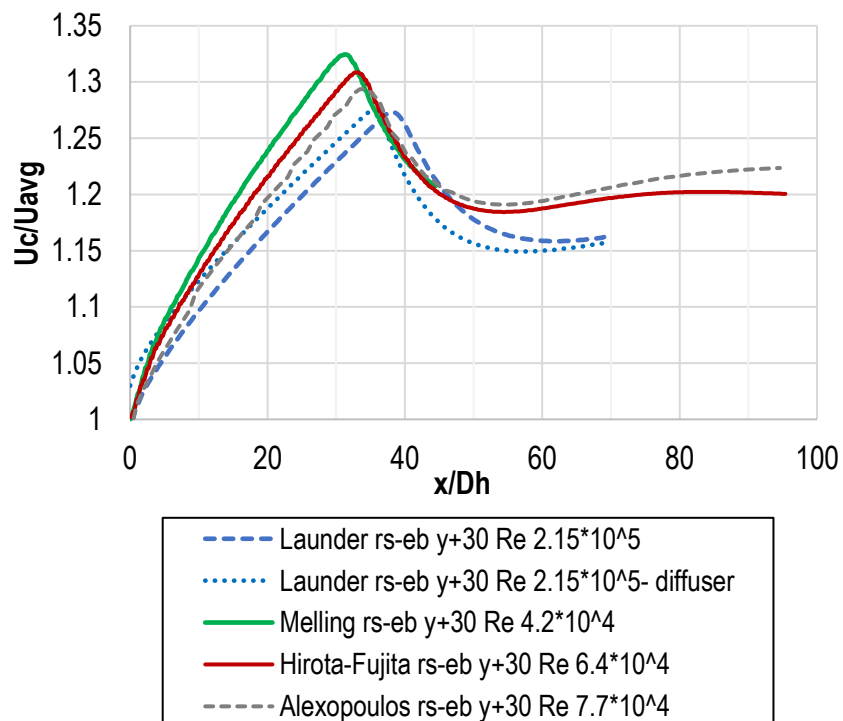


Figure 1.8. Scaled velocity in the center of the duct in the benchmark experiments.

Table 1.3. Description of the candidate benchmark experiments.

Experiment	Medium	Re	Cross section	Length*	Included in the present report?
Lauder & Ying [31]	Air, isothermal	215,000	10 cm x 10 cm	7 m (69 D_h)	Yes
Melling & Whitelaw [26]	Water, isothermal	42,000	4 cm x 4 cm	1.8 m (29 D_h)	Yes
Hoagland [23]	Air, isothermal	60,000	4.2 cm x 12.7 cm	9.7 m (154 D_h)	No
Hirota et al. [29]	Air, heated (constant temperature on all walls)	65,000	5 cm x 5 cm	4.77 m (95.4 D_h)	Yes
Alexopoulos [30]	Air, heated (constant heat flux on all walls)	77,000	9.6 cm x 9.6 cm	9.1 m (95.2 D_h)	No

* D_h = hydraulic diameter

As a brief summary of the reviewed experiments, Table 1.3 shows the basic dimensions of the ducts, Re of the flow, and medium used in the experiment. CFD models of five experiments have been developed while the results of three of them are presented in this report. The source of discrepancies between the simulated results and the experimental data for the experiments of Hoagland as well as that of Alexopoulos could not be explained and for that reason, these are not presented here.

2 Simulations of a Generic Fuel Plate

2.1 Base Simulations

To verify the importance of proper accounting for turbulence effects near the corners of thin coolant channels, an analysis was performed with a simplified (flattened) single-channel model (called further “SC model”) with a single coolant channel. The dimensions of the cross section of that model are presented in Figure 2.1. The dimensions of the SC model in the axial direction are shown in the side view in Figure 2.2. The base model is not symmetric, although the fuel core was almost centered within the plate in the base model. To verify how the position of the fuel core within the plate affects the heat transfer and temperature distributions as well as the performance of various turbulence models, the position of the fuel core within the plate was shifted in the lateral direction closer to the side plate, in the direction of the power peak. In the base case, the fuel-core edge was positioned at 2.6 mm from the side plate, which is equivalent to approximately two hydraulic diameters, D_h , of the modeled coolant channel gap. For the geometry with shifted fuel core, the following cases were considered:

- Shifted case #1, with the distance between the edge of the fuel core and the side plate reduced by half from 2.6 mm to 1.3 mm (equivalent roughly to $1.0 D_h$).
- Shifted case #2, with the distance between the edge of the fuel core and the side plate reduced by 75% from 2.6 mm to 0.65 mm (equivalent roughly to $0.5 D_h$).
- Shifted case #3, with the distance between the edge of the fuel core and the side plate reduced by 92% from 2.6 mm to 0.2 mm (equivalent roughly to $0.15 D_h$).
- Shifted case #4, with the distance between the edge of the fuel core and the side plate increased by 50% from 2.6 mm to 3.9 mm (equivalent roughly to $3.0 D_h$).

Cases #1 and #2 were analyzed with the RKE, KW-QCR, and RST-EB turbulence models (see Appendix A for the references with the descriptions of the turbulence models discussed in this report). Cases #3 and #4 were only run for the KW-QCR turbulence model, to confirm the trends on a larger number of data points.

Table 2.1 lists the dimensions that change in these cases. In all the cases, the overall width of the fuel core remained the same and the power density distribution was translated together with the fuel core.

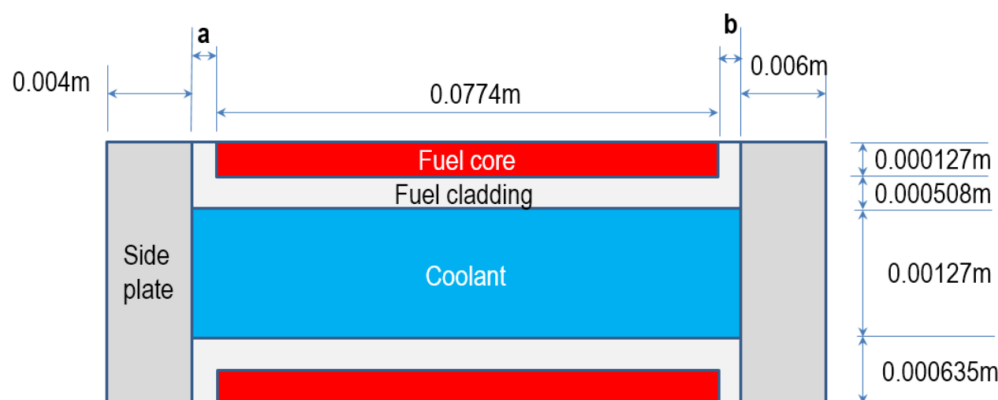


Figure 2.1. The geometry of the generic SC model of plate and coolant channel.

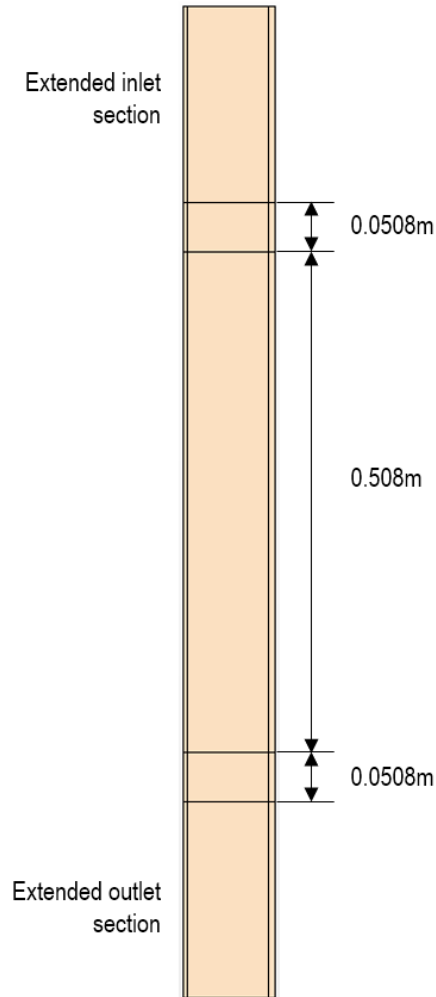


Figure 2.2. Side view of the SC model.

Table 2.1. Distance between the fuel core and the side plate in the analyzed cases.

Case	a (mm)*	b (mm)*
shifted #4	3.9	2.6
base	2.6	3.9
shifted #1	1.3	5.2
shifted #2	0.65	5.85
shifted #3	0.2	6.3

*See Figure 2.1.

The SC model used a non-uniform power distribution with a shape mimicking the shape of the power function encountered in involute fuel plates with characteristic power peaking near the edges of the fuel core. Power distribution on the plate as used in the simulations is shown in Figure 2.3, with three plots representing power density at the leading edge, in the middle, and at the trailing edge of the plate, respectively. The prescribed bulk coolant velocity in the channel was 14.0 m/s. The inlet coolant temperature was set at 49 °C. Adiabatic boundary conditions were set up at the edges of the side plates. Readers are referred to a previous report [17] where the SC model is described in more detail.

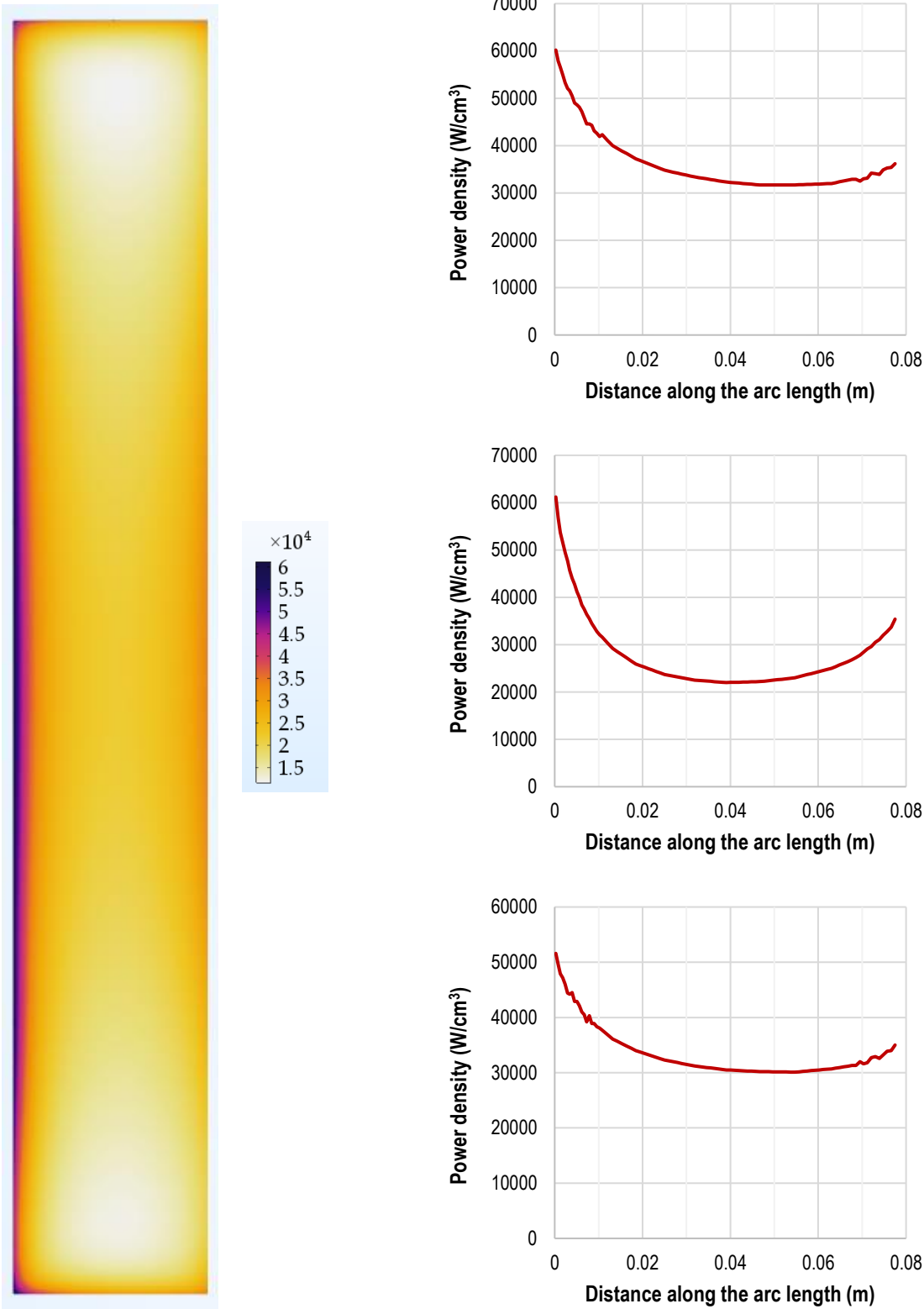
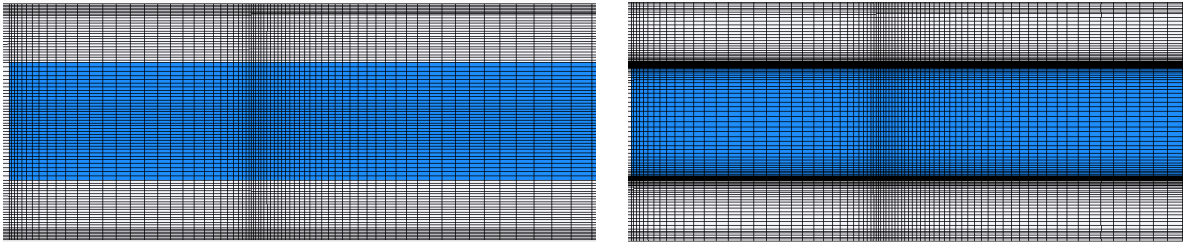


Figure 2.3. Power density distribution in the fuel (W/cm³) at the (upper right) leading edge, (center right) middle, and (lower right) trailing edge of the plate.

Two near-wall grid densities were considered in the analysis, with y^+ in the range of $1 < y^+ < 5$ and $y^+ > 30$, respectively. Most of the simulations were performed for the coarse grid models, as they required fewer computational resources. Also, one of the RANS turbulence models (RST-QPS) was not implemented for low y^+ , when $y^+ < 5$. Figure 2.4 presents details of these two grid densities. The total number of cells in the models was around 8 million and 13 million for the $y^+ > 30$ and $1 < y^+ < 5$ meshes, respectively.



**Figure 2.4. Computational grid details for two near-wall densities:
(left) $y^+ > 30$; (right) $1 < y^+ < 5$.**

In this part of the study, six turbulence models were considered:

1. Linear realizable k-epsilon: two-layer model, RKE
2. Linear k-omega (SST), KW
3. K-omega (SST) with quadratic terms, KW-QCR
4. Reynolds stress transport with elliptic blending (high and low y^+), RST-EB
5. Reynolds stress transport with linear pressure strain, two-layer model (high and low y^+), RST-LPS2L
6. Reynolds stress transport with quadratic pressure strain (high y^+ only), RST-QPS

Figure 2.5 through Figure 2.7 show the velocity magnitude distribution in the cross section (top), together with the secondary velocities (bottom), for three turbulence models that are representative of all other models. The RKE model with linear realizable turbulence was not able to capture the secondary flows in the cross section. It is represented with near-zero in-plane velocities in the bottom of Figure 2.5. This finding was representative for both the linear RKE and KW turbulence models. On the contrary, the distribution of secondary flow velocities in the cross section of the channel for the quadratic KW-QCR model is similar to the patterns and magnitude found in simulations with RS turbulence models (Figure 2.6 and Figure 2.7, respectively). The magnitude of that secondary velocity is, as expected, negligible—on the order of $\sim 1\%$ —as compared to the magnitude of the axial velocity.

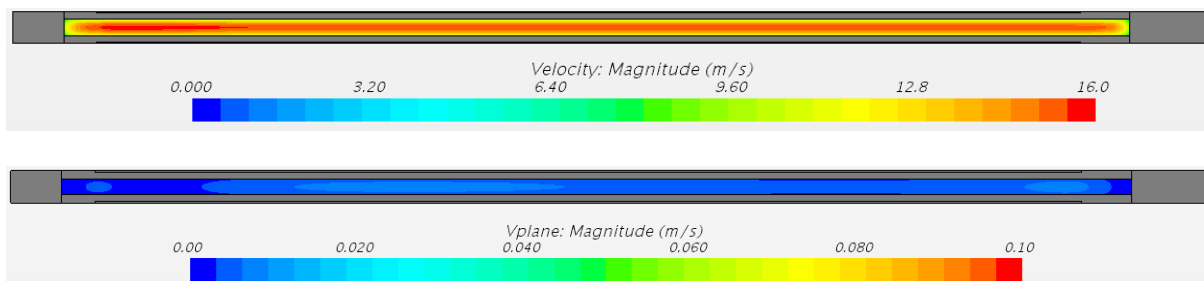


Figure 2.5. The magnitude of (top) axial velocity and (bottom) in-plane velocities in generic CFD model with linear RKE turbulence model (units of m/s).

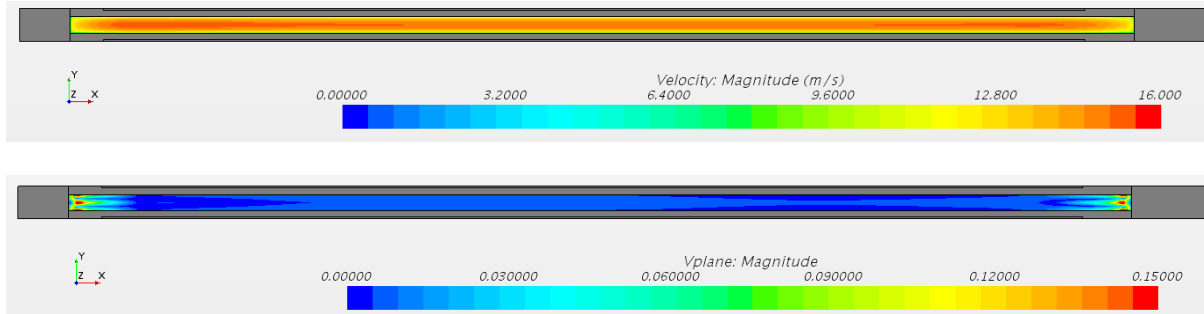


Figure 2.6. The magnitude of (top) axial velocity and (bottom) in-plane velocities in generic CFD model with KW-QCR (quadratic terms) turbulence model (units of m/s).

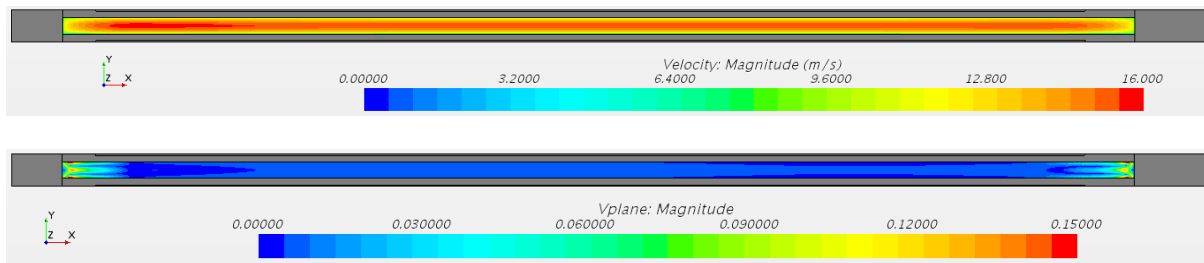


Figure 2.7. The magnitude of (top) axial velocity and (bottom) in-plane velocities in generic CFD model with RST-EB (elliptic blending) turbulence model (units of m/s).

Figure 2.8 shows a closer view of the profiles of secondary flow velocities near the edges of the coolant channel for KW-QCR (left) and RST-EB (right). These profiles look very similar. What can be noted is the extent to which the secondary flow has a noticeable presence. At the end of the fueled portion of the plate (marked by red arrows in the figure), the influence of already-small secondary flow velocities is further decreased. The cases with a shifted fuel core, analyzed further in Section 2.2, place the edge of the fuel well within the zone of influence of secondary flows on axial flow.

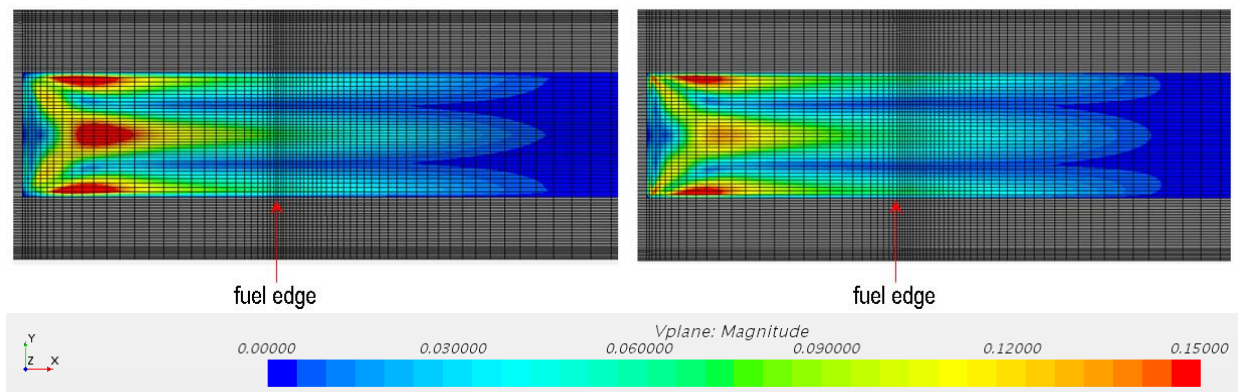


Figure 2.8. The magnitude of in-plane velocities in a generic CFD model with (left) KW-QCR and (right) RST-EB turbulence models (units of m/s).

Figure 2.9 presents typical distributions of the temperature and the heat flux at the interface between the cladding and the coolant, with a peak near the edge of the fuel core. Also included in the figure are the lines at which the heat flux and the temperature were compared in all cases. The location of the maximum of the boundary heat flux is aligned with the location of maximum power-density input. The location of the maximum temperature is located further downstream.

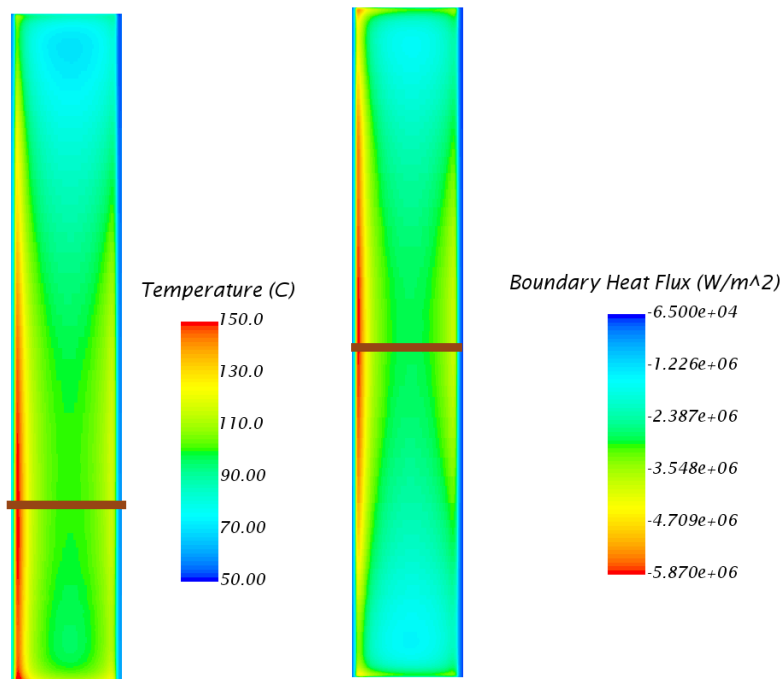


Figure 2.9. Locations of interest on the cladding-coolant interface for peak temperature and heat flux measurements.

Figure 2.10 and Figure 2.11 show the distribution of maximum heat flux and maximum temperature, respectively, on the cladding-coolant interface for the base model with near-wall mesh density of $Y^+ > 30$. The difference in predicted heat fluxes among various turbulence models (Figure 2.10, right) is marginal. The difference in the peak temperatures predicted by the selected turbulence models (Figure 2.11, right) is more noticeable.

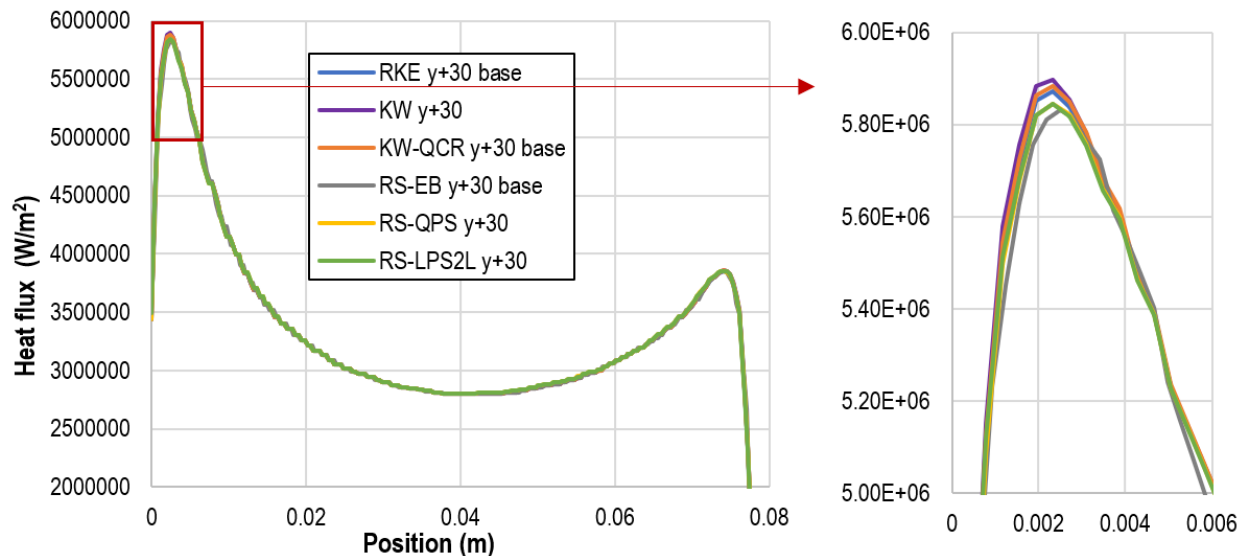


Figure 2.10. Maximum heat flux on the cladding-coolant interface in generic CFD models: (left) full range and (right) close-up of the peak.

The lowest peak temperature of 147.7 °C was predicted by the model with linear KW turbulence, followed by 148.5 °C as predicted with the use of KW-QCR. The peak temperature predicted by the linear RKE model is 151.1°C, a value nearly identical to the one predicted by the RST-QPS model. The RST-LPS2L turbulence model predicted maximum cladding temperature of 153.0 °C, while the highest temperature of 153.5 °C was predicted by the RST-EB turbulence model.

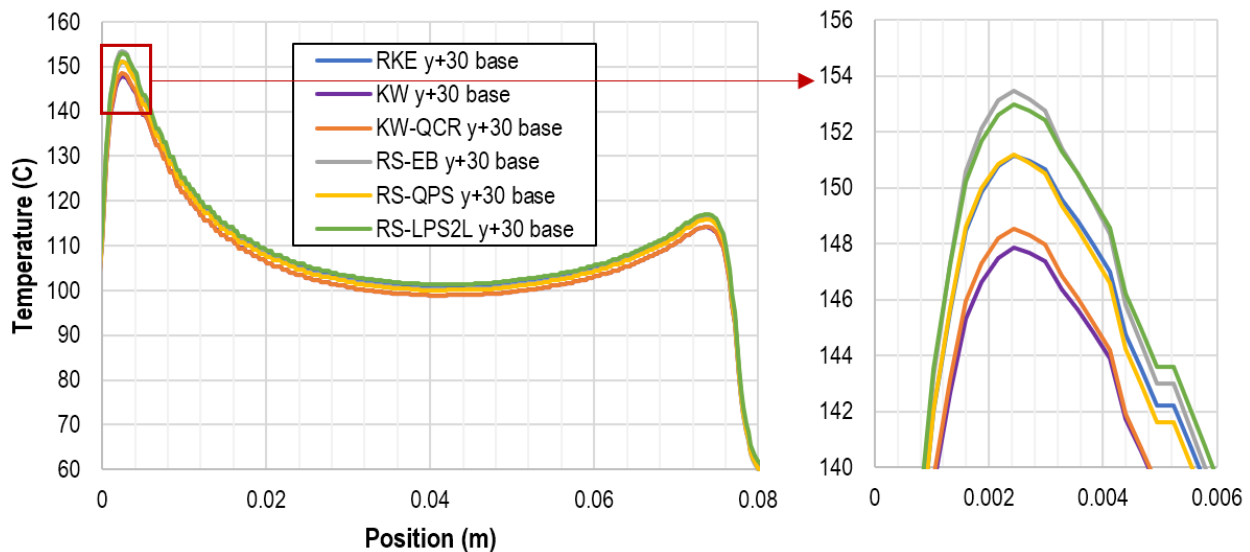


Figure 2.11. Maximum temperature at the cladding-coolant interface in generic CFD models: (left) full range and (right) close-up of the peak.

Figure 2.12 compares the maximum temperatures predicted by various turbulence models and two mesh densities. According to the STAR-CCM+ manual, RST-QPS is an improved implementation of the RST-EB turbulence model for the high- y^+ mesh. For the near-wall mesh $1 < y^+ < 5$, the RST-QPS model is not implemented so it was not used for the denser mesh model. The range of predicted peak temperatures is similar for the two mesh densities, with the lowest temperature for the models with the denser mesh ($1 < y^+ < 5$) also predicted by the linear KW model at 147.8 °C. The maximum temperature for the models with the denser mesh ($1 < y^+ < 5$) was predicted by the RKE and RST-LPS2L models at 153 °C and 152.8 °C respectively. The RST-EB model predicted a lower temperature of 150.7 °C.

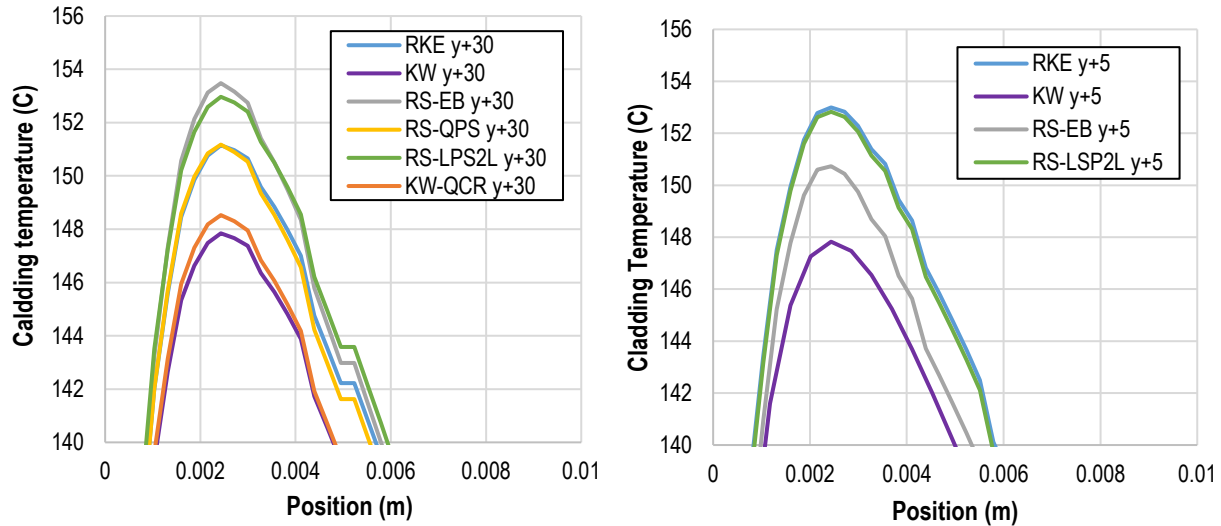


Figure 2.12. Maximum temperature at the cladding-coolant interface in generic CFD models, for models with (left) $y+ > 30$ mesh (left) and (right) $1 < y+ < 5$ mesh.

From the analyzed cases, in which fuel is sufficiently far from the corner (more than two times D_h), it appears that the difference in predicted peak temperatures is not attributable to the ability of a turbulence model to capture anisotropic effects near the corners. The observation that the RST-EB model tends to predict the highest cladding temperatures, and therefore gives the most conservative results for safety analysis, was one of the conclusions of work reported previously in [4] for the heat-transfer analysis with the focus on the center of the channel, away from the corners. The present analysis with RST-EB turbulence model predicted the highest temperature for the near-wall mesh $y+ > 30$. However, this turbulence model did not give the most conservative cladding temperature for the mesh with $y+ < 5$. The prediction was slightly lower than that made by RST-LPS2L and RKE turbulence models.

2.2 Simulations with Shifted Fuel Core

The results of the analysis with shifted fuel core positions within the plate are presented next. This part of the study was performed only for the models with near-wall mesh $y+ > 30$. Figure 2.13, Figure 2.14, and Figure 2.15 present heat-flux distributions across the plate width (located as shown in Figure 2.9) in models with near-wall mesh size $y+ > 30$ for the KE, KW-QCR, and RST-EB turbulence models, respectively. Each plot contains the results for the base model with the original position of the fuel in the plate as well as for the two cases with the core shifted towards the side plate (note that the origin of the X axis is located at the edge of the fuel core in the base model). As expected, all three turbulence models predict an increase in the maximum heat flux value for the shifted core. There is no apparent difference in the trends between the isotropic KE model and the anisotropic turbulence models.

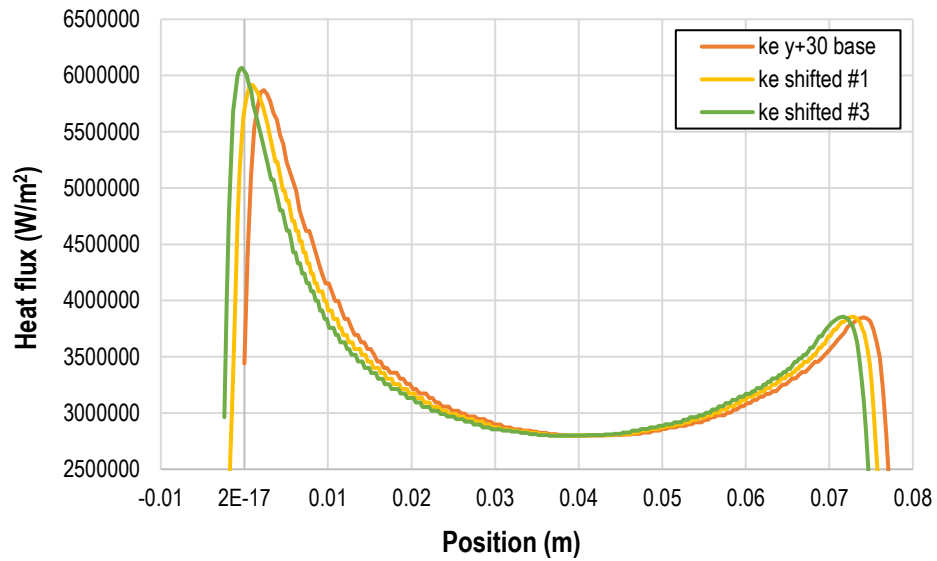


Figure 2.13. Heat flux in models with RKE turbulence and near-wall mesh size $y^+ > 30$.

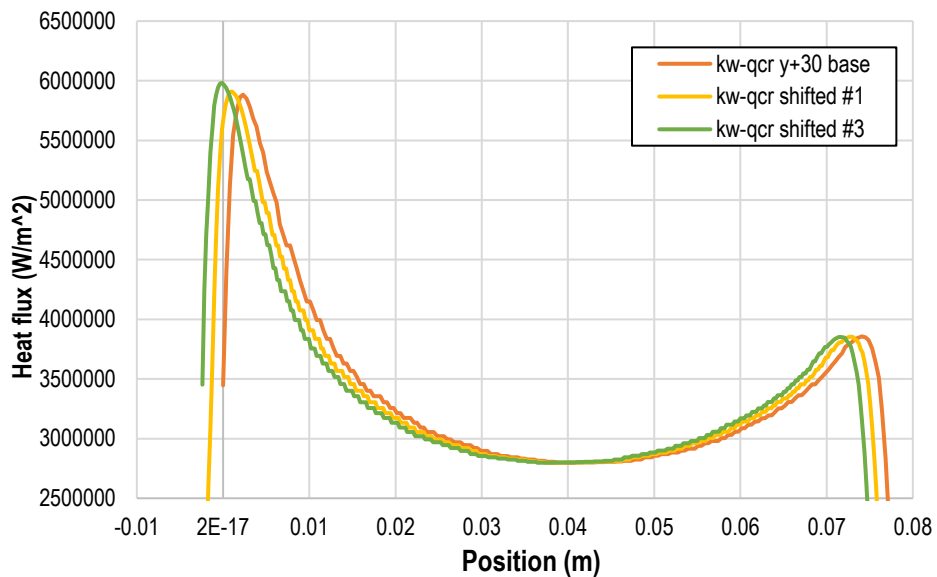


Figure 2.14. Heat flux in models with KW-QCR turbulence and near-wall mesh size $y^+ > 30$.

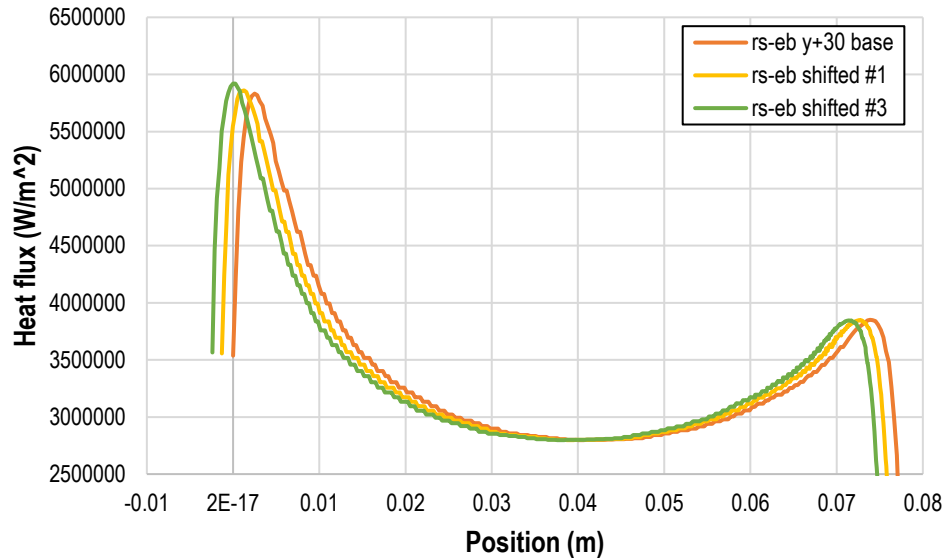


Figure 2.15. Heat flux in models with RST-EB turbulence and near-wall mesh size $y^+ > 30$.

A similar set of plots was generated for the temperature at the interface between the cladding and the coolant along a section located as shown in Figure 2.9. These are presented in Figure 2.16, Figure 2.17, and Figure 2.18. Each of them shows an increase of the peak temperature once the fuel core is moved closer to the side plate. There is no apparent difference in the trends between the isotropic KE model and the anisotropic turbulence models.

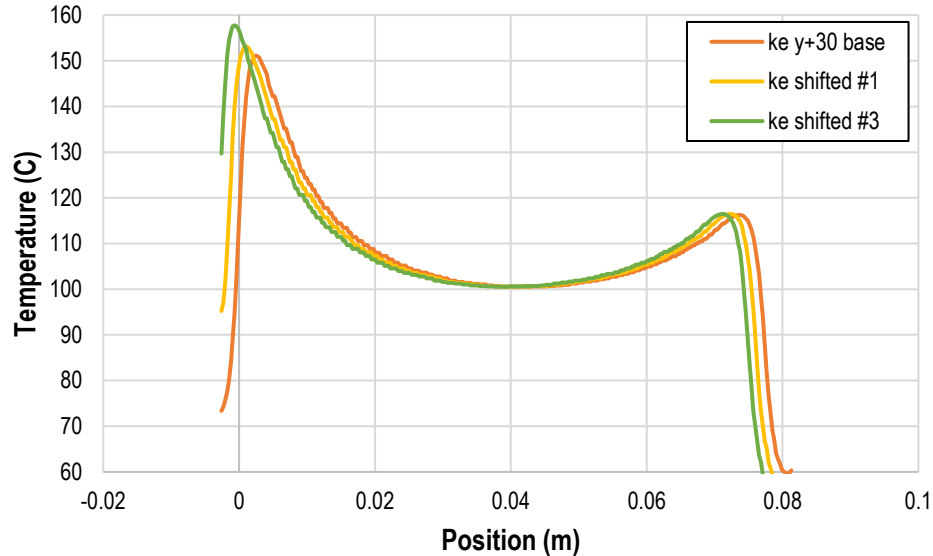


Figure 2.16. Temperature in models with RKE turbulence and near-wall mesh size $y^+ > 30$.

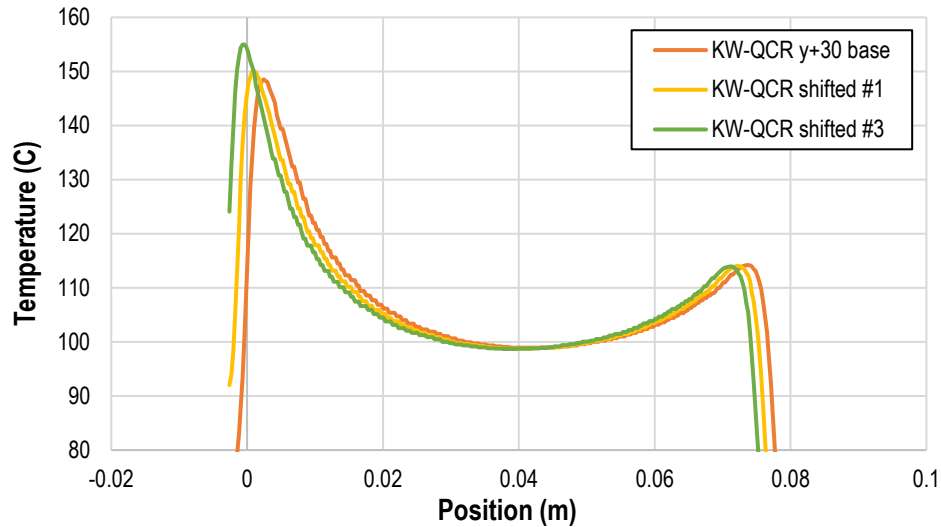


Figure 2.17. Temperature in models with KW-QCR turbulence and near-wall mesh size $y^+ > 30$.

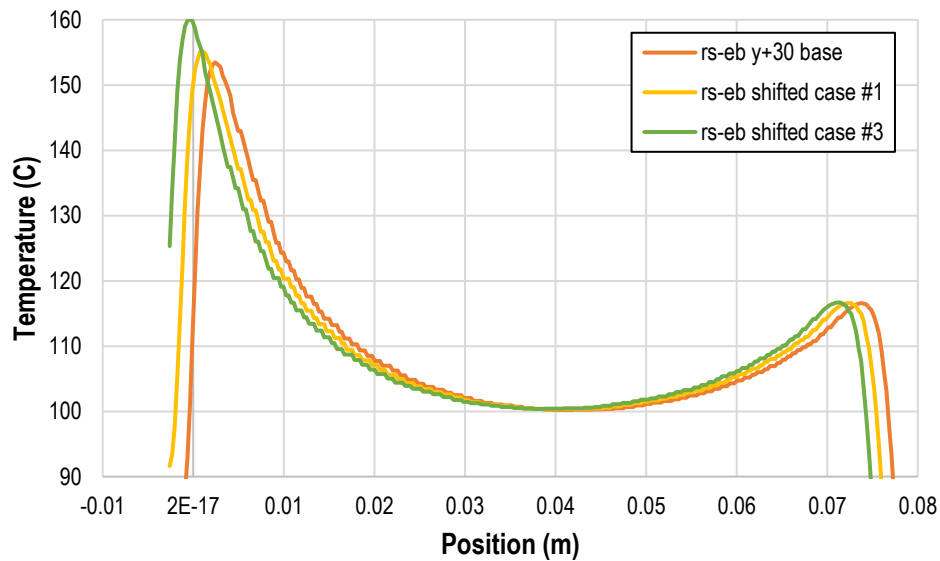


Figure 2.18. Temperature in models with RST-EB turbulence and near-wall mesh size $y^+ > 30$.

Figure 2.19 shows the dependency of peak heat flux on the distance between the fuel edge and the side plate for various turbulence models. The trends for the KW-QCR and RST-EB turbulence models are almost identical, with an equal offset at each distance between the fuel edge and the side plate. The trend is steeper for the results obtained with the linear RKE model.

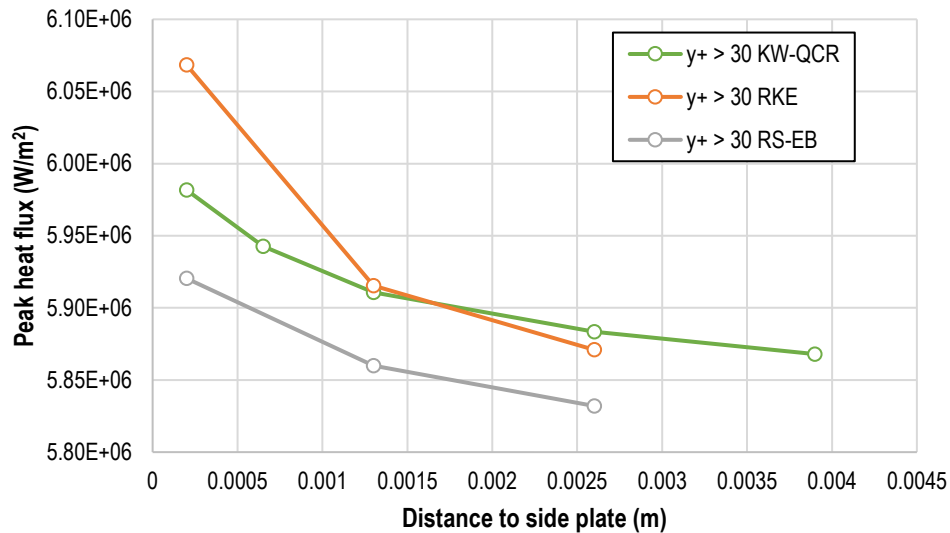


Figure 2.19. Dependency of peak heat flux on the distance between the fuel edge and the side plate for various turbulence models.

For the safety analysis, one of the most important results is the temperature at the cladding-coolant interface. Figure 2.20 shows the dependency of peak temperature on the distance between the fuel edge and the side plate for various turbulence models. Consistently, for all the distances, the RST-EB model predicts the highest temperature at the cladding-coolant interface, followed by RKE, and KW-QCR predicts the lowest value. Regardless of the ability of the models to capture the secondary flows, all trends look alike.

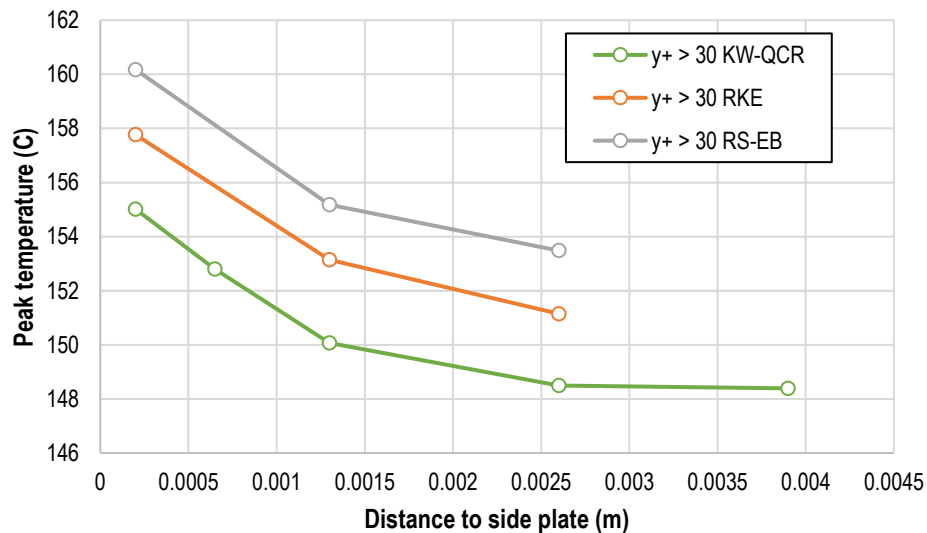


Figure 2.20. Dependency of peak temperature at the cladding-coolant interface on the distance between the fuel edge and the side plate for various turbulence models.

The difference between predictions for the KW-QCR and RST-EB model was about 5 °C for all analyzed positions of the fuel in the plate. This is not a negligible difference as it makes up for approximately 3% of the predicted temperature and for that reason, the use of CFD models for safety analysis should

never be limited to a single turbulence model. The recommendation is to test several of them (as a minimum RKE and KW as the two most robust ones) and report the range of possible predictions as an uncertainty of the simulations.

It was shown that the relative distance between the fuel edge and the side plate has no influence on the peak temperature in the cladding, as long as that distance is larger than two D_h . The closer the edge of the fuel gets to the side plate, the higher the predicted peak temperature on the cladding-coolant interface. This behavior was confirmed with the use of three turbulence models: RKE, KW-QCR, and RST-EB. RKE, which is an isotropic eddy viscosity model, is not capable of predicting the anisotropic flow patterns in the corners. Thus, the effect presented here appears not to be attributable to the anisotropy of the flow in the corners. Nevertheless, to better understand the ability of various turbulence models to capture the flow patterns in that section of the coolant channel ($2D_h$ and closer to the edge), validation of these models against the selected experimental benchmarks is performed.

3 Simulations of Launder and Ying's Experiment

3.1 Description of Launder and Ying's Experiment

An open-circuit air flow facility with a square 23-ft (~ 7 -m)-long duct channel was used in the experiments [24]. The internal side dimension of the duct was 4 in (10.16 cm). The walls were built of 0.5-in (1.27-cm)-thick Perspex sheets. A 6-ft-long transition duct was installed between the settling chamber (with a bigger, but unknown, cross-section) and the square test section. The secondary velocities were measured in a testing section located 2 in (5.08 cm) upstream from the exit of the duct.

Hot-wire probes were used for the measurements of secondary flow angles, as described in detail in [21]. A Pitot tube assembly was used to measure axial velocities, which together with the measured angles allowed for determination of the magnitude of the secondary velocities. The accuracy of the secondary flow angle measurement was $\pm 0.2^\circ$, and the accuracy of measurements of the secondary velocities was $\pm 5\%$. The accuracy of the Pitot tube setup was not specified; thus, uncertainty in the measurements of the mean velocities cannot be directly deduced from [24].

The results for smooth-wall experiments were obtained for flow with $Re=215,000$. The raw measurement of bulk or center velocity was not given explicitly. Knowing the Re value and assuming the density and dynamic viscosity of air at room temperature (see Appendix B), the bulk velocity was estimated to be 32.08 m/s.

Figure 3.1 shows a digitized plot of the axial velocity profiles for a smooth square duct on the left, and the locations where the velocities were measured on the right. The measurements were taken along six lines, aligned with the x axis for $0 < x < h$, at $y/h = 0.05, 0.1, 0.2, 0.3, 0.5$, and 1.0 , where y is the vertical axis, $0 < y < 2h$, and h is equal to half the duct size. This set of data was the basis for comparison with computational results.

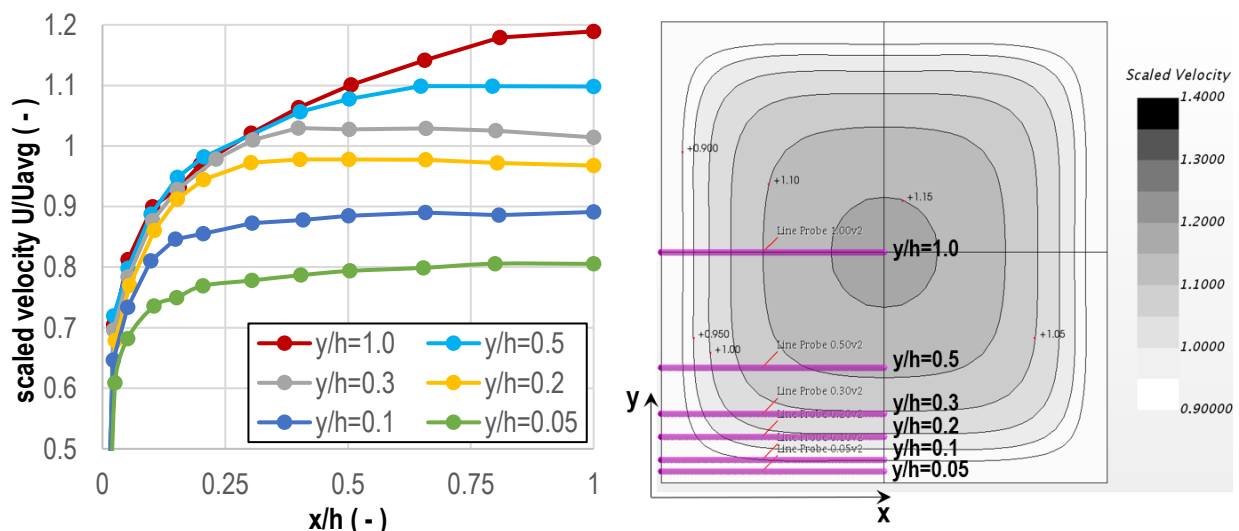


Figure 3.1. (Left) Digitized axial velocity profiles in a smooth square duct (source [24]); (right) location of the cross sections of interest for velocity reporting.

3.2 Description of the CFD Model

A CFD model, representing the test section only, was built using the commercial software STAR-CCM+. Three computational grids were built with hexahedral structured mesh for various mesh densities near the walls, with y^+ in the following ranges:

1. $y^+ < 1$ with 90 by 90 elements in the cross section,
2. $1 < y^+ < 5$ with 70 by 70 elements in the cross section, and
3. $y^+ > 30$ with 50 by 50 elements in the cross section.

The largest cells in the center of the cross section for all three models were squares with an edge size of ~ 0.004 m. The cross-section mesh was extruded along the length of the duct model to form 300 non-uniform layers with the smallest (0.01-m-thick) layers near the outlet section, from which the results were extracted.

These are the three most common ranges of mesh densities used in CFD models. Obviously, the coarser meshes are desirable for many engineering purposes, as they characterize models with the lowest number of cells. Fine meshes (especially those with $y^+ < 1$) are frequently not practical for use with complex geometries. Moreover, for some types of analyses like fluid-structure interaction between fuel plates and coolant, meshes are desired to be as coarse as possible, owing to the high computational burden of such analyses and lack of stability in the solution for the models with low- y^+ meshes.

Figure 3.2 shows cross sections through the models of the ducts with these three meshes. Note that the density of the elements in the center part is nearly identical for all three meshes; only the near-wall cells are different in these models.

Out of all the available turbulence models, five models were investigated in relation to the experimental data of [24]: realizable k-epsilon (RKE), k-omega (KW) SST, k-omega with quadratic terms (KW-QCR), Reynold's stress with elliptic blending (RST-EB), and Reynold's stress with linear pressure strain (RST-LPS2L). Two-layer all- y^+ models were used for all cases (refer to Appendix A and Simcenter STAR-CCM+ documentation [33] for further description of the turbulence models).

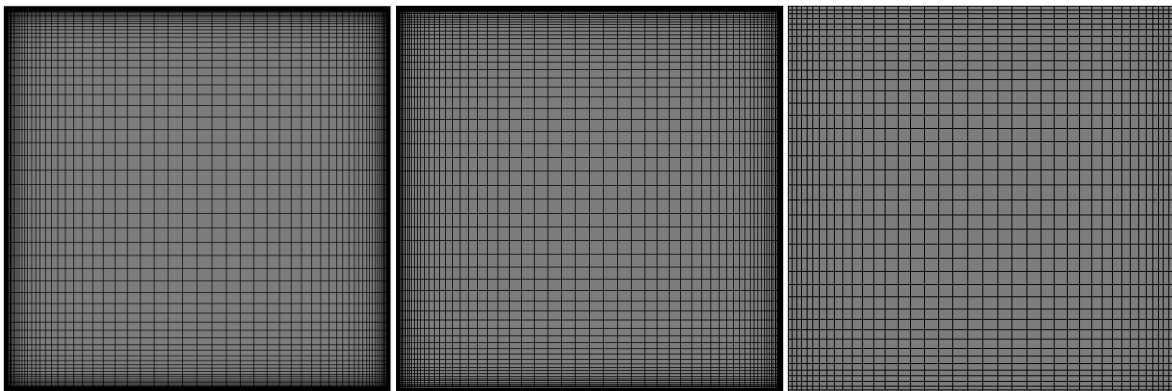


Figure 3.2. Cross section through three computational grids used to model the duct in [24]: (left) 90 by 90 cells with near-wall element size of $y^+ 1$; (center) 70 by 70 cells with $1 < y^+ < 5$; (right) 50 by 50 cells with $y^+ > 30$.

3.3 Results

Figure 3.3 shows velocity contours in models with different turbulence models and near-wall mesh density of $y^+ > 30$, compared to the profiles from the experiment. It can be noticed that all the models predict the contours reasonably well, but there are some that outperform the most popular ones, like the linear KE or linear KW (SST) model. KW-QCR (SST), with quadratic terms activated, performs better than its linear equivalent. In fact, the KW-QCR model with quadratic terms was one of the best-performing models in this test. The tested RS turbulence models performed very well by predicting velocity profiles that were close to the experimental ones.

While Figure 3.3 shows a qualitative comparison of contours of axial velocities, Figure 3.4 through Figure 3.6 show velocity profiles at the cross sections identified in Figure 3.2, compared to the experimental values. The velocities were scaled with the average flow velocity in the duct. Both the linear KE and the linear KW turbulence models visibly underpredict the velocity in the region from 0 to $0.2 x/h$ from the wall (where x is the distance from the inlet and “ h ” is half of the duct edge size). The three other turbulence models: KW with quadratic terms (KW-QCR), RS with elliptic blending (RST-EB), and RS with linear pressure strain two-layer model (RST-LPS2L) predict the profiles of velocities equally well near the walls ($0 < x/h < 0.2$) and in the middle of the duct. These conclusions are valid for all near-wall mesh densities considered. Figure 3.4 presents the results for a near-wall mesh size of $y^+ > 30$. Figure 3.5 presents the results for a near-wall mesh size in the range of $1 < y^+ < 5$, and Figure 3.6 presents the results for the densest near-wall mesh size of $y^+ < 1$. There is no substantial difference in the performance of various turbulence models with various near-wall mesh densities.

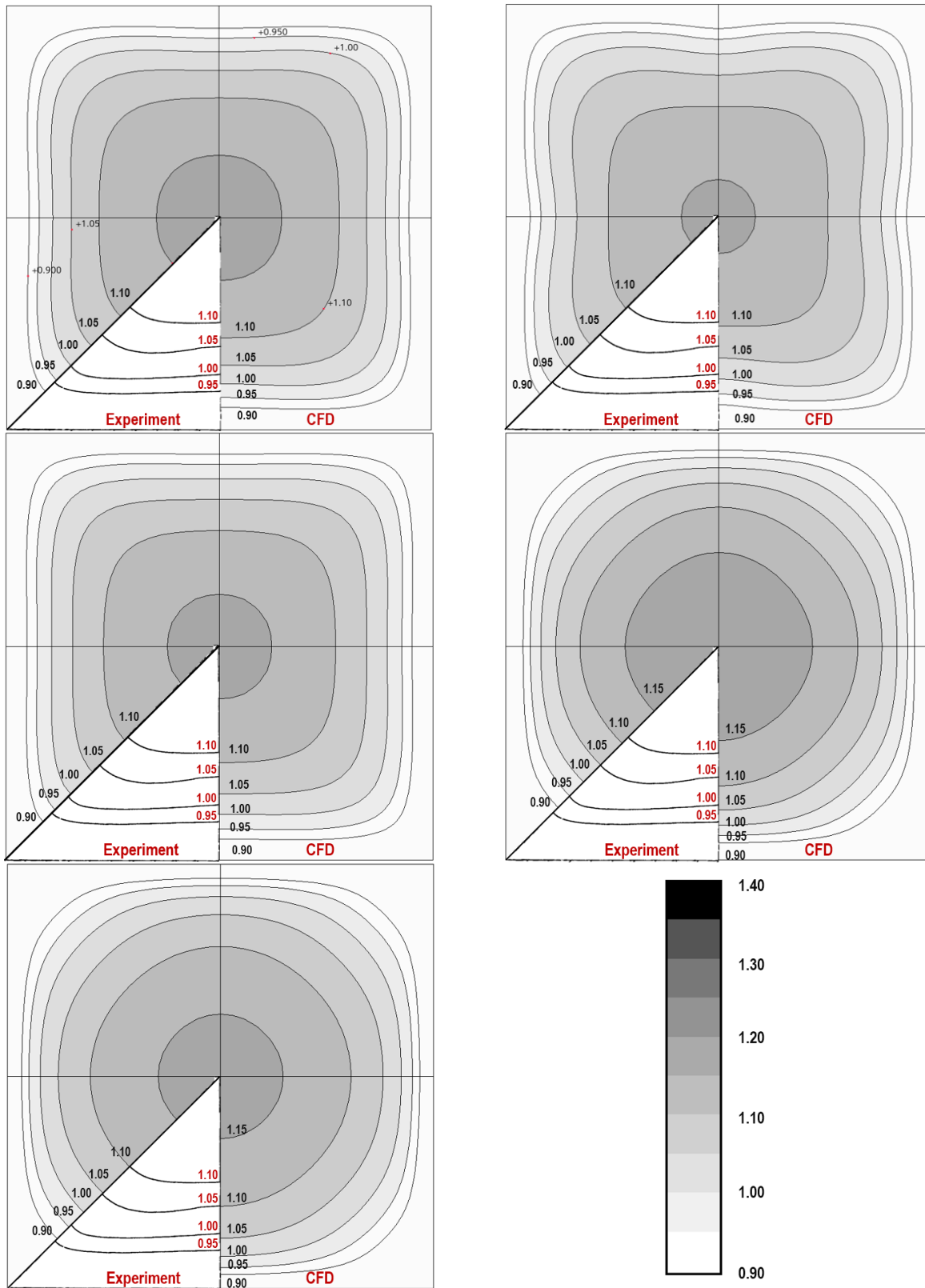


Figure 3.3. Constant-velocity contours for near-wall mesh size of $y^+ 30$, compared to the experimental data, for (from top left) RST-EB, KW-QCR, RST-LPS2L, RKE, and KW models.

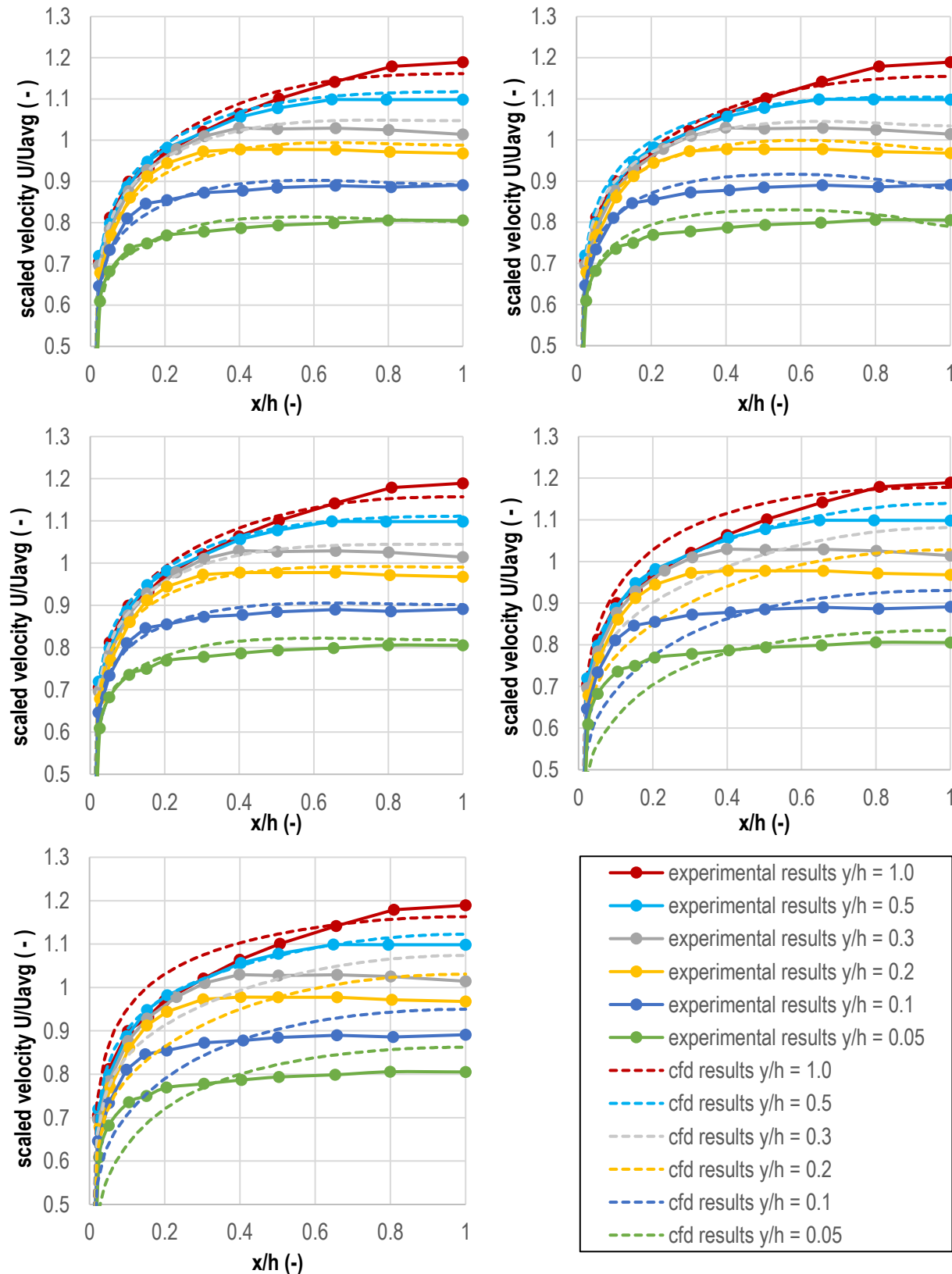


Figure 3.4. Axial velocity profiles for near-wall mesh size of $y^+ > 30$ compared to the experimental data for (from the top left) RST-EB, KW-QCR, RST-LPS2L, RKE, and KW models.

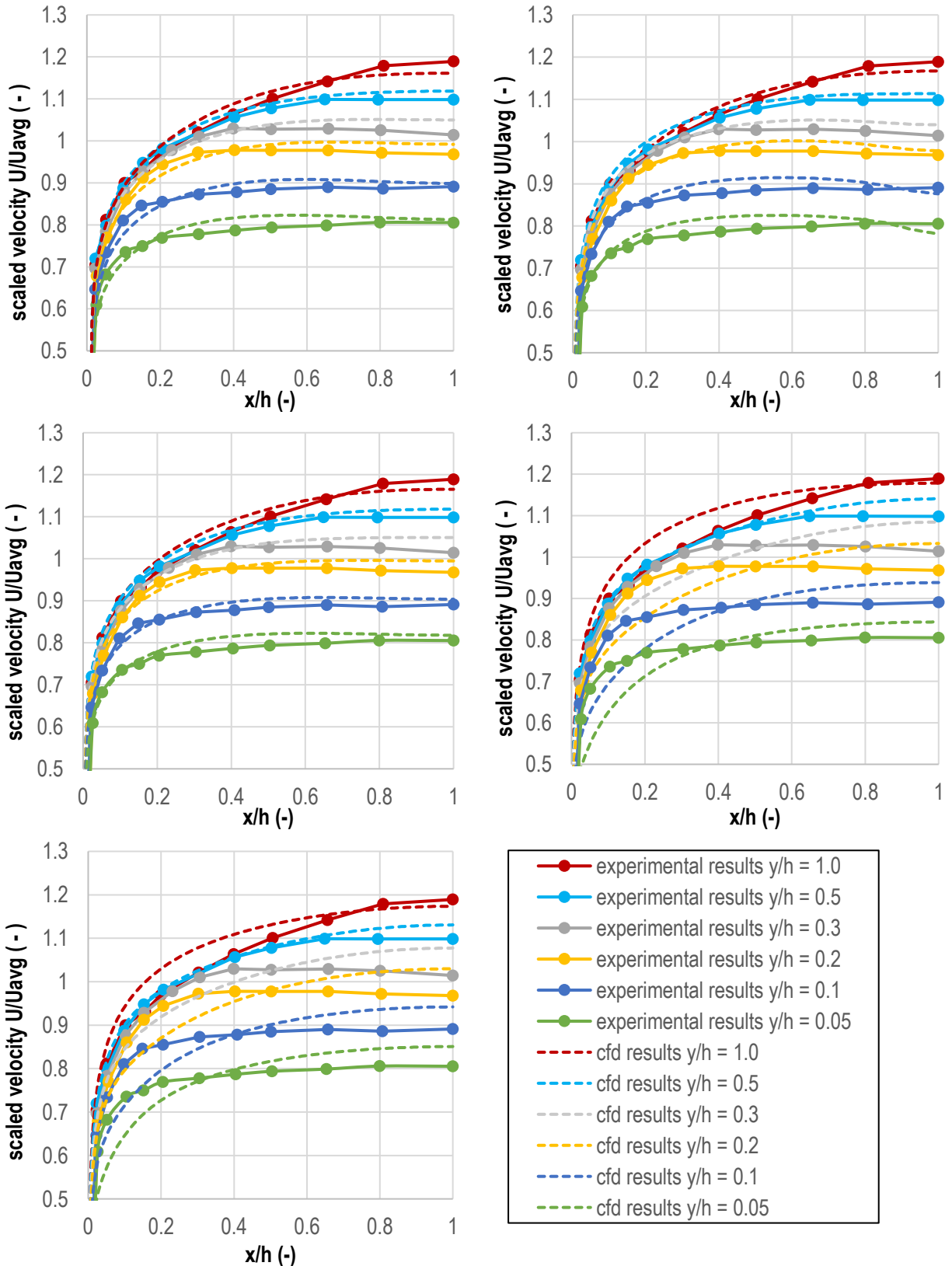


Figure 3.5. Axial velocity profiles for near-wall mesh size of $1 < y^+ < 5$ compared to the experimental data for (from the top left) RST-EB, KW-QCR, RST-LPS2L, RKE, and KW models.

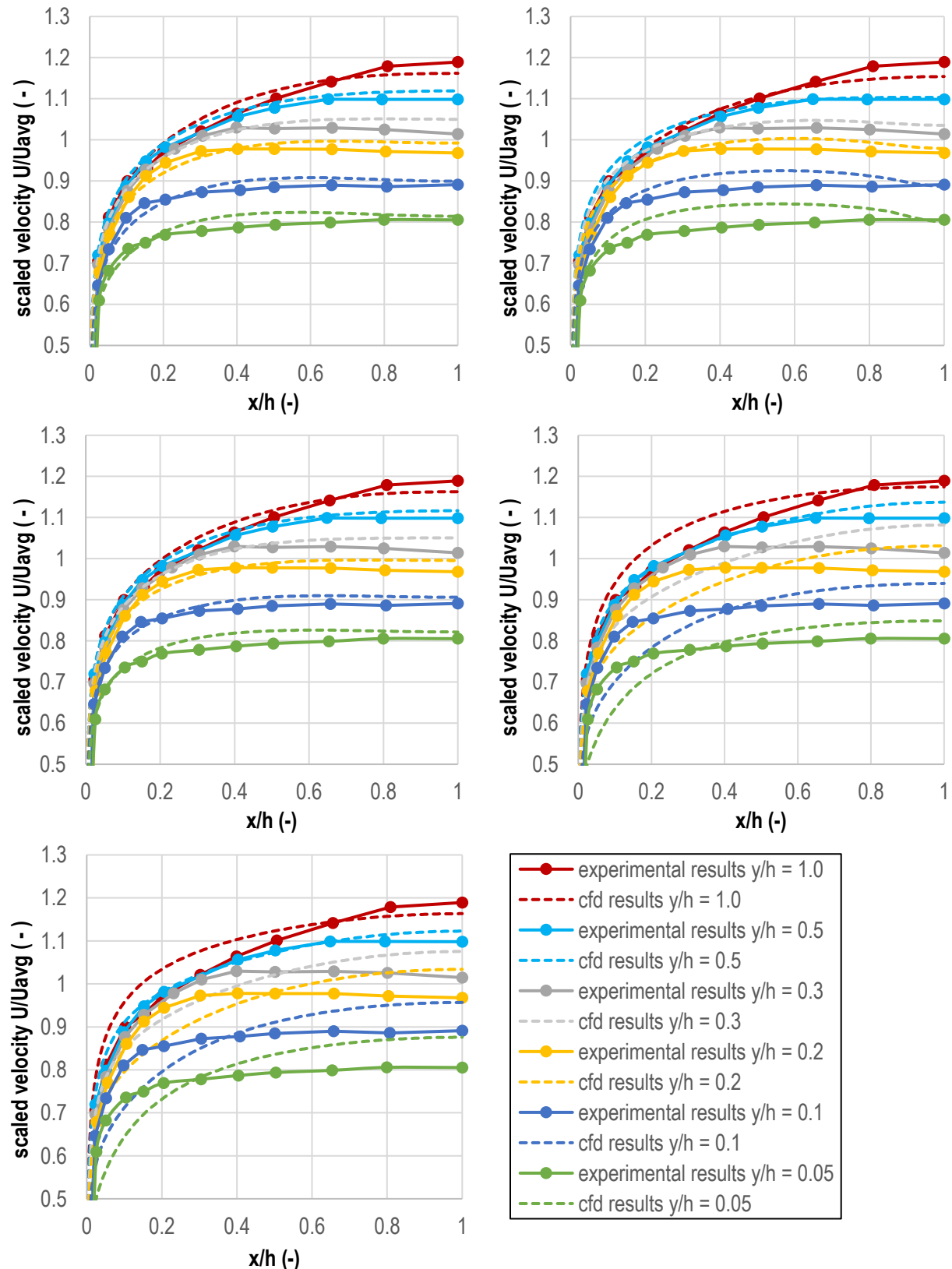


Figure 3.6. Axial velocity profiles for near-wall mesh size of $y^+ < 1$ compared to the experimental data for (from the top left) RST-EB, KW-QCR, RST-LPS2L, RKE, and KW models.

4 Simulations of Melling and Whitelaw's Experiment

4.1 Description of the Experiment

In the experiment designed by Melling and Whitelaw [26], the test duct was built of 9-mm-thick, 1.8-m-long Perspex walls. The inner cross section of the duct was 40 mm in width by 41 mm in depth (the accuracy of these values was ± 0.2 mm). The experiment used water as an operating fluid. It was pumped through the testing section upwards from a plenum in a closed loop. The pump was operated at a nominal flow of 1.50 kg/s, which corresponded to a bulk velocity in the test section of 0.915 m/s and a Re of 42,000.

A laser-Doppler anemometer was used to measure contours of time-averaged (mean) velocity and turbulence intensity in a developing flow. Although the authors of [26] claim that all three mean velocity components and five of the six Reynolds stresses components were measured in a nearly developed flow, the simulated results presented in their journal article indicate that the flow was still in the development stage, i.e., boundary layers were not fully developed. A detailed description of the measurement system is provided in references [26] and [32]. The laser-Doppler anemometer has advantages over the hot-wire probes used by Hoagland [23], Launder [24], and others in the measurement of secondary velocities, since no probes are present to interfere with the flow. The technique also allowed for measurements to be made at various cross sections in the developing flow in addition to the near-outlet cross section.

Not all reported data were available for all axial cross sections with locations described with the ratio x/D_h , where x is the distance from the inlet and D_h is the hydraulic diameter of the duct (40 mm). Axial velocity profiles, shown in Figure 4.1, were reported in detail only for $x/D_h = 29.0$, which corresponds to a distance of 1.17 m from the inlet. In the right-hand panel of Figure 4.1, the cross sections where the velocities were measured, are highlighted in pink. The axial velocity profiles were digitized from the figure available in the report [32] and used for comparison with the simulated results. The distortion of the axial velocity plots in Figure 4.1 is somewhat reduced in the digitization process, in which the reference frame is defined based on the distorted frame in the plot.

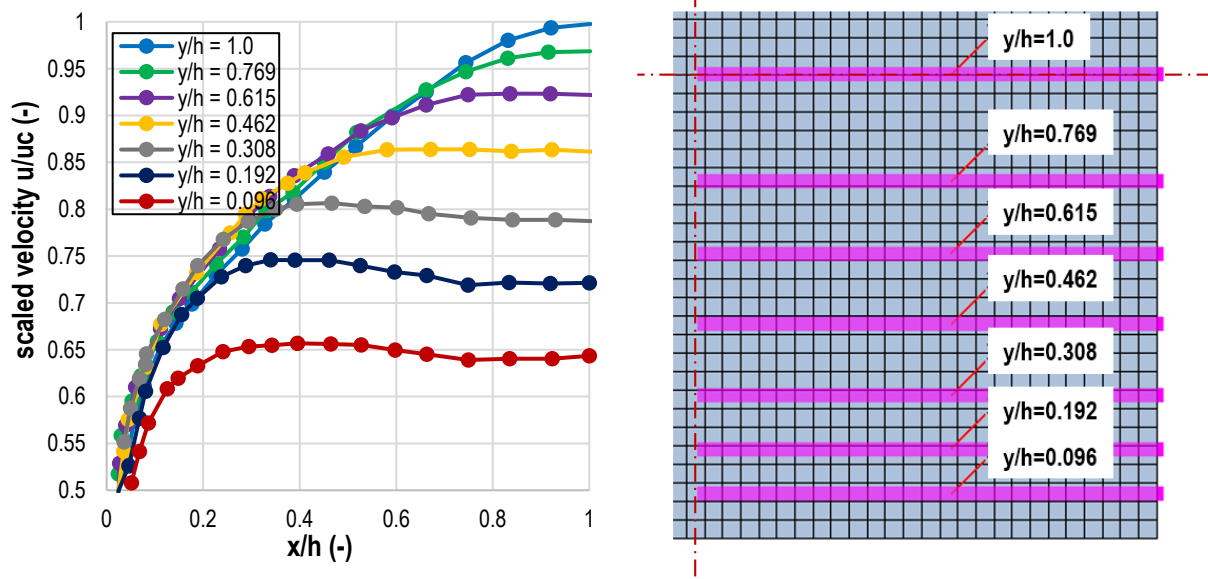


Figure 4.1. (Left) Digitized experimental axial velocity profiles at $x/D_h = 29.0$ (source [26]), and (right) locations of the measurements.

4.2 Description of the CFD Model

A CFD model of the rectangular duct, made of Perspex with dimensions 40 mm by 41 mm by 1.8 m, was built in STAR-CCM+. Three meshes were built with hexahedral structured mesh for various mesh densities near the walls, with y^+ in three ranges (see Figure 4.2):

1. $y^+ < 1$ with 90 x 90 elements in the cross section,
2. $1 < y^+ < 5$ with 70 x 70 elements in the cross section, and
3. $y^+ > 30$ with 50 x 50 elements in the cross section.

In the present study, the performance of the three mesh densities combined with five different turbulence models was tested. Out of all available turbulence models, the following five were used: realizable k-epsilon (RKE), k-omega (KW), k-omega SST with quadratic terms (KW-QCR), Reynold's stress with elliptic blending (RST-EB), and Reynold's stress with linear pressure-strain relationship (RST-LPS2L). Two-layer models were used for all cases (refer to Appendix A and to STAR-CCM+ documentation [33] for further descriptions of the turbulence models).

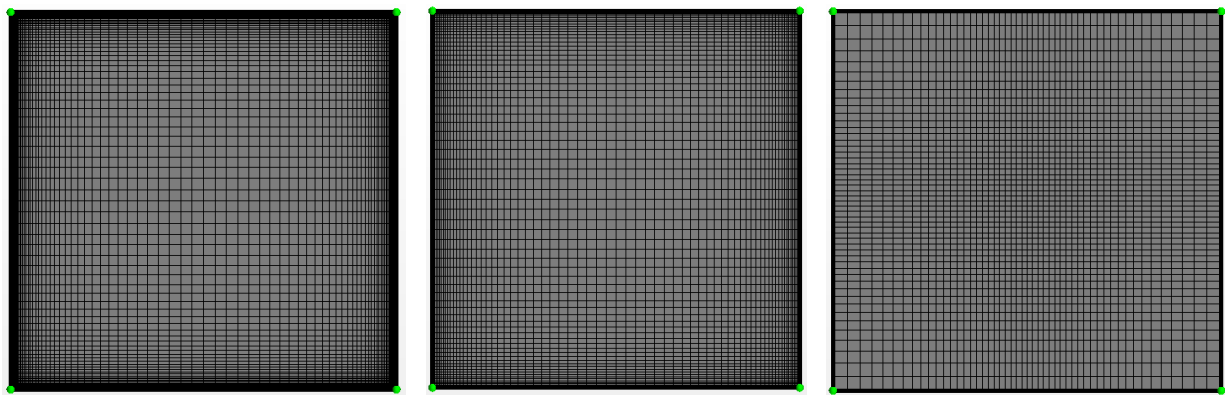


Figure 4.2. Cross section through three meshes used to model the duct in [26]: (left) 90 by 90 elements with near-wall element size of $y^+ < 1$, (center) 70 by 70 elements with $1 < y^+ < 5$, (right) 50 by 50 elements with $y^+ > 30$.

4.3 Results

The experiment reported by Melling and Whitelaw was performed for a relatively short duct. The flow is developing through its entire length, and, in fact, the fully developed state is not reached at the end of the duct. The authors state that the presence of the secondary flow effects is noticeable at x/D_h equal to about 20. In the cross sections upstream from this location, the characteristic distortions of the isovels are not present. For the same reason, the cross sections for which axial velocity profiles and velocity contours were reported (at various stages of the flow development) are not equivalent to each other.

Figure 4.3 shows velocity at the center of the duct, normalized by the bulk velocity, for various turbulence models with the near-wall mesh size $y^+ > 30$, compared to the experimental data. The experimental data were measured with two methods. In one of them, bulk velocity was calculated based on the flow rate. The result is plotted in the figure with a red solid line with markers. In the other method, the isovels at various cross sections were integrated to obtain the bulk velocity. This result is plotted with a black solid line with markers. Depending on the flow regime, and therefore on Re , this plot may have a peak, visible in the CFD results at $x/D_h \sim 30$, which flattens out once the flow is fully developed. The peak is more pronounced for high- Re flows [34]. The lack of a noticeable peak

in the experimental data used here for reference may be caused by the fact that the flow was not fully developed and there was a plenum at the outlet of the duct that could have affected the flow in the duct. This behavior was not explained in the source document [26].

The RST-EB turbulence model with near-wall mesh size $y^+ > 30$ predicted the highest velocity in the center of the duct, while the RST-LPS2L model predicted the lowest. The RKE and KW models predicted center velocities that were closest to the experimental data. The peak in the numerical plots occurred at various distances, ranging from $x/D_h = 28.7$ for the KW-QCR model to $x/D_h = 33.1$ for the RKE model.

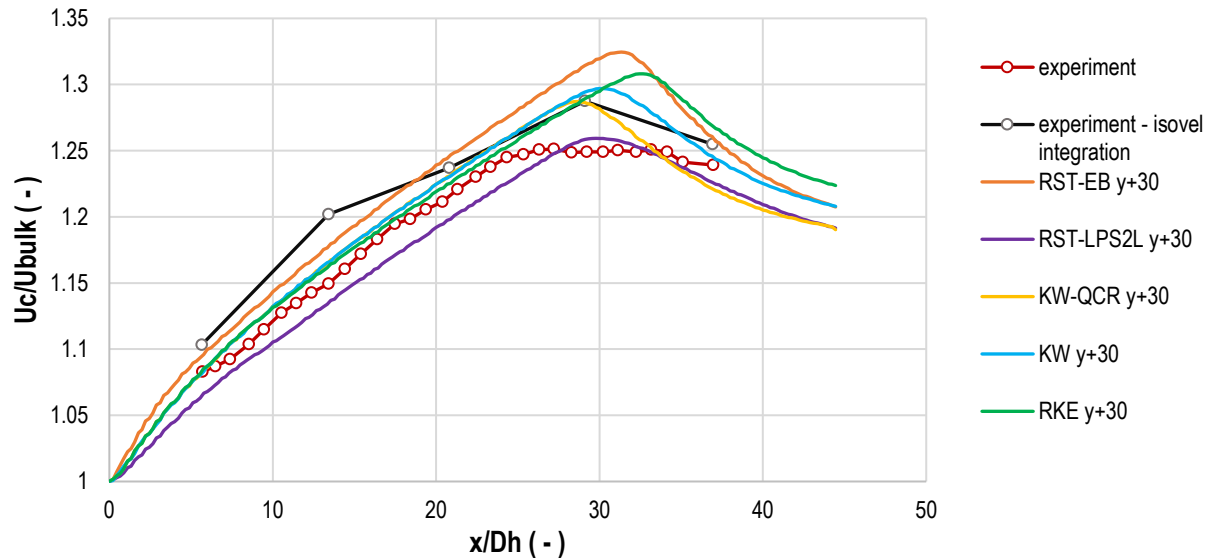


Figure 4.3. Scaled velocity at the center of the duct for various turbulence models and $y^+ > 30$, compared to the experimental data.

Figure 4.4 shows a similar plot, but this time only the RST-EB turbulence model was used for three meshes with various densities, because it predicted the most conservative result out of all turbulence models. For higher mesh densities, the duct-center velocity was lower, and closer to the experimental data, for the main part of the plot (before the peak), as compared to the velocities predicted by the mesh with a near-wall size of $y^+ > 30$.

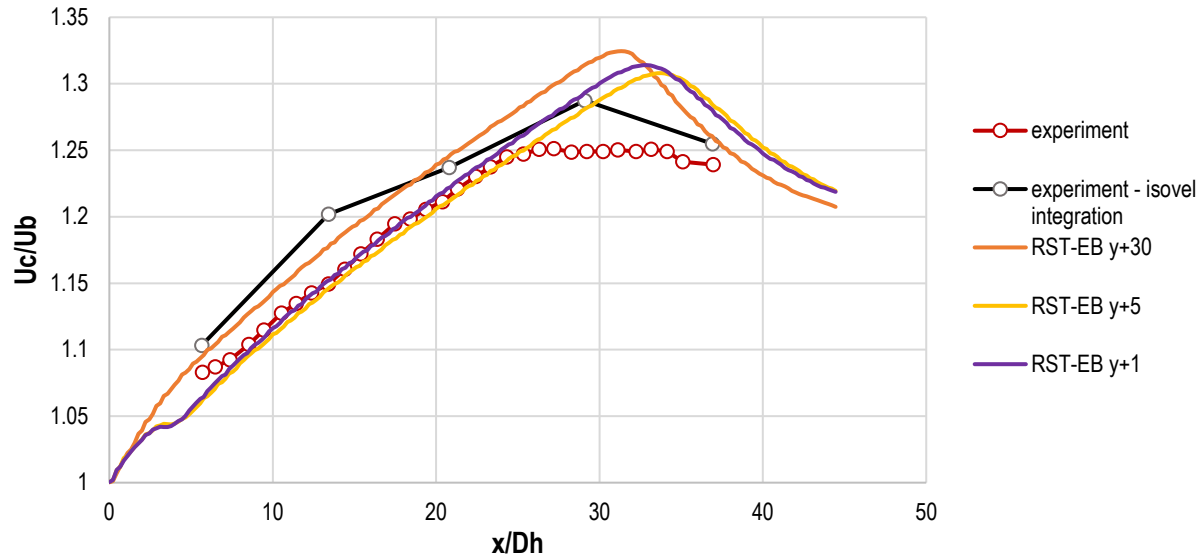


Figure 4.4. Scaled velocity at the center of the duct for the RST-EB turbulence model and various mesh densities, compared to the experimental data.

Figure 4.5 shows the vector plots of the secondary velocity field in the duct at $x/D_h = 36.8$ for various turbulence models. Only one-quarter of the duct cross section is displayed; the other quarters are mirror reflections of the one shown. The RS turbulence models, as well as KW-QCR, can predict the characteristic vortices directing flow from the center, along the bisectors of the corners, and then along the walls toward their midpoint and then back to the center of the duct. These flow patterns are all symmetric about the bisector of the corner and the lines halving the duct walls. This flow pattern causes distortion of the axial velocity and temperature fields in non-circular ducts. The linear isotropic turbulence models, RKE and KW, are not able to predict such flow patterns.

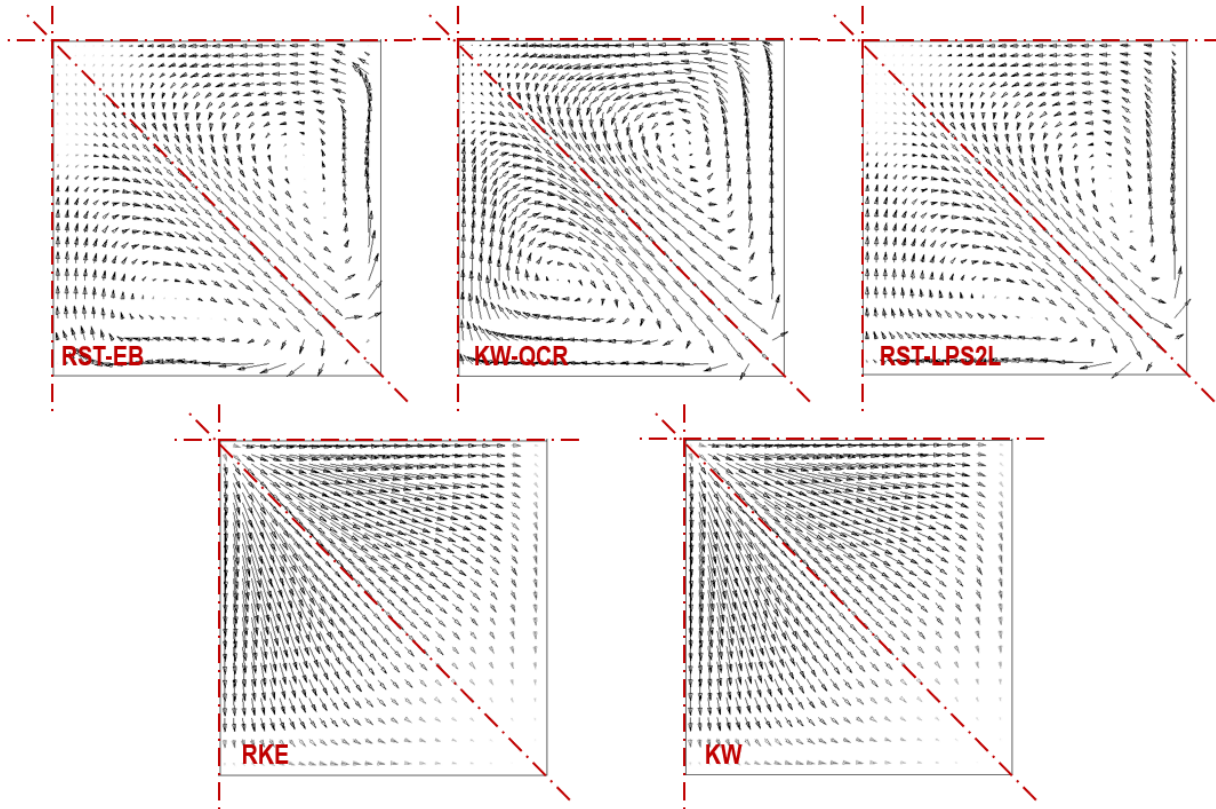


Figure 4.5. Vector plot of secondary velocity field in the duct at $x/D_h = 36.8$ for the five indicated models.

Figure 4.6, Figure 4.7, and Figure 4.8 present the constant-velocity contours in the cross section $x/D_h = 36.8$ for meshes with $y^+ > 30$, $1 < y^+ < 5$, and $y^+ < 1$, respectively. The flow in this cross section approaches the fully developed flow, but it is not yet fully developed. Each figure contains the cross sections from numerical models using different turbulence models. An eighth of the cross section (a symmetrical triangle) is replaced with a section of the plot from experimental data. The agreement between the simulated and the experimental data can be checked along the vertical and diagonal lines bounding the experimental data in the plot. It can be observed that the RST-EB and KW-QCR models show the best agreement for all y^+ ranges. These were closely followed by results from the RST-LPS2L model. RST-LPS2L is not suitable for meshes with $y^+ < 1$; thus, it should be used with caution. The isotropic turbulence models RKE and KW did not predict the distortions of the velocity field.

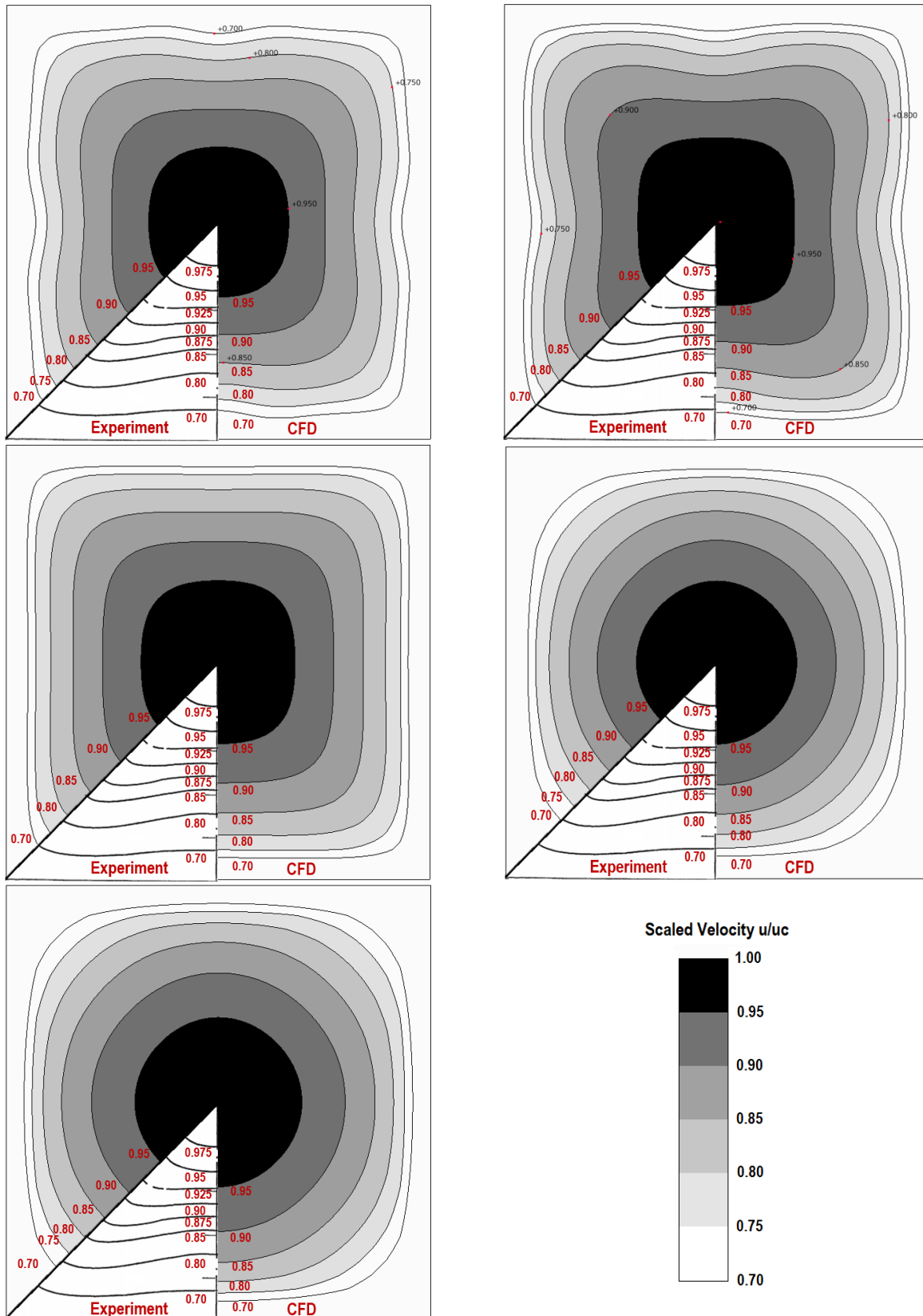


Figure 4.6. Constant-velocity contours for near-wall mesh size of $y^+ > 30$ compared to the experimental data, for (from the top left) RST-EB, KW-QCR, RST-LPS2L, RKE, and KW models.

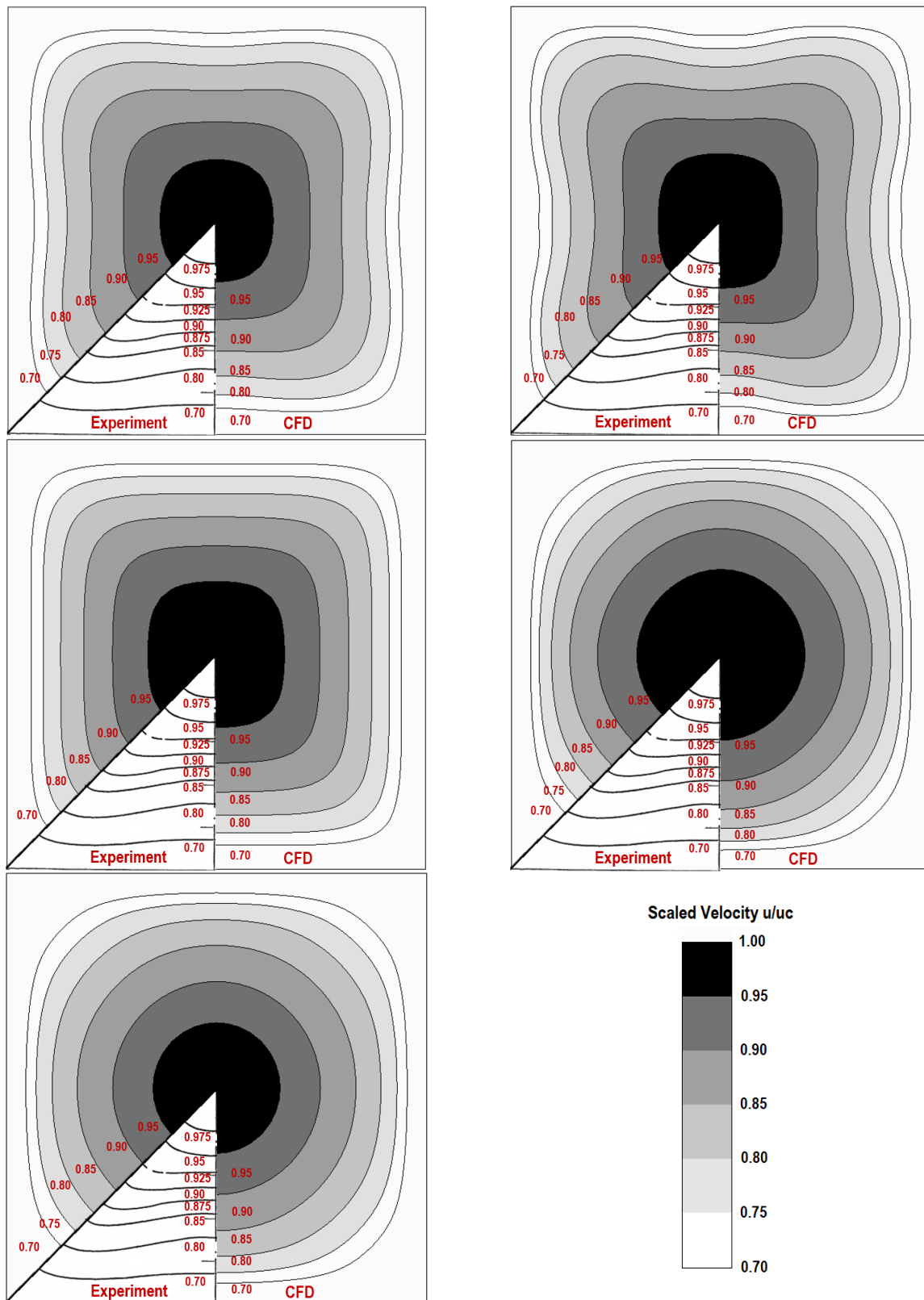


Figure 4.7. Constant-velocity contours for near-wall mesh size of $1 < y+ < 5$ compared to the experimental data, for (from the top left) RST-EB, KW-QCR, RST-LPS2L, RKE, and KW models.

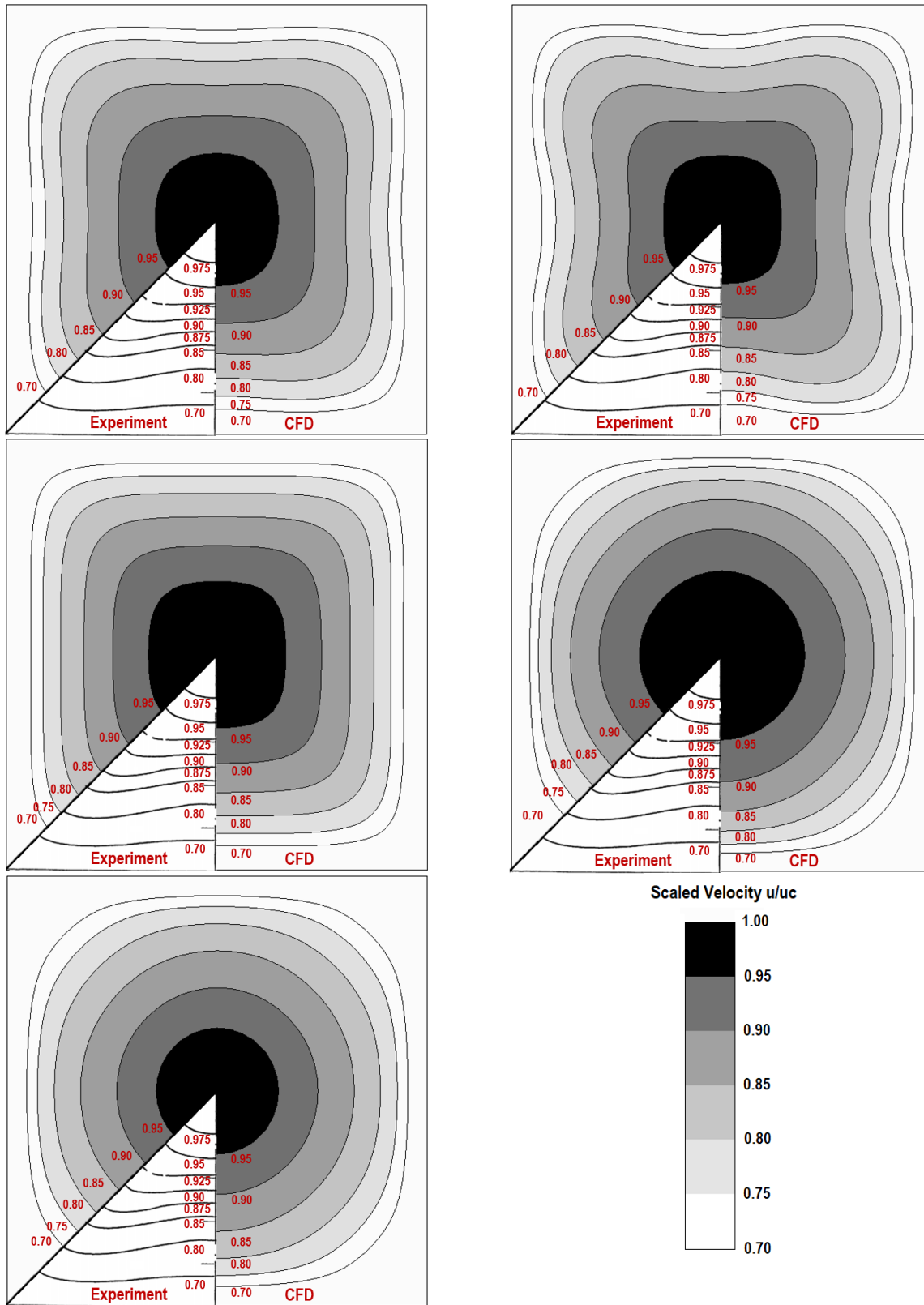


Figure 4.8. Constant-velocity contours for near-wall mesh size of $y^+ < 1$ compared to the experimental data, for (from the top left) RST-EB, KW-QCR, RST-LPS2L, RKE, and KW models.

Figure 4.9, Figure 4.10, and Figure 4.11 present plots comparing axial velocity profiles from various CFD models in the cross section $x/D_h = 29.0$ for meshes with $y^+ > 30$, $1 < y^+ < 5$, and $y^+ < 1$, respectively. As mentioned earlier, this is a cross section with developing flow. Each figure contains plots for five studied turbulence models. For all three near-wall densities, the best results are obtained from the model with RST-EB turbulence, followed by the KW-QCR model. The RST-LPS2L model worked reasonably well for the coarsest mesh, with $y^+ > 30$. The KW and RKE models significantly underestimated the flow velocities near the walls. It is important to note that although the RST-EB model gave the closest results to the experimental data, problems with its convergence were observed. While the other turbulence models gave converged results with 40 elements in the cross section, changes in the results were still noticed for the RST-EB model when higher densities in the duct cross section were used.

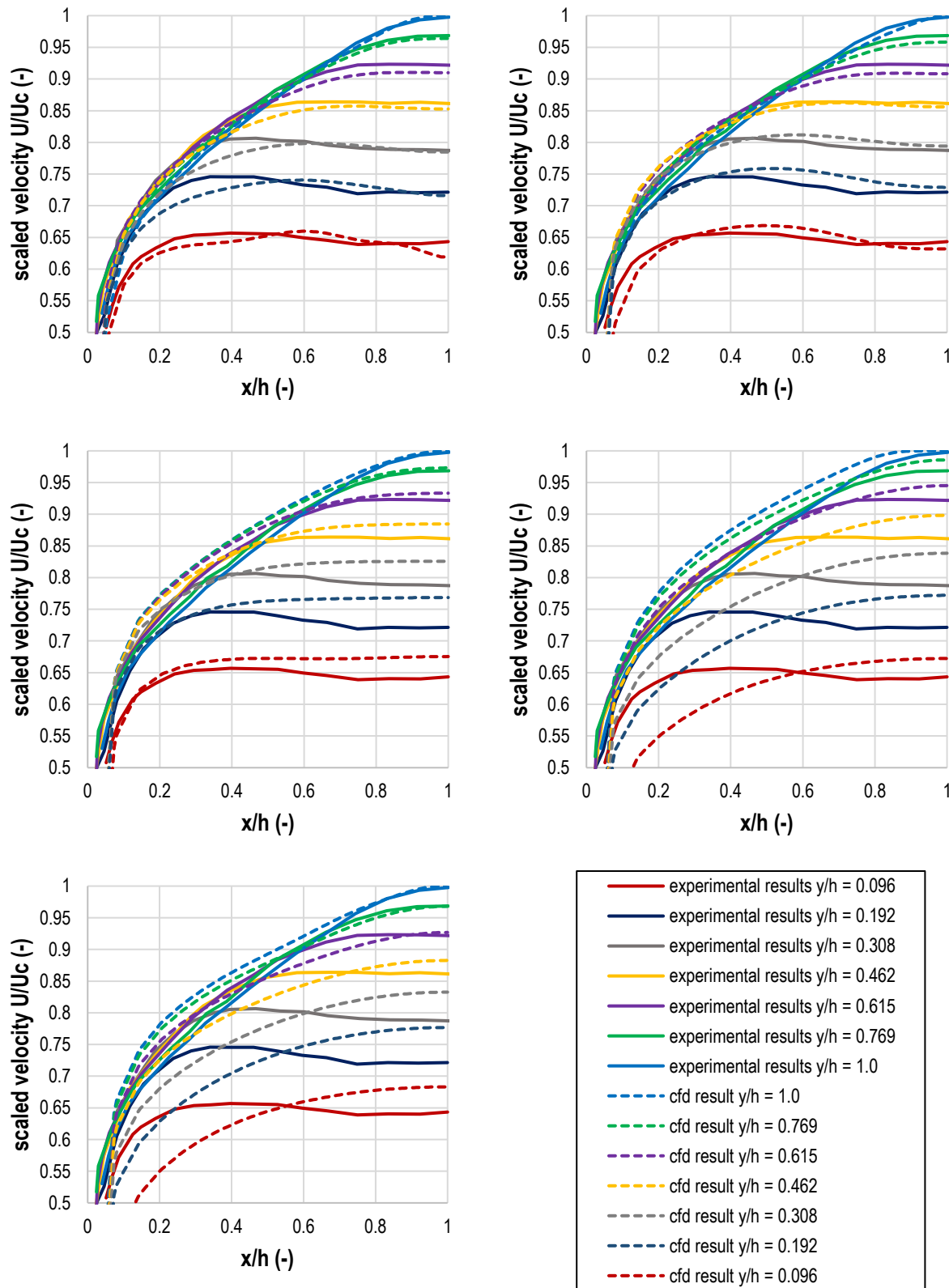


Figure 4.9. Axial velocity profiles for near-wall mesh size $y^+ > 30$ compared to the experimental data, for (from the top left) RST-EB, KW-QCR, RST-LPS2L, RKE, and KW models.

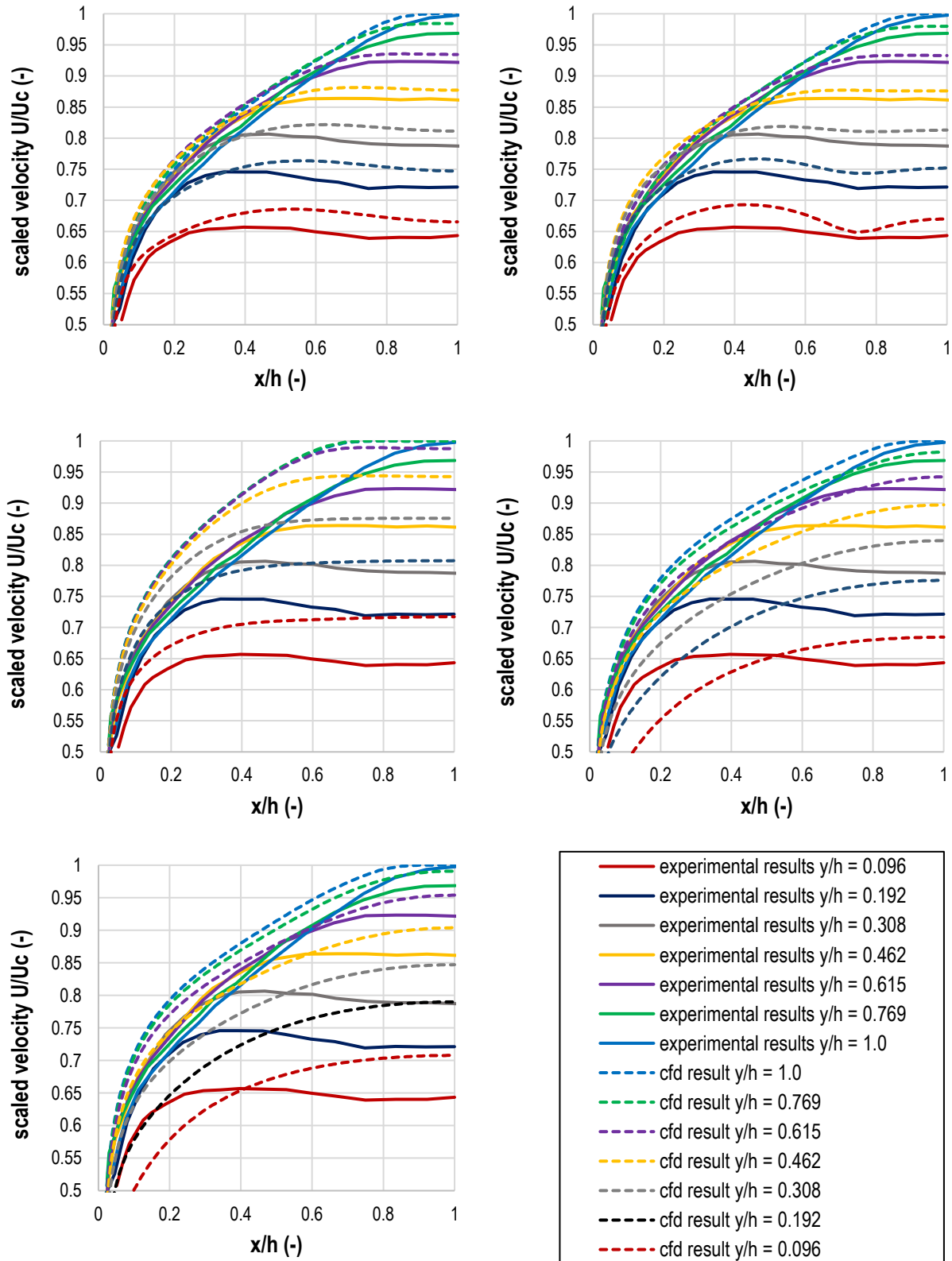


Figure 4.10. Axial velocity profiles for near-wall mesh size $1 < y^+ < 5$ compared to the experimental data, for (from the top left) RST-EB, KW-QCR, RST-LPS2L, RKE, and KW models.

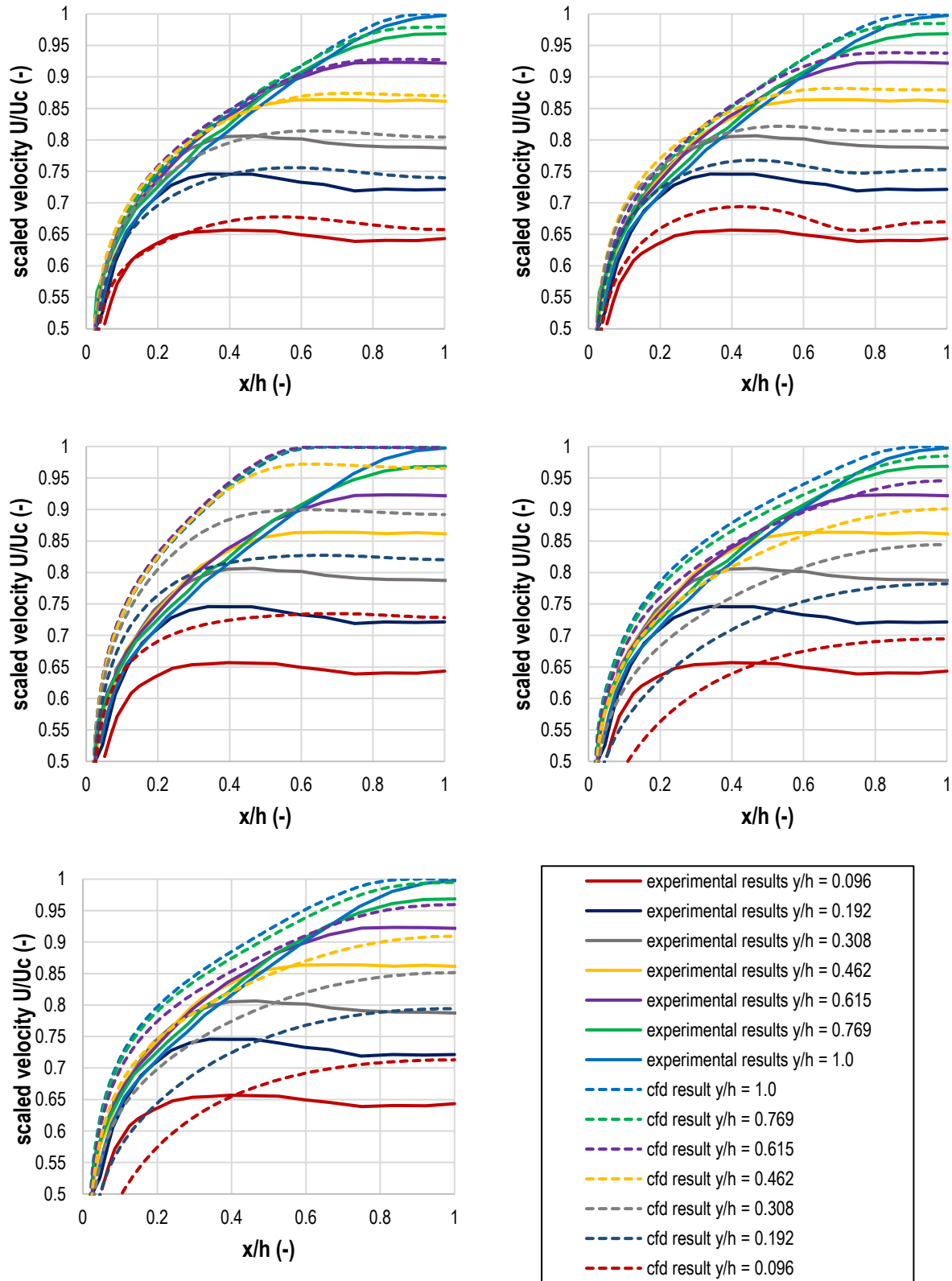


Figure 4.11. Axial velocity profiles for near-wall mesh size $y^+ < 1$ compared to the experimental data, for (from the top left) RST-EB, KW-QCR, RST-LPS2L, RKE, and KW models.

5 Simulations of the Experiment of Hirota et al.

5.1 Description of the Experiment

Among the abundance of experiments with isothermal flows, the experiment conducted by Hirota et al. [29] in 1996 is one of only a few that studied the characteristics of the turbulent temperature field for forced-convection heat transfer in a straight duct with a square cross section. These researchers showed similarities between the temperature field and the flow-velocity field, but also noted that the distortions of the mean temperature field were weaker than those of the mean velocity field. Contours of turbulent heat flux, eddy thermal diffusivity, and other characteristics of the flow were reported.

The experiment used a straight 4.77-m-long duct with a square cross section with inner dimensions of 50 mm by 50 mm. The length of the duct corresponds to $95.4 D_h$, where D_h is the hydraulic diameter. The duct was built of extruded aluminum with hydraulically smooth walls. A 1.75-m-long segment (corresponding to $35.0 D_h$) located toward the downstream end of the duct had its walls heated isothermally with a constant temperature of 373 K (100 °C) by saturated steam supplied between the inner and outer ducts. The measuring cross section was located 100 mm upstream from the duct outlet.

The authors did not directly provide the inlet velocity or the inlet bulk temperature of the air in [28]. However, a Re of 65,000 for the flow was given. Some of the missing input data were collected from other publications in which the same authors reported results of tests conducted at the same testing facility and duct dimensions, under the same flow regime, but with rough walls [35], [36]. It is assumed that many characteristics of the experimental setup were similar across all these experiments. These publications provide more key information that was missing in [29] used as the main reference in the current study. As reported in [36], the inlet temperature of the air ranged from 15.0 °C to 18.8 °C. That reference also reported that the accuracy of the wall-temperature measurements was 0.3 °C. Reference [35] listed values of physical properties of the air that were used in the calculations. The density of air at the inlet was assumed to be 1.184 kg/m³, while the kinematic viscosity was assumed to be 1.537×10^{-5} m²/s. The specific heat was assumed to be 1.0×10^3 J/kg·K. Based on these values, the average inlet velocity in the numerical models was estimated to be 19.98 m/s. All three references listed uncertainties of selected measurements, which are gathered in Table 5.1. It should be noted that the primary reference [28] for the present work does not list as many uncertainties as the other two. Thus, it is assumed that all the quantities of interest had a similar level of accuracy in the measurements across the experiments reported in [29], [35], and [36].

Table 5.1. Uncertainties in the heated-duct experiments of Hirota et al. and Fujita et al.

Quantity	Reference [29]	Reference [35]	Reference [36]
mean velocity, U_1	-	1.5 %	1.4 %
mean velocity, U_2	-	3.3 %	-
mean velocity, U_3	-	3.3 %	6.0 %
mean temperature, T	-	-	2.3 %
wall-temperature scattering, dT	0.3 °C	-	0.3 °C
heat flux, q	-	-	14.1 %

Figure 5.1 presents the isolines of the averaged mean velocity and the isolines of the scaled mean temperature obtained in the experiments. The scaling of the velocity was done with respect to the velocity in the center of the duct cross section, but the latter value, which is also the maximum velocity in the cross section, was not provided in any of the related publications. The centerline velocity can be roughly estimated based on previously estimated bulk velocity and the so called “1/7th power law”, which relates the bulk mean velocity to the maximum (center) velocity in a round duct according to the following equation:

$$\frac{U_{avg}}{U_c} = \frac{2n^2}{(n+1)(2n+1)} \quad (3)$$

where $n = 7$. The ratio of U_{avg} to U_c is estimated to be 0.817, which for this specific experiment and the bulk velocity of 19.981 m/s leads to an estimation of the center velocity ~ 24.47 m/s.

The scaling of the temperature, T , in the cross section uses the constant temperature on the wall, T_w , as well as the value of the temperature in the center of the duct, T_c , according to the formula:

$$\bar{T} = \frac{T_w - T}{T_w - T_c} \quad (4)$$

The temperature in the center of the duct also was not reported in the available references. The magnitude of the maximum values of temperature and velocity is affected by two measurements: the exact estimation of the center position in the duct and the measurement of the velocity or the temperature itself. For highly turbulent flows, the velocity profile in the cross section is rather flat, and the measurement of the maximum velocity is not particularly sensitive to the position of the measurement. However, because only the scaled data are presented without the raw measurements, additional uncertainties are introduced in the results.

The results from reference [29], in the form of the isolines of velocity and temperature in one-fourth of the cross section, were used as a base for comparison with the CFD simulation results and are presented in Figure 5.1. Two other references, [36] and [37], provide an alternative set of isolines from the same or similar tests performed by the same authors at the same testing facility.

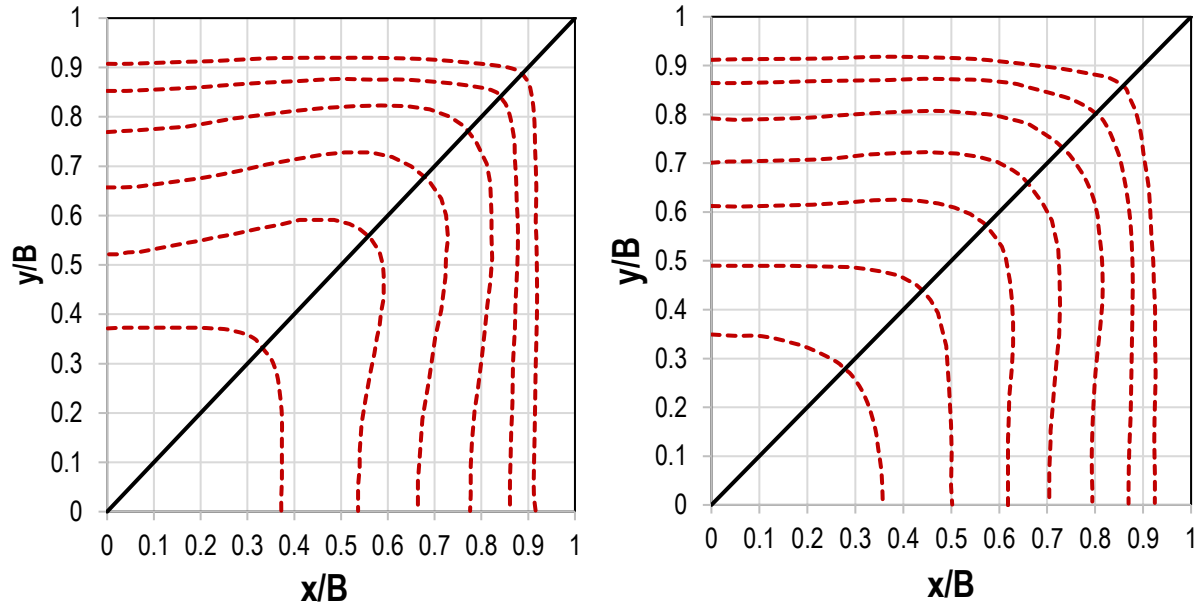


Figure 5.1. Isolines in the testing section: (left) scaled velocity and (right) scaled temperature [29].

The accuracy of comparisons of the numerical results with the experimental isoline plots in general is rather low. In other words, it is not the best validation metric if the raw data for their construction is not available. However, for quantitative comparison of the simulated results with the experiments, Figure 5.2 and Figure 5.3 can be used instead. They present the experimental data for the velocity and temperature distributions, respectively, normalized by wall parameters measured along five cross sections of the duct, which are presented in Figure 5.4.

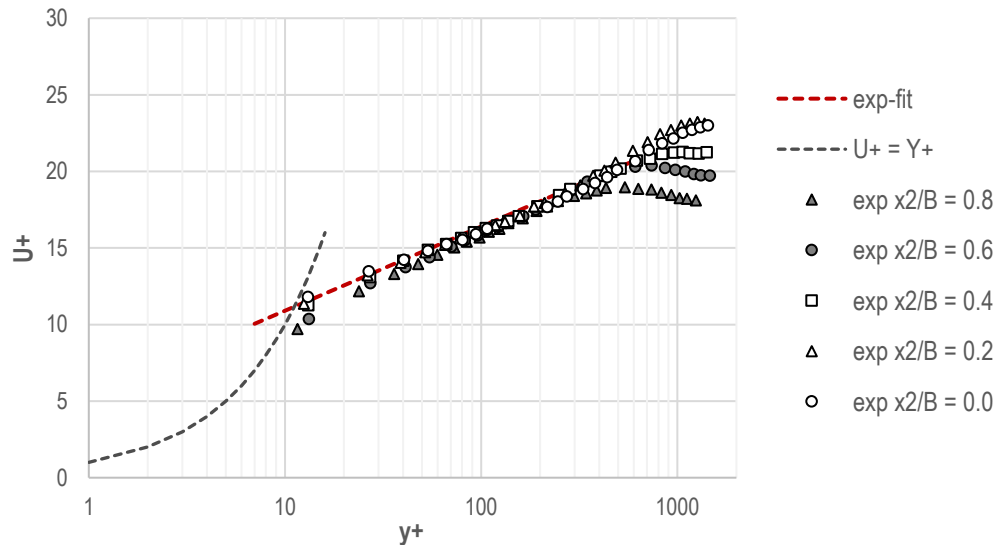


Figure 5.2. Mean primary flow velocity distribution in wall parameters [29].

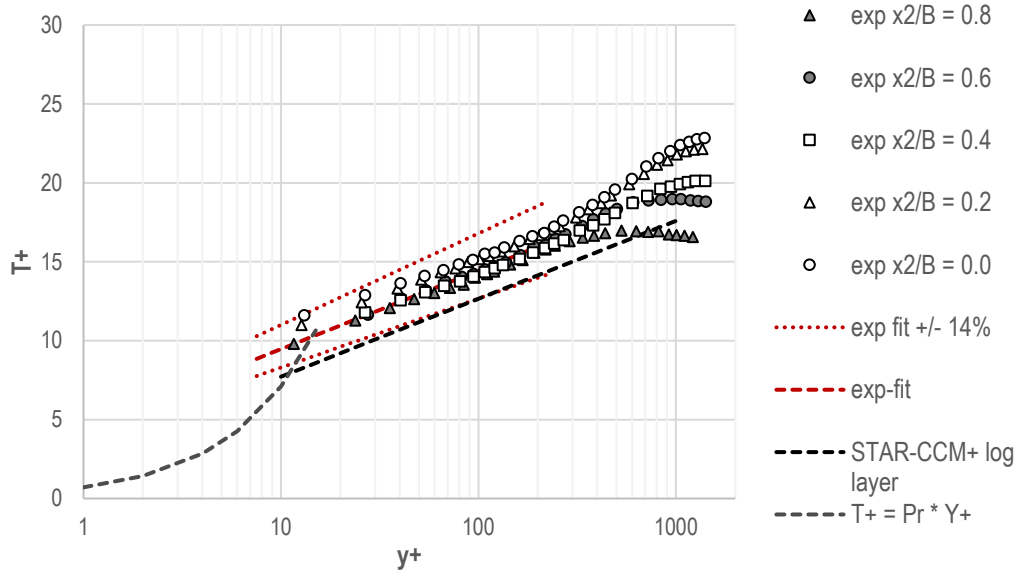


Figure 5.3. Mean temperature distribution in wall parameters [29].

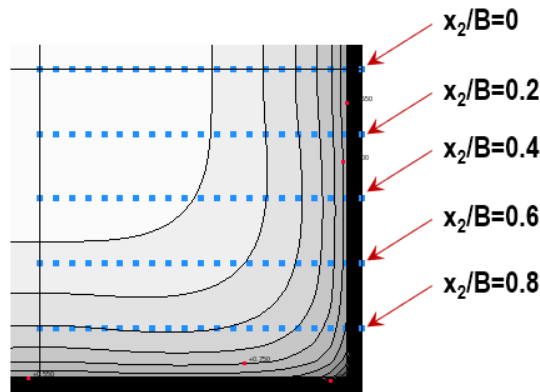


Figure 5.4. Locations of the data-gathering lines in the duct cross section for Ref. [29].

The experimental fit in Figure 5.2 is based on Sarnecki's formula, which is valid for the interval $30 < y^+ < 300$ [29]:

$$U^+ = 5.5 \cdot \log y^+ + 5.4. \quad (5)$$

The experimental fit for the temperature measurements presented in Figure 5.3 is based on a similar formula [29]:

$$T^+ = 4.98 \cdot \log y^+ + 4.48. \quad (6)$$

As pointed out in Table 5.1, the uncertainty of measurements of the wall heat flux is $\pm 14.1\%$. For that reason, $\pm 14.1\%$ bands around that fit were also added.

Figure 5.3 also contains a line representing the standard wall function used in STAR-CCM+ [33], which is defined as

$$T^+ = Pr_t \left(\frac{1}{\kappa} \cdot \ln(E' \cdot y^+) + P \right), \quad (7)$$

where Pr_t is the turbulent Prandtl number, equal to 0.9; κ is the von Karman constant, equal to 0.42; E' is defined as E/f , where E is log law offset, assumed to be 9.0, and f is the roughness function, assumed to be 1 for smooth walls; and P is defined as follows:

$$P = 9.24 \cdot \left[\left(\frac{Pr}{Pr_t} \right)^{\frac{3}{4}} - 1 \right] \left[1 + 0.28 \exp \left(-0.007 \frac{Pr}{Pr_t} \right) \right]. \quad (8)$$

For $Pr_t = 0.9$ and $Pr = 0.71$, P is calculated to be -1.925.

5.2 Description of the CFD Model

The CFD models were built in a similar fashion to the other models developed for the isothermal experiments of Launder and Ying [24] and Melling and Whitelaw [26] as presented in Sections 3 and 4, respectively. Out of the entire apparatus, only the unheated 3.02-m-long and the heated 1.75-m-long portions of the duct were included in the model. An assumption was made that the settling chamber installed upstream from the unheated section delivered a uniform velocity profile in the experiment. The unheated and heated sections were modeled as separate regions in STAR-CCM+ software to preserve separate access to the boundary surfaces as well as the mesh settings for both sections. The inlet bulk velocity was set in accordance with the previously estimated value of 19.981 m/s. The average air temperature at the inlet was assumed to be 16.9 °C, which is a simple average between the top and bottom of the range reported in [36]. A constant temperature of 99.85 °C (373 K) was applied on the walls of the heated section.

Similarly to the simulations of the two experiments presented in Sections 3 and 4, three ranges of the near-wall mesh were considered in the models. Figure 5.5 presents cross sections in the models with nondimensional near-wall mesh sizes $y^+ < 1$, $y^+ < 5$, and the coarsest one with $y^+ > 30$. Note that the same size of near-wall cells yields slightly different resultant y^+ values for various turbulence models. For some of them, the size of the first layer of the cells had to be adjusted to keep the near-wall y^+ mesh size within the targeted ranges. A minimum of 50 cells across the duct section were required to obtain converged results for the mesh size of $y^+ > 30$. For the mesh with $y^+ < 5$, 100 cells across the duct section were used, with nonuniform sizes starting from 0.1 mm near the walls and 1.0 mm in the center of the duct. For the finest mesh, 130 cells across the duct section were used, with nonuniform sizes starting from 0.0125 mm near the walls and 1.1 mm in the center of the duct. Two hundred cells along the main air-flow direction in the heated portion of the duct were sufficient to obtain converged results. For all three cases, the mesh in the unheated portion of the duct was built of a coarser mesh with $y^+ > 30$, and 200 cells, for a total of 400 cells in the flow direction along the entire model. The mesh density in the unheated region did not affect the solution in the test section located 1.0 m away from the outlet of the heated section of the duct.

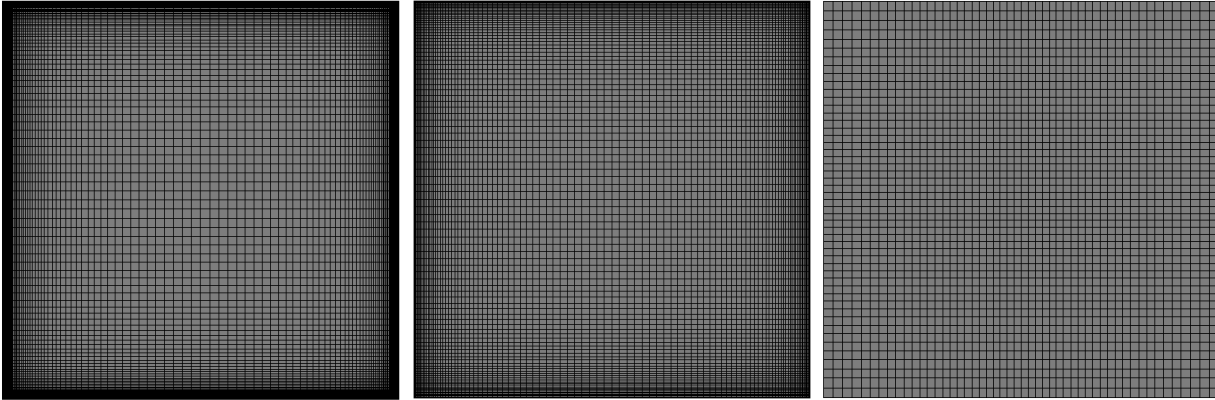


Figure 5.5. Cross-sections through the mesh used to model the duct in [29]: (left) fine, with $y^+ < 1$; (center) medium, with $1 < y^+ < 5$; and (right) coarse, with $y^+ > 30$.

The gradient of the temperatures across the duct cross section required that the air properties in the simulations be assumed as temperature dependent. Within the ranges of temperatures considered, i.e., from room temperature up to 100 °C, and under atmospheric pressure, these properties can be approximated as linear functions of the temperature. These linear functions are presented in Appendix B.

Out of all available RANS turbulence models, seven were considered in this part of the study (see Table 5.2): realizable k-epsilon (RKE), cubic standard k-epsilon (SKE-CUBIC), k-omega SST with quadratic terms (KW-QCR), k-omega SST with cubic terms (KW-CUBIC), Reynolds's stress with elliptic blending (RST-EB), Reynolds's stress with linear pressure strain relationship (RST-LPS2L), and Reynolds's stress with quadratic pressure-strain relationship (RST-QPS). Two-layer models were used for all cases whenever possible (refer to Appendix A and STAR-CCM+ documentation [33] for further descriptions of the turbulence models).

Table 5.2. Matrix of runs for the simulations of the experiment of Hirota et al. [29].

	$y^+ < 1$	$1 < y^+ < 5$	$y^+ > 30$
RKE	✓	✓	✓
SKE-CUBIC	✓	✓	✓
KW-QCR	✓	✓	✓
KW-CUBIC	✓	✓	✓
RST-EB	✓	✓	✓
RST-QPS	✗	✗	✓
RST-LPS2L	✓	✓	✓

It was found that the segregated solver was producing poorly converged results for some of the RS turbulence models. For that reason, all the results were produced with the coupled solver. For those turbulence models that converged well with both solvers, the differences in the results were indistinguishable.

5.3 Results

Figure 5.6 presents the local wall heat flux on $1/8^{\text{th}}$ of the wall in the models with $y^+ > 30$. The simulated results are compared to the experimental data of Hirota et al. [29], the experimental data of Brundrett and Burroughs [38], and the prediction by Nakahama with suppressed secondary flows that is included in [36]. The results for all turbulence models were split into two separate graphs in

Figure 5.6 for easier identification of each case. The upper graph in Figure 5.6 presents results for the k-epsilon and k-omega turbulence models and their variants. In that group, the closest results to the experimental data were obtained with the SKE-CUBIC model with modified turbulence coefficients, closely followed by the KW-QCR model. The shape of the curve predicted by the RKE model resembles the one obtained by Nakayama for calculations with suppressed secondary motions. The lower graph in Figure 5.6 contains results obtained with the three RS turbulence models. RST-EB gave the closest results to the experimental data. Out of all the plots presented in the two figures, SKE-CUBIC gave the best estimate of the heat flux. Nevertheless, as mentioned earlier, this is a model with modified turbulence coefficients and as such, is not usually recommended for use, because tuning of the coefficients requires a vast range of experiments to ensure their universality.

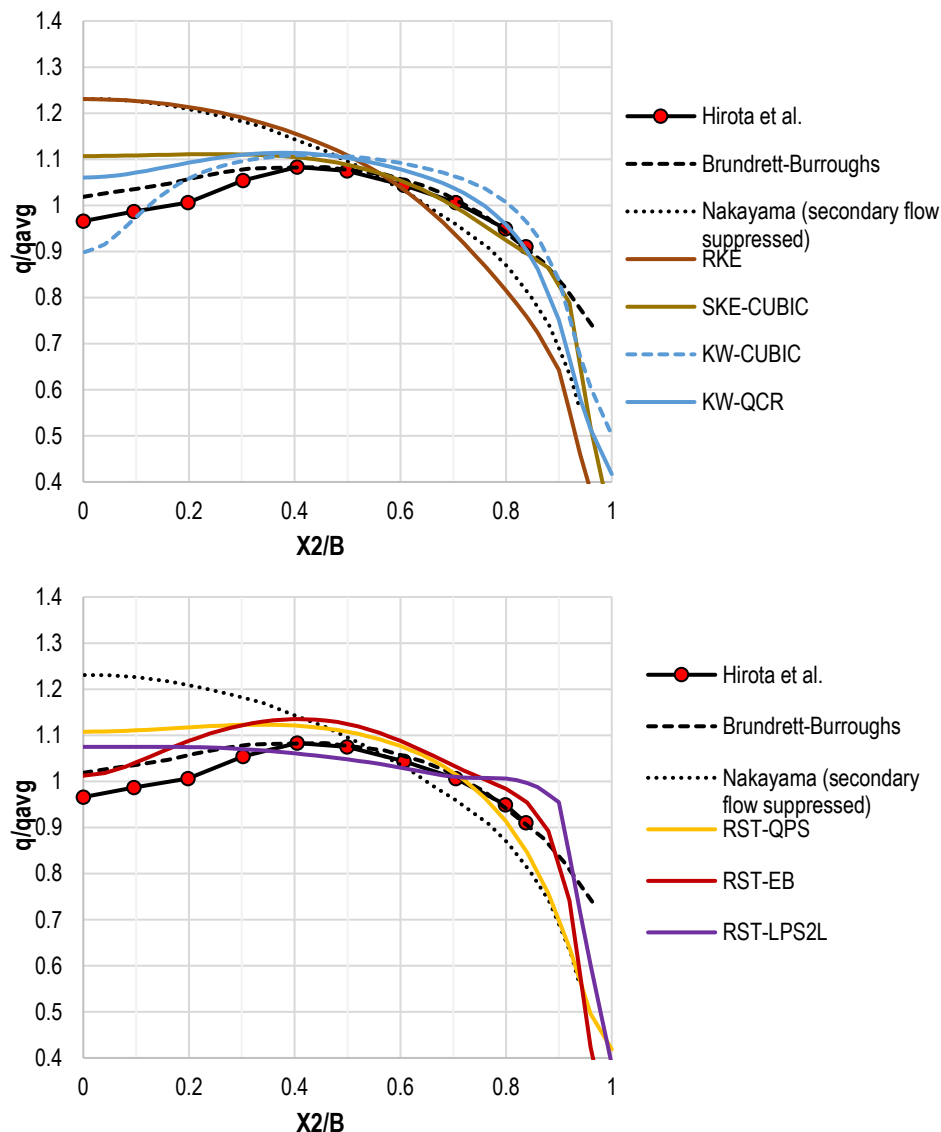


Figure 5.6. Local wall heat flux on 1/8th of the wall in models with near-wall mesh size $y^+ > 30$.

Figure 5.7 to Figure 5.13 show pairs of results for scaled velocity and scaled temperature in a quarter of the duct for each of the analyzed turbulence models. The velocity is scaled by the maximum value

in the center, while the temperatures are scaled according to Eq. (4). Experimentally obtained isolines are overlaid on top of the numerical plots with red dashed lines. The linear KE turbulence model (RKE, Figure 5.7) performed the worst out of all the tested models. Similar performance was obtained with other linear eddy viscosity models, including SKE and KW, and based on that performance, these turbulence models were not further investigated. RKE was assumed to be a good representative of that class of turbulence models. However, the quadratic k-omega model, KW-QCR (Figure 5.9), captured the isolines of the temperatures quite well, although it was not able to capture significant distortions in the velocity field present in the experimental data. The only turbulence model that was able to capture these distortions in the velocity field was KW-CUBIC (Figure 5.10), which was not used in the simulations of isothermal experiments. The simulations with this turbulence model and denser mesh did not converge well. Also, in the simulations with KW-CUBIC, symmetry in the flow field was not always achieved. Despite its good performance in this case, it is not recommended for general use and should be used with caution. The SKE-CUBIC model (Figure 5.8) performed better than the RKE model (Figure 5.7), but neither the velocity nor the temperature isolines were captured properly in the simulations with this turbulence model.

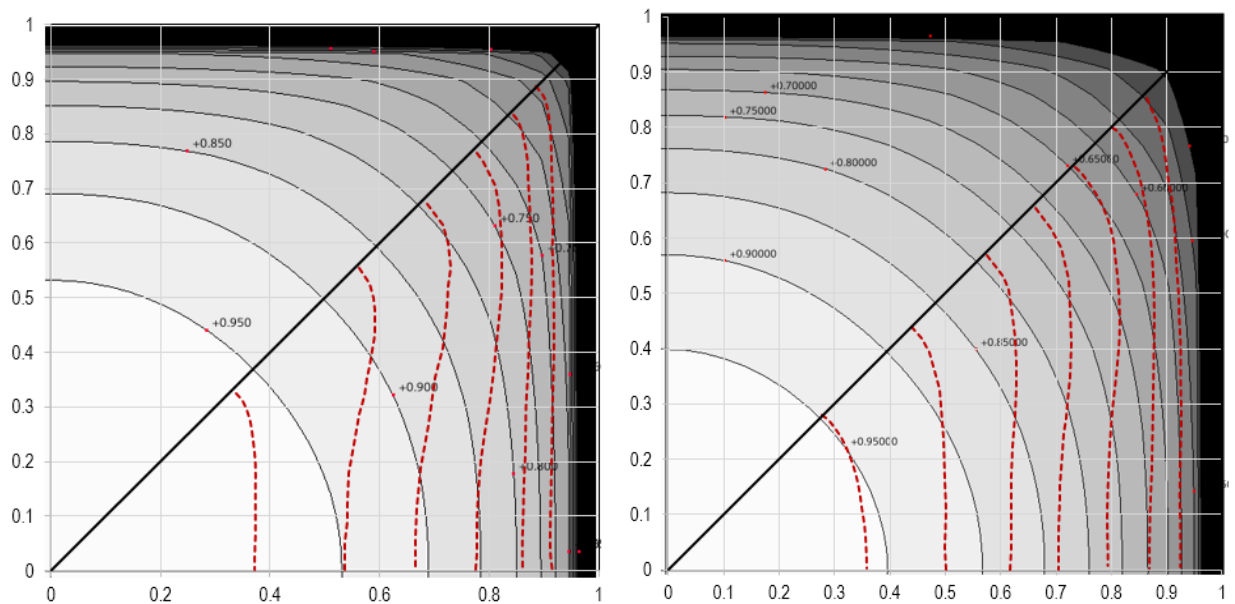


Figure 5.7. Constant velocity (left) and temperature (right) contours for near-wall mesh size of $y^+ > 30$ compared to the experimental data for the RKE turbulence model. Experiment - red dashed lines, CFD - black solid lines.

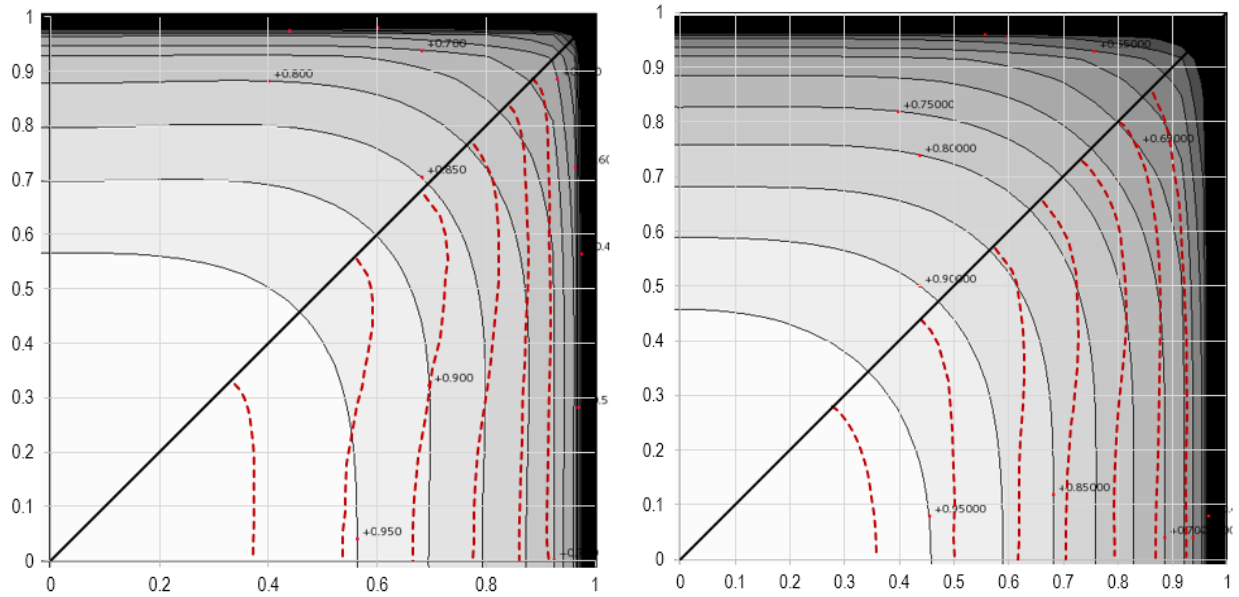


Figure 5.8. Constant velocity (left) and temperature (right) contours for near-wall mesh size of $y^+ > 30$ compared to the experimental data for the SKE-CUBIC turbulence model. Experiment - red dashed lines, CFD - black solid lines.

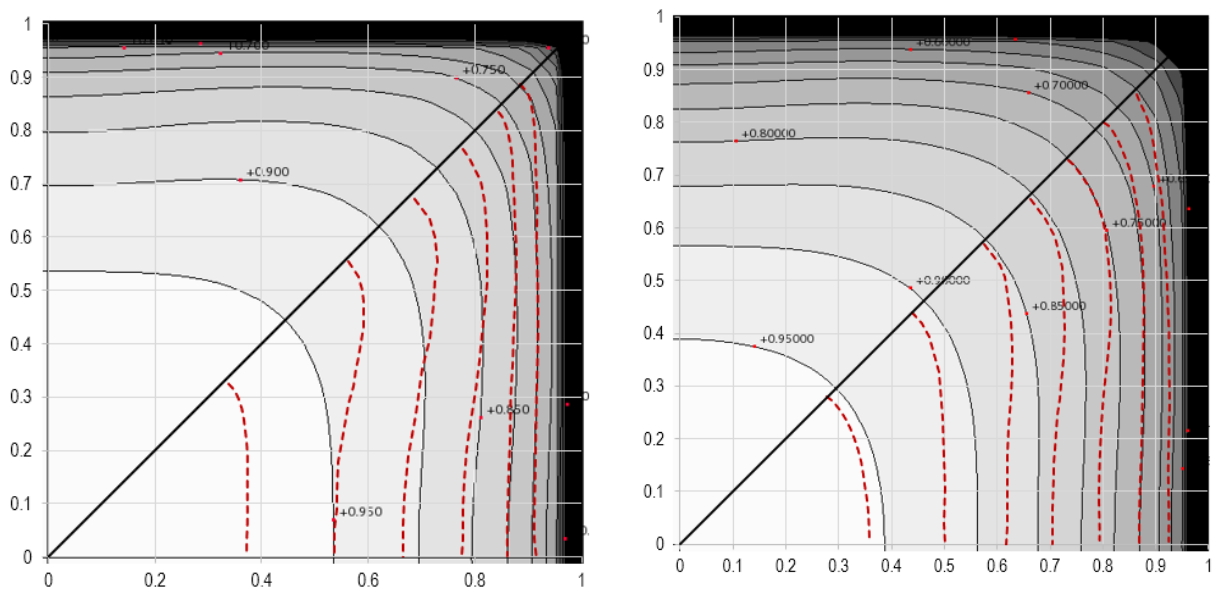


Figure 5.9. Constant velocity (left) and temperature (right) contours for near-wall mesh size of $y^+ > 30$ compared to the experimental data for the KW-QCR turbulence model. Experiment - red dashed lines, CFD - black solid lines.

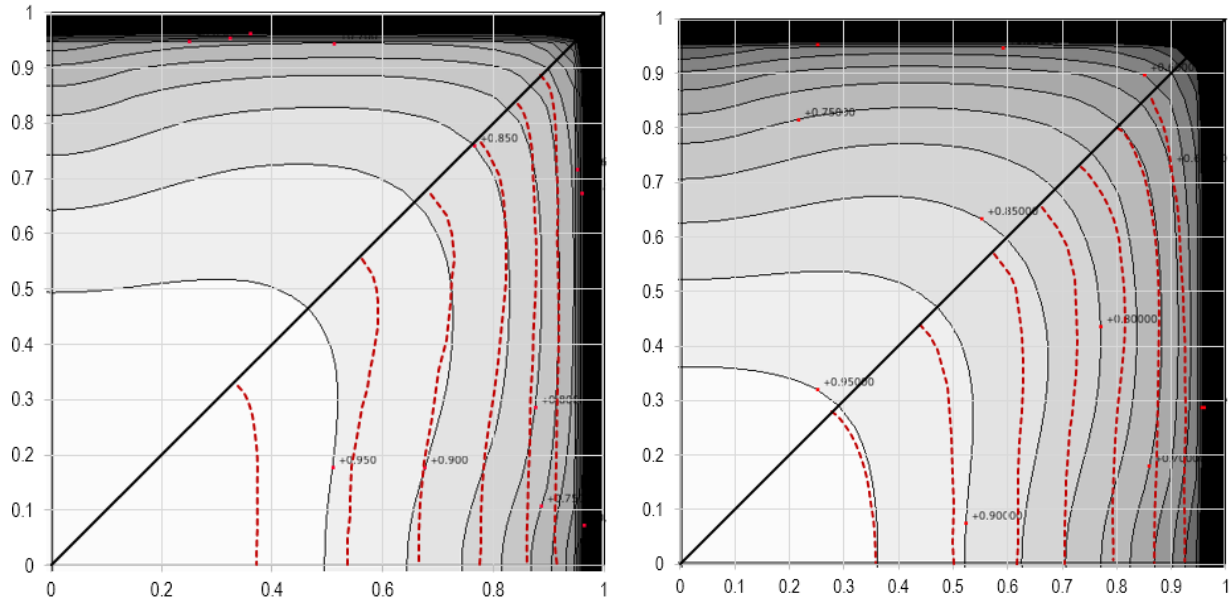


Figure 5.10. Constant velocity (left) and temperature (right) contours for near-wall mesh size of $y^+ > 30$ compared to the experimental data for the KW-CUBIC turbulence model. Experiment - red dashed lines, CFD - black solid lines.

Both RS turbulence models RST-EB and RST-LPS2L predicted the distribution of the temperature field in the testing section reasonably well, but the velocity field did not show the same level of distortions near the corners as was reported in the experiment.

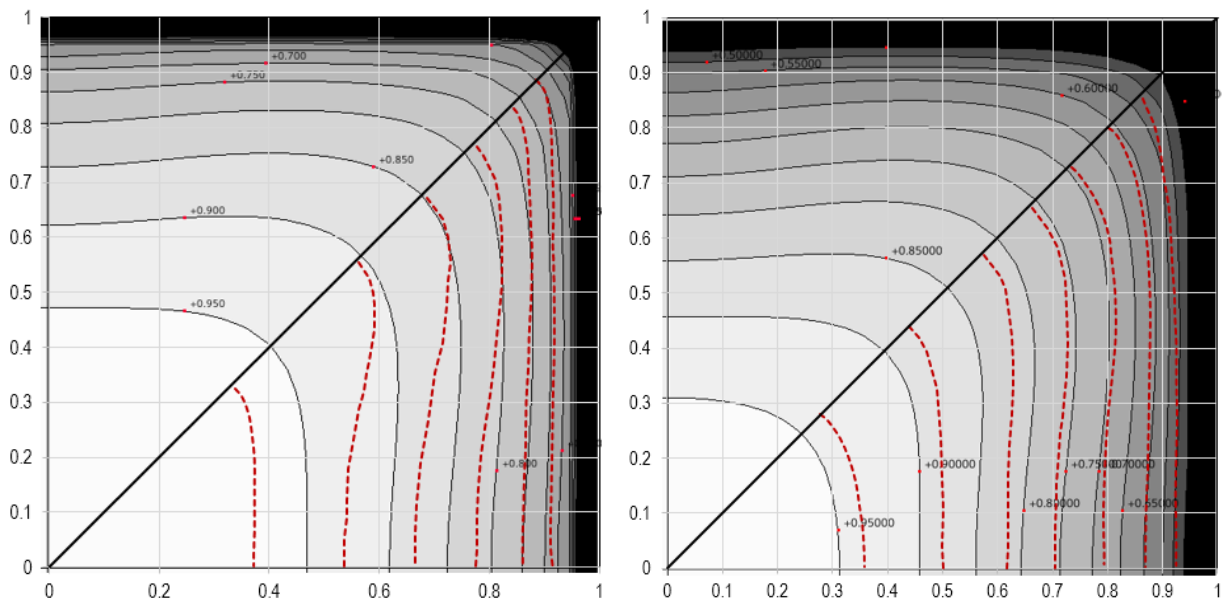


Figure 5.11. Constant velocity (left) and temperature (right) contours for near-wall mesh size of $y^+ > 30$ compared to the experimental data for the RST-EB turbulence model. Experiment - red dashed lines, CFD - black solid lines.

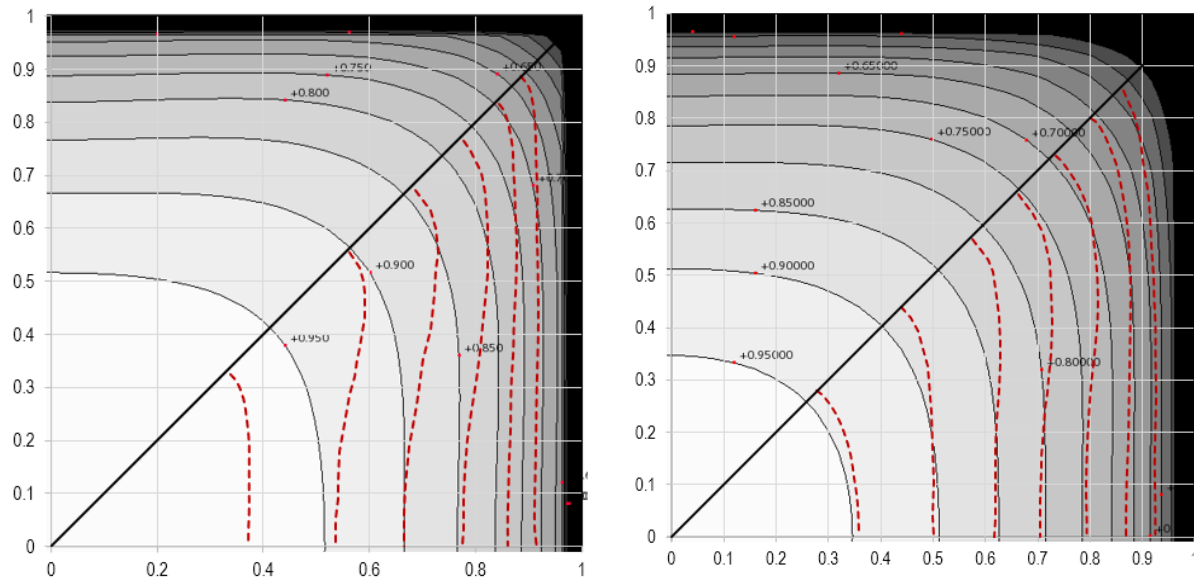


Figure 5.12. Constant velocity (left) and temperature (right) contours for near-wall mesh size of $y^+ > 30$ compared to the experimental data for the RST-QPS turbulence model. Experiment - red dashed lines, CFD - black solid lines.

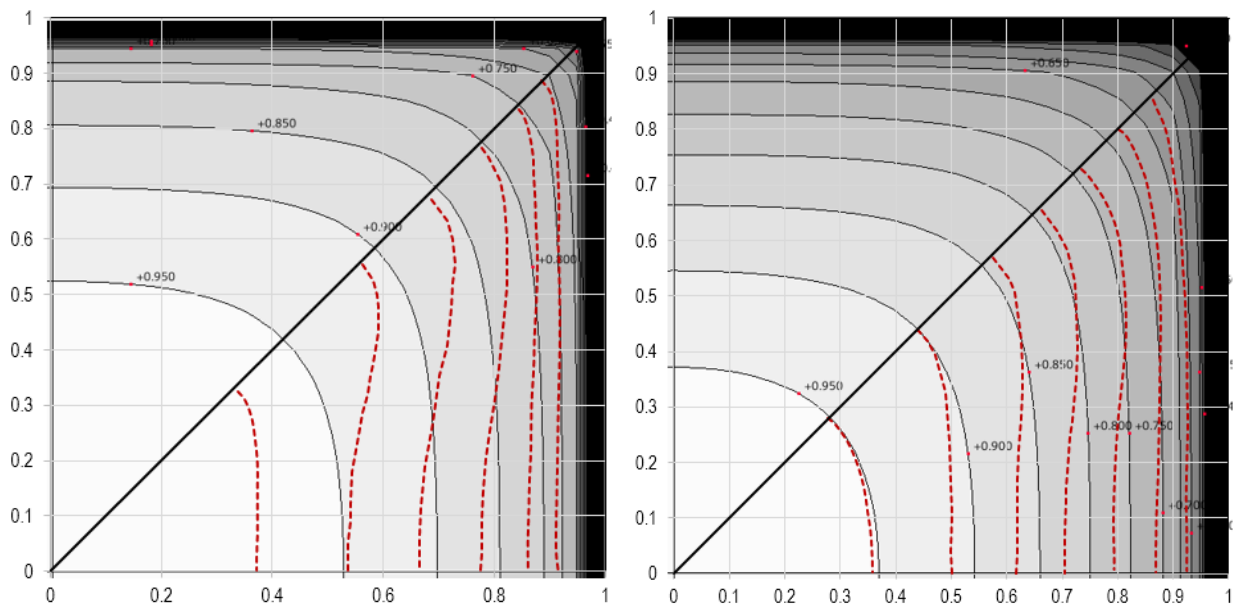


Figure 5.13. Constant velocity (left) and temperature (right) contours for near-wall mesh size of $y^+ > 30$ compared to the experimental data for the RST-LPS2L turbulence model. Experiment - red dashed lines, CFD - black solid lines.

Table 5.3 compares the center velocity, as predicted by the CFD simulations with near-wall mesh size $y^+ > 30$, with estimations of the experimental velocity (based on the $1/7^{\text{th}}$ -power law and Re). The center velocity in the simulations varies from 24.64 m/s to 25.80 m/s. These values are all above the estimation of the velocity magnitude from the experiment. As pointed out earlier, this value was not given explicitly in any of the references, and its estimation may be affected by the following factors:

1. The uncertainty in measurement of the velocity itself,
2. The accuracy of the positioning of the channel center,
3. The assumption of the kinematic viscosity needed for estimation of bulk velocity from the Re definition, and
4. The validity of the “1/7th-power law” for square ducts.

The uncertainty of the mean velocity measurement in the experiment was only $\pm 1.5\%$ (see Table 5.1); therefore, factor #1 should not have a significant influence on the solution. In highly turbulent flows, the velocity profile becomes rather flat in the center of the ducts; thus, the positioning of the center (factor #2) also should not be the primary driver of the uncertainties. However, factors #3 and #4 may contribute to a substantial error in the estimation performed in the current study. For these reasons, the estimation of the center velocity in the experiment should be taken not as a statistical mean value but rather as a crude estimate.

In the results presented here, for each turbulence model, a different center value of velocity and temperature was predicted. Table 5.3 presents these values together with the experimental estimation. The mean of the maxima obtained from the simulations was 25.23 m/s, with a standard deviation of 0.41 m/s. Center velocities predicted in the simulations were all higher than the estimated experimental value. To illustrate the influence of that discrepancy, Figure 5.14 was created with three plots of velocity isolines from the simulation with the KW-QCR turbulence model and the near-wall mesh size $y^+ > 30$. In the three plots, the simulated velocity isolines were scaled by (i) the center velocity decreased by the standard deviation (25.23 m/s – 0.41 m/s = 24.82 m/s), (ii) the computational average velocity of 25.23 m/s, and (iii) the center velocity increased by the standard deviation (25.23 m/s + 0.41 m/s = 25.64 m/s). The isolines obviously preserve the shape, but their locations in the cross section are vastly different. The comparison presented here shows that the velocity profiles scaled by the center (or maximum) velocity are highly sensitive to that center value. Also, without the knowledge of that center location (or better yet, the bulk velocity at the inlet) in the experiment, the isolines of velocity are not the best source of data for CFD model validation.

Table 5.3. Comparison of the center velocity in the experiment and simulations from models with wall $y^+ > 30$ and various turbulence models.

Source		Center velocity (m/s)
Experimental estimate		~24.47
CFD turbulence model	SKE-CUBIC	25.01
	RKE	25.80
	KW-QCR	24.99
	KW-CUBIC	24.80
	RST-EB	25.64
	RST-QPS	25.50
	RST-LPS2L	24.64
	computational average	25.23 \pm 0.41

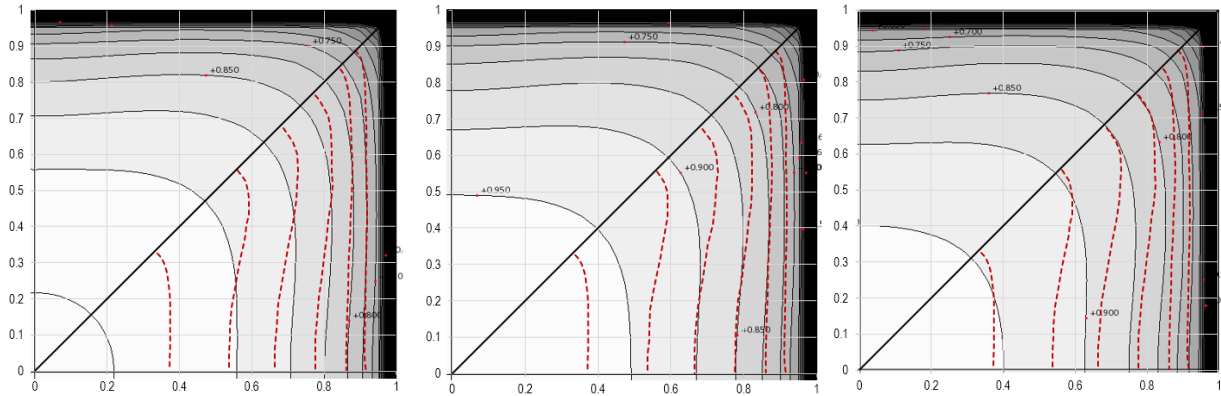


Figure 5.14. Constant-velocity contours for near-wall mesh size of $y^+ > 30$ compared to the experimental data, for the KW-QCR turbulence model scaled by (left) the lowest center velocity, (center) the average center velocity, and (right) the highest center velocity. Experiment - red dashed lines, CFD - black solid lines.

Similar data were gathered for the center temperatures and are presented in Table 5.4. The estimation of the center temperature in the experiment is even more difficult than the center velocity. In the references, the temperature is only provided in the form of the isolines or normalized T^+ plots. This information is not sufficient to calculate the temperature in the center of the duct in the experiment. The highest computationally estimated center temperature was 31.35 °C (304.5 K), and the lowest was 25.65 °C (298.8 K), for the KW-CUBIC and RST-LPS2L turbulence models, respectively. The average center temperature was calculated to be 27.75 °C \pm 2.74 °C (300.9 K \pm 2.74 K).

Figure 5.15 presents constant-temperature contours compared to the experimental data for the KW-QCR turbulence model, scaled (per Eq. (4)) by the lowest center temperature of 25.1 °C (298.16 K), average center temperature of 27.75 °C (300.9 K), and the center temperature predicted by the KW-QCR turbulence model, 31.35 °C (304.5 K). Again, very high sensitivity of the isolines can be noticed for that temperature range.

Table 5.4. Comparison of the center temperature in the simulations from models with wall $y^+ > 30$ and various turbulence models.

Source	Center temperature, °C (K)
SKE-CUBIC	29.8 (303.0)
RKE	26.2 (299.4)
KW-QCR	31.0 (304.1)
KW-CUBIC	31.4 (304.5)
RST-EB	23.6 (296.8)
RST-QPS	26.6 (299.7)
RST-LPS2L	25.6 (298.8)
computational average	27.75 (300.9) \pm 2.74

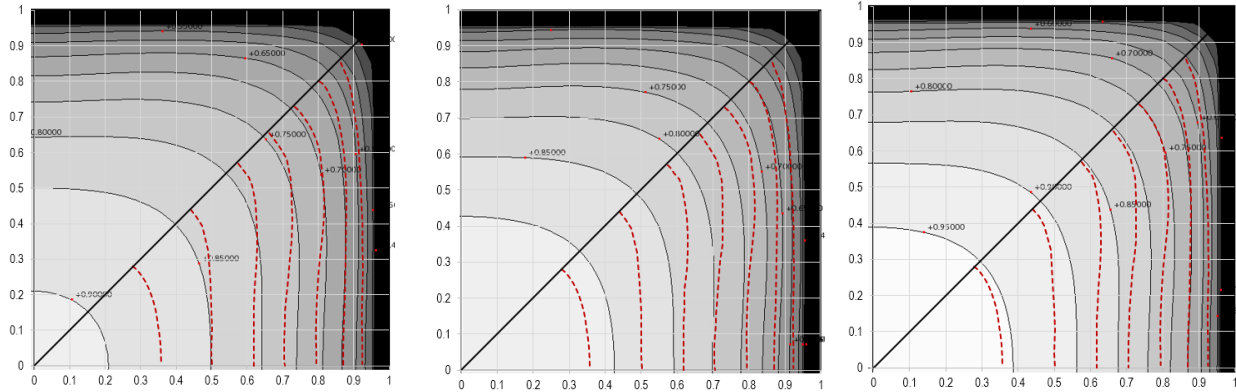


Figure 5.15. Constant-temperature contours for near-wall mesh size of $y^+ > 30$ compared to the experimental data, for the KW-QCR turbulence model scaled by (left) the lowest center temperature, (center) the average center temperature, and (right) the highest center temperature. Experiment - red dashed lines, CFD - black solid lines.

Despite the difficulties with the scaling of the isolines and the lack of raw data, the experiment conducted by Hirota et al. [29] may still be considered a valuable benchmark case. Its value lies in the data that were reported closer to the walls of the duct, in the form of plots presenting U^+ and T^+ as functions of y^+ . The experimental isolines of the velocities and temperatures were reported only relatively far away from the walls.

Figure 5.16 shows the velocity isolines (blue dashed lines and a green solid line) overlaid on the grid (red lines) used in the model with wall $y^+ > 30$ and KW-QCR turbulence. The centroid of the first cell is located at $y^+ \approx 36$. The centroid of the second cell is located at $y^+ \approx 105$, and the third one is at $y^+ \approx 175$. The first isoline (marked with a green solid line in the figure) is located between the centroids of the second and the third cell at around $y^+ \approx 150$. Thus, information related to y^+ values closer to the wall cannot be differentiated. For this reason, results shown in the subsequent plots may be of greater value, as they allow for qualitative as well as quantitative comparison of the simulated results versus the experimental data for y^+ in the range between 12 and 1,400.

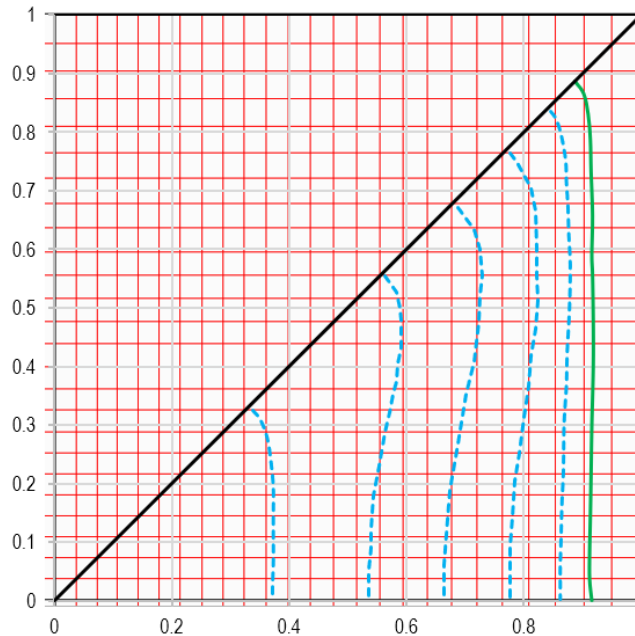


Figure 5.16. Computational grid with $y^+ > 30$ overlaid with the digitized experimental velocity isolines [29].

Figure 5.17 through Figure 5.23 present the simulated velocities against the experimental data scaled to the wall parameters, U^+ vs. y^+ . That scaling was explained earlier in the current chapter. Each figure contains three plots (if possible) obtained for three different grids with near-wall cell size $y^+ < 1$, $y^+ < 5$, and $y^+ > 30$. Each plot contains the standard wall functions used by STAR-CCM+ in the viscous sublayer and in the log-law layer, plotted with dashed green and red lines, respectively. The wall functions are independent of the turbulence models, and for the coarser meshes they become the boundary condition for the turbulent-flow solution within the duct away from the walls. The finest mesh, with $y^+ < 1$, does not use wall functions to predict the velocity of the fluid near the walls, as the mesh resolution allows for calculation of that profile explicitly. Thus, looking at the three plots for each turbulence model allows for an independent assessment of the turbulence models' performance as well as the performance of the wall functions in conjunction with these turbulence models for the coarser meshes.

It must be noted that it is not clear what values of the material properties were assumed by Hirota et al. in the calculations of these scaled parameters, or how the y^+ was calculated. Thus, some of the discrepancies in the results may be again caused by the lack of raw data. Also, for the simulated results the parameters y^+ , U^+ , and T^+ were manually defined in STAR-CCM+. The definitions of these parameters rely on calculations of U^* , the friction velocity. The value of U^* is available directly in STAR-CCM+ but its use led to large discrepancies between the numerical and the experimental results. Defining U^* manually as $U^* = \sqrt{\tau_w/\rho}$ (where τ_w is the local wall shear stress and ρ is the density) was recommended by the STAR-CCM+ developers and led to predictions much closer to the experimental data.

Figure 5.17 contains the U^+ plots as a function of y^+ for the RKE turbulence model. The U^+ is overpredicted by the model with the coarsest mesh near the wall ($y^+ > 30$). Results obtained with the finer-mesh models follow the wall functions with a noticeable blending between the two of them in the buffer layer for $5 < y^+ < 30$. In the log-law region, for $30 < y^+ < 300$, there is good agreement

between the simulated and the experimental data. For $y^+ > 300$, the simulated data only roughly follow the experimental data. The portion of the duct cross section with $y^+ > 300$ occupies most of the center portion of the duct. This is the area where the simulated isolines were not in good agreement with the experimental isolines.

Figure 5.18 contains the U^+ plots as a function of y^+ for the SKE-CUBIC turbulence model. Again, an overestimation of U^+ is visible over the entire range of y^+ for the coarse grid with $y^+ > 30$ near the wall.

Figure 5.19 contains the U^+ plots as a function of y^+ for the KW-QCR turbulence model. This turbulence model tends to slightly overpredict the U^+ for $y^+ > 30$ for all the cell sizes.

Figure 5.20 presents the U^+ plots as a function of y^+ for the KW-CUBIC turbulence model. Although it was very effective in predicting the distorted shapes of the isolines, this turbulence model was the worst-performing one in the current comparison, especially for the finer grids with $y^+ < 5$. It should be used with great caution.

Figure 5.21 presents the U^+ plots as a function of y^+ for the RST-LPS2L turbulence model. This model performed well for the finer grids, with $y^+ < 5$ predicting U^+ values close to the experimental data and the wall functions used by STAR-CCM+. However, it significantly overpredicted the experimental data when a coarser grid was used, with a near-wall mesh size of $y^+ > 30$.

Figure 5.22 presents the U^+ plots as a function of y^+ for the RST-EB turbulence model. For the region close to the wall, $y^+ < 300$, this model performed reasonably well for all three types of grids. It tended to slightly overestimate the U^+ in the central portion of the duct for $y^+ > 300$. While in the previous simulations of isothermal benchmark cases, this turbulence model gave the best results, it will be shown for the T^+ results that this model should be used with caution for the coarser grids with $y^+ > 30$, and the RST-QPS turbulence model gave better results.

Figure 5.23 presents the U^+ plots as a function of y^+ for the RST-QPS turbulence model. RST-QPS and RST-EB are based on the most recent formulations of RS turbulence models [33]. The RST-QPS model is only available for coarse grids with near-wall cell size of $y^+ > 30$, meaning it does not resolve the viscous near-wall region. This model marginally overpredicted the experimental data.

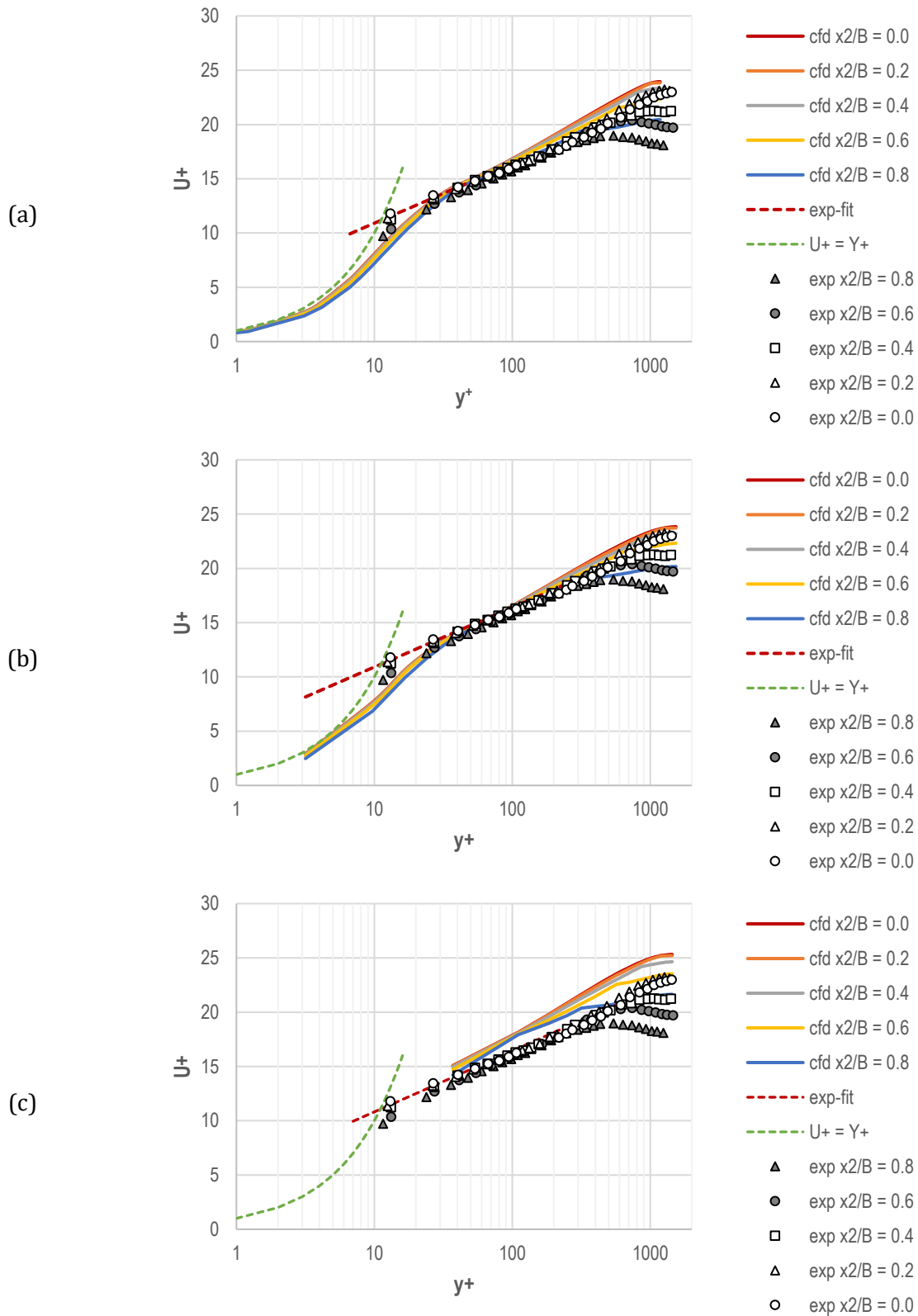


Figure 5.17. U^+ in simulations with the RKE turbulence model and near-wall cell size (a) $y^+ < 1$, (b) $y^+ < 5$, and (c) $y^+ > 30$, as compared to the experimental data.

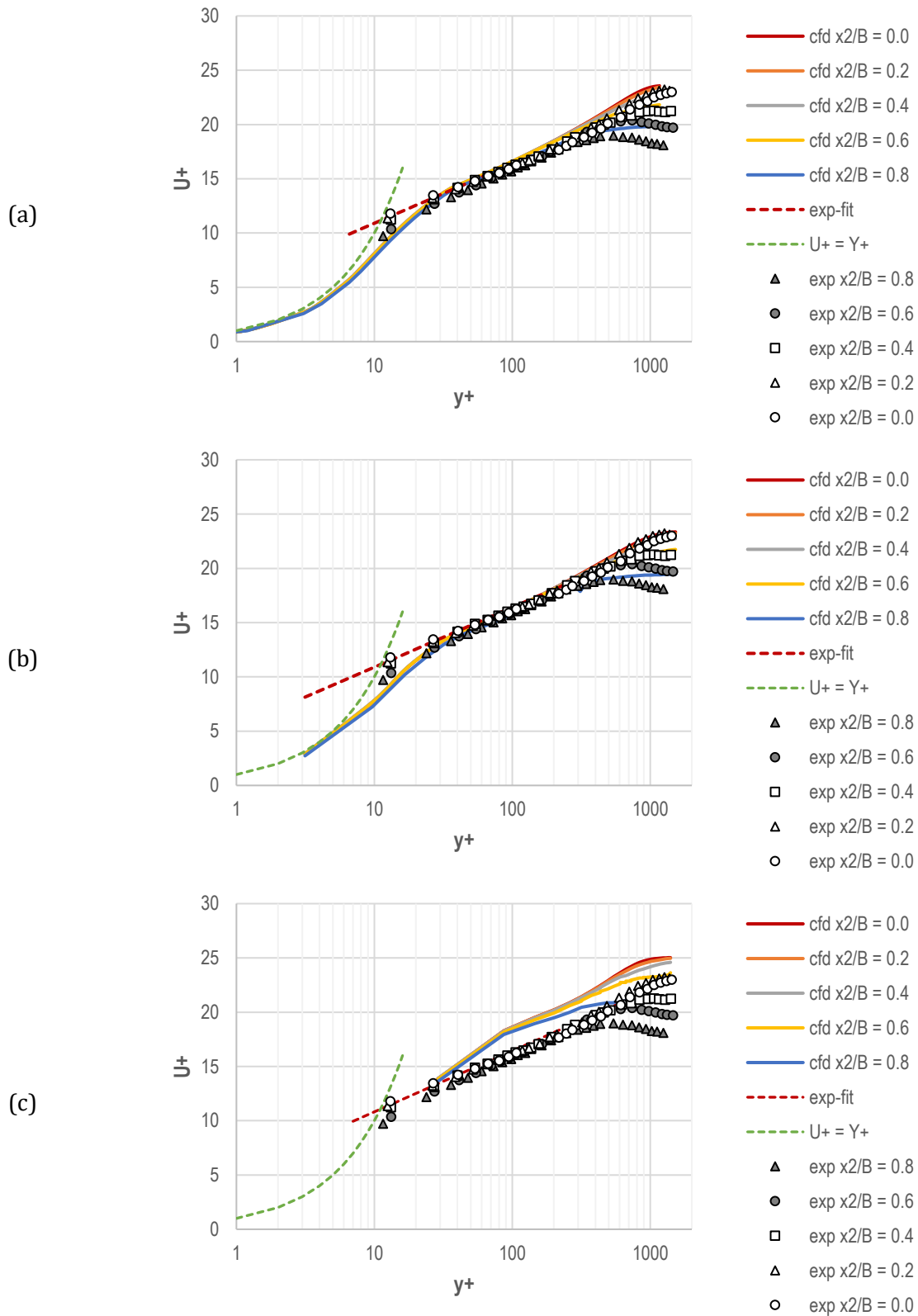


Figure 5.18. U^+ in simulations with the SKE-CUBIC turbulence model and near-wall cell size (a) $y^+ < 1$, (b) $y^+ < 5$, and (c) $y^+ > 30$, as compared to the experimental data.

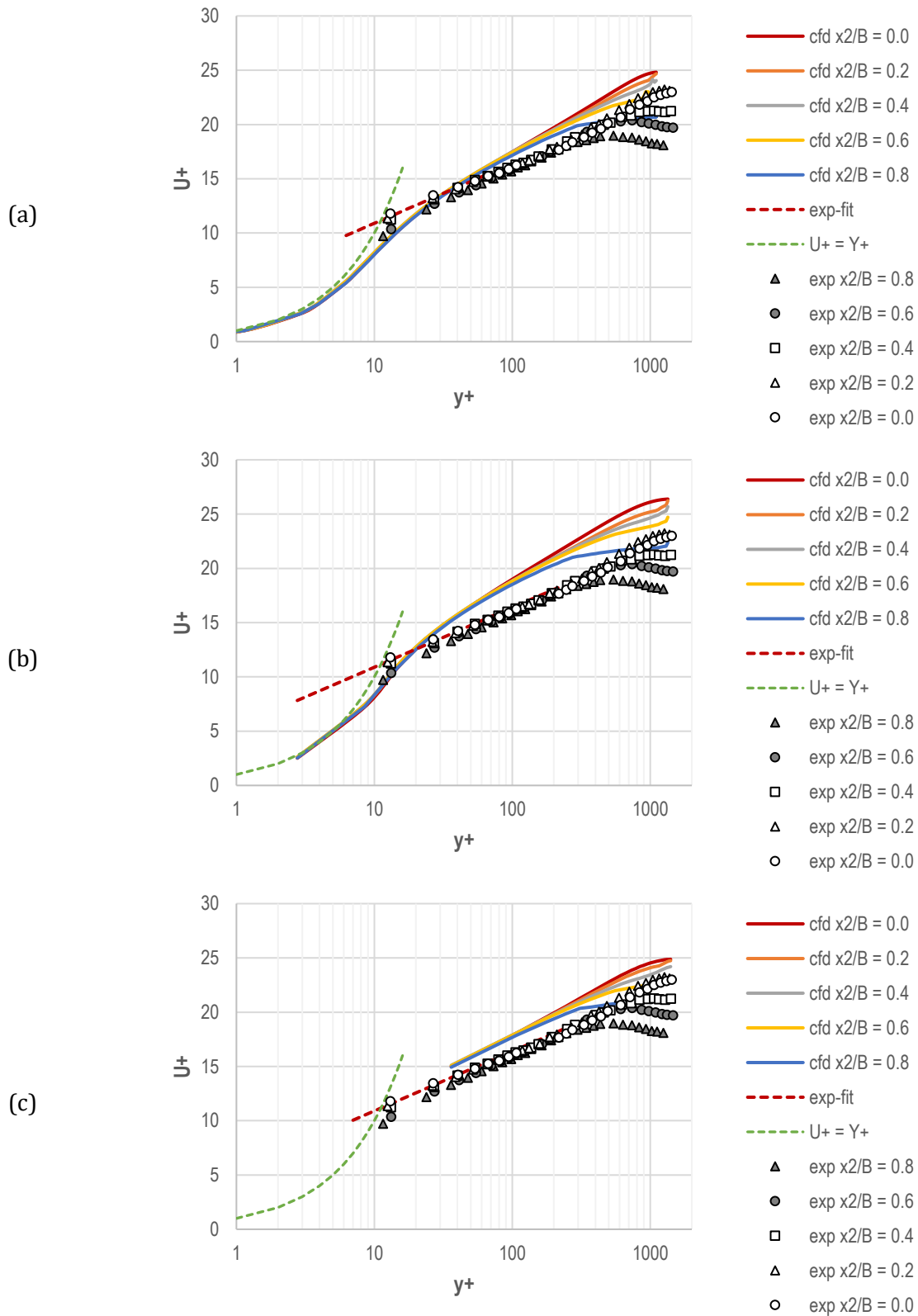


Figure 5.19. U^+ in simulations with the KW-QCR turbulence model and near-wall cell size (a) $y^+ < 1$, (b) $y^+ < 5$, and (c) $y^+ > 30$, as compared to the experimental data.

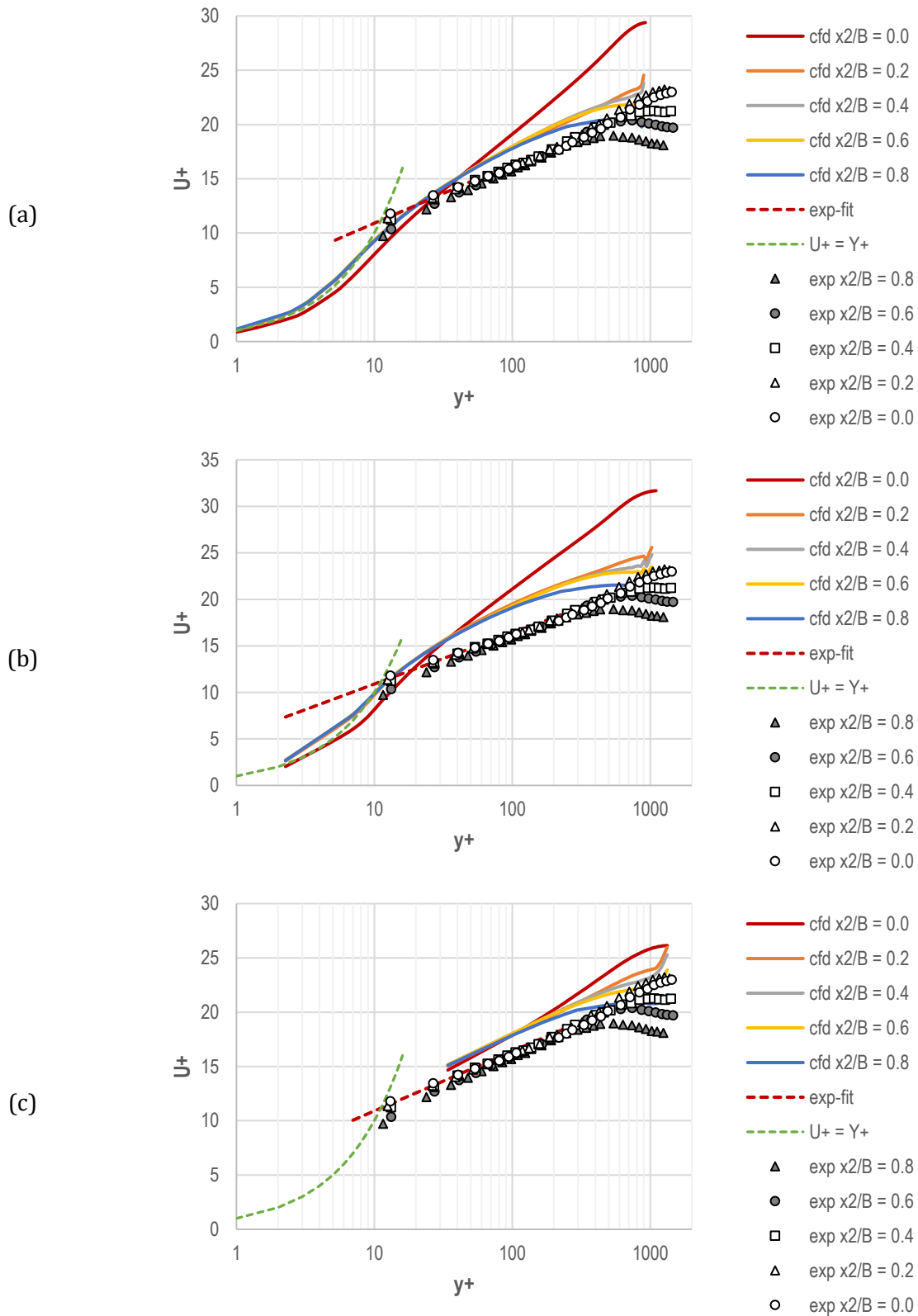


Figure 5.20. U^+ in simulations with the KW-CUBIC turbulence model and near-wall cell size (a) $y^+ < 1$, (b) $y^+ < 5$, and (c) $y^+ > 30$, as compared to the experimental data.

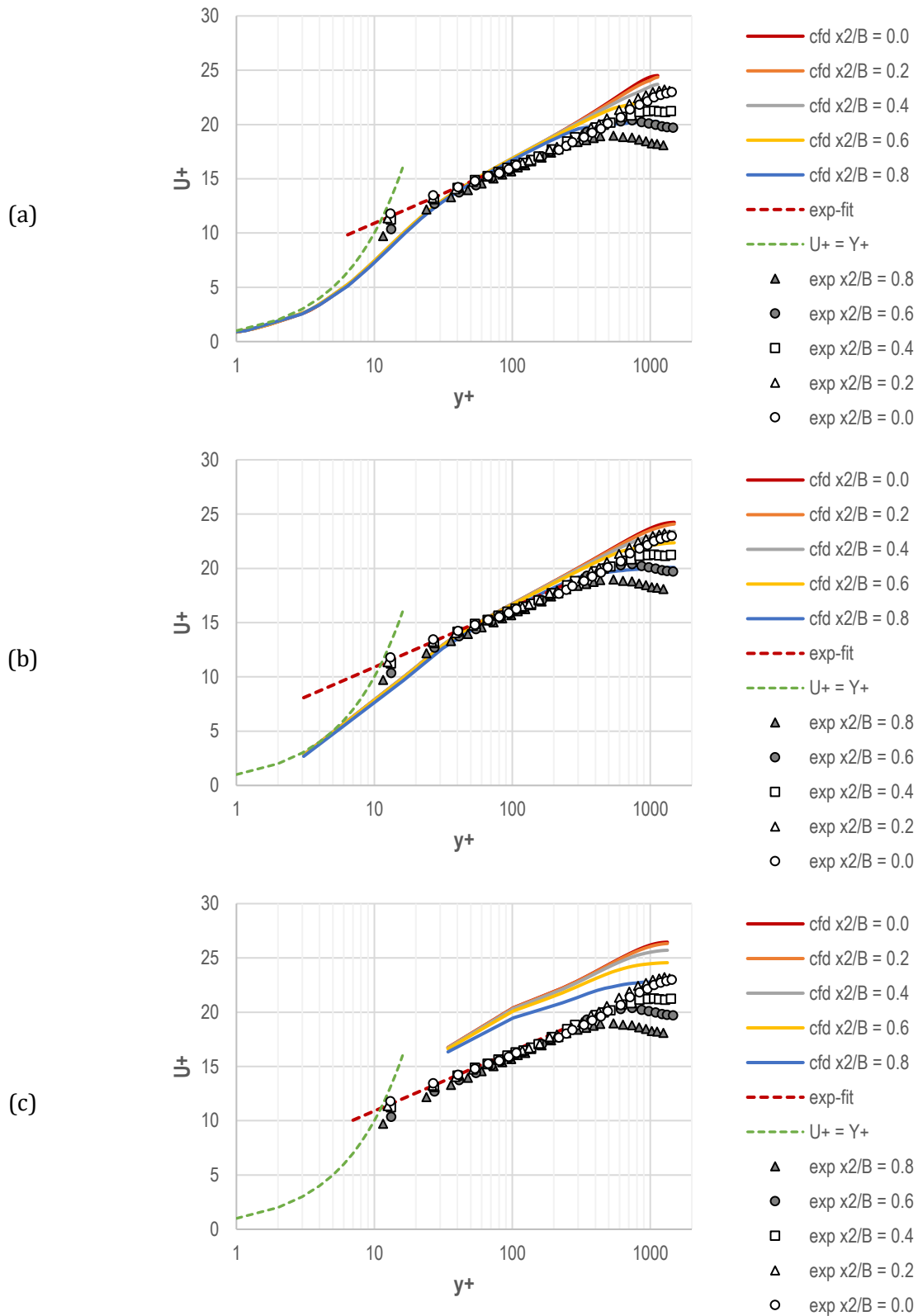


Figure 5.21. U^+ in simulations with the RST-LPS2L turbulence model and near-wall cell size (a) $y^+ < 1$, (b) $y^+ < 5$, and (c) $y^+ > 30$, as compared to the experimental data.

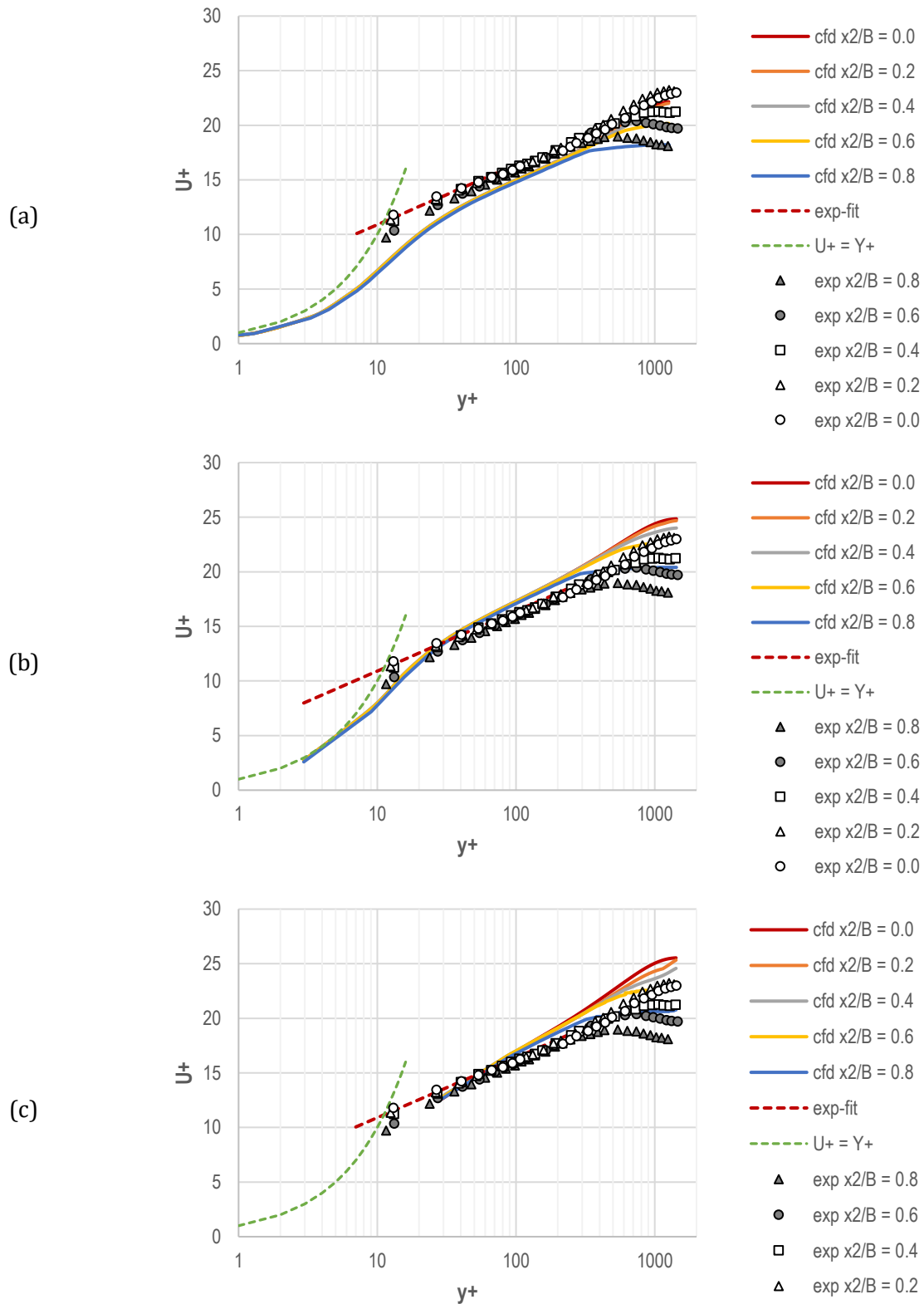


Figure 5.22. U^+ in simulations with the RST-EB turbulence model and near-wall cell size (a) $y^+ < 1$, (b) $y^+ < 5$, and (c) $y^+ > 30$, as compared to the experimental data.

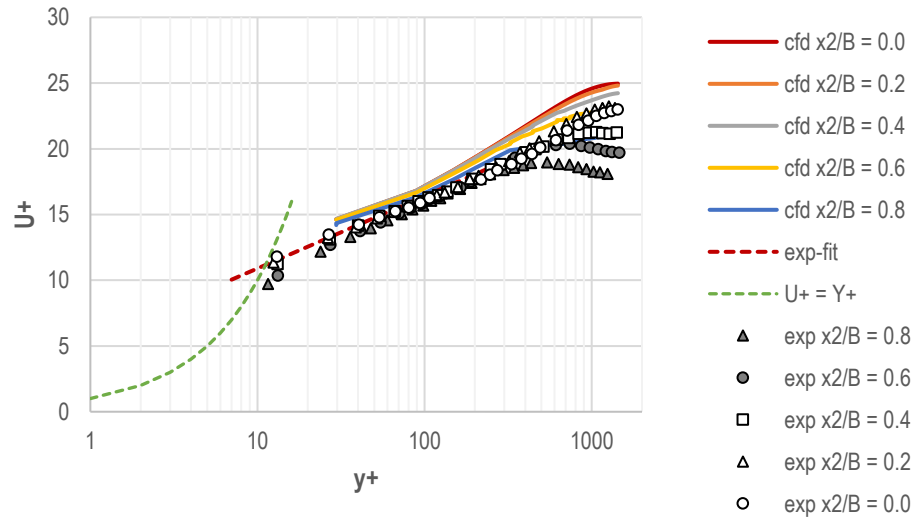


Figure 5.23. U^+ in simulations with the RST-QPS turbulence model and near-wall cell size $y^+ > 30$, as compared to the experimental data.

Figure 5.24 presents the T^+ plots as a function of y^+ for the RKE turbulence model. Good agreement with the experimental data was obtained for higher values of y^+ , namely, above 40. It must be noted that the experimental data follows the logarithmic fit (straight red dashed line in the plot) down to $y^+ \approx 12$, while the simulated results follow the blending function implemented in the code between the linear and the logarithmic functions in the range $5 < y^+ < 30$. This behavior is common to all tested turbulence models.

Figure 5.25 presents the T^+ plots as a function of y^+ for the SKE-CUBIC model. The performance of that model is good and is very similar to the performance of the RKE model. It should be noted that the SKE-CUBIC model was much better in predicting the shape of the isolines in the duct than the linear RKE model. This finding may lead to the conclusion that the prediction of the temperature near the wall, when reported in wall parameters, is independent of the turbulence model in the center of the duct.

Figure 5.26 presents the T^+ plots as a function of y^+ for the quadratic turbulence model KW-QCR. This model was superior in predicting the isolines for the isothermal experiments and the isolines of temperature in the current case. The T^+ plots presented in this figure look very similar to the plots described above for the RKE and SKE-CUBIC turbulence models.

Figure 5.27 presents the T^+ plots as a function of y^+ for the quadratic turbulence model KW-CUBIC. The simulated results close to the wall follow the linear relationship between T^+ and y^+ up until $y^+ \approx 10$, in contrast to the previous turbulence models, which deviated from it at $y^+ \approx 5$. However, the model with the finer near-wall grid greatly overestimated the T^+ when the non-dimensional distance from the wall y^+ was greater than 50. As previously indicated, this model also greatly overpredicted the U^+ values, and for that reason should be used with great caution.

Figure 5.28 presents the T^+ plots as a function of y^+ for the RST-LPS2L turbulence model. The numerical results predict the experimental data reasonably well. However, for finer grids, T^+ is underpredicted.

Figure 5.29 presents the T^+ plots as a function of y^+ for the RST-EB turbulence model. As seen with the U^+ predictions, it performed well for the finer grids but greatly overpredicted the T^+ values for the coarse grid. On the other hand, the high- y^+ RST-QPS model, for which the results are presented in Figure 5.30, performed significantly better for the coarse grid.

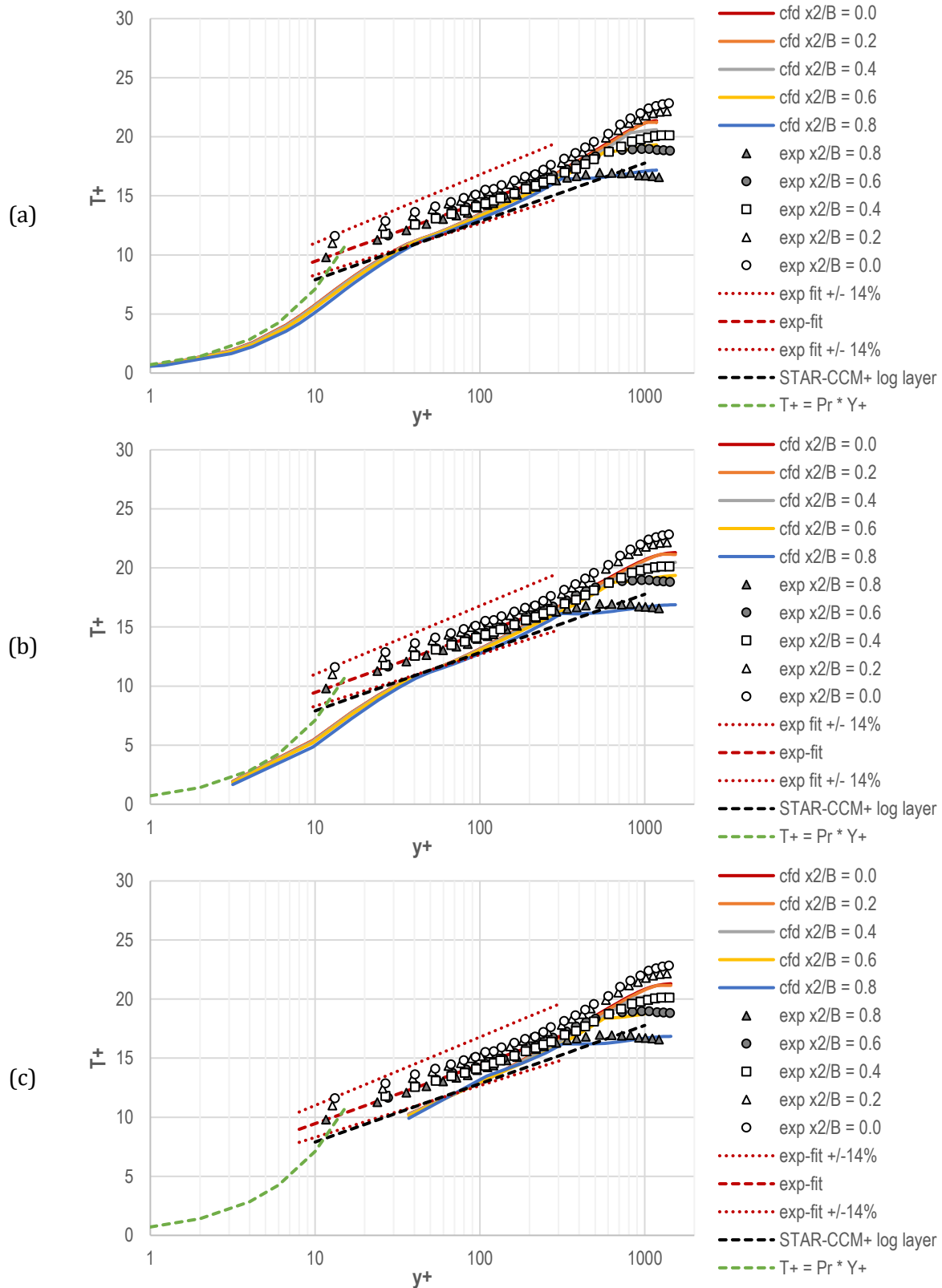


Figure 5.24. T^+ in simulations with the RKE turbulence model and near-wall cell size (a) $y^+ < 1$, (b) $y^+ < 5$, and (c) $y^+ > 30$, as compared to the experimental data.

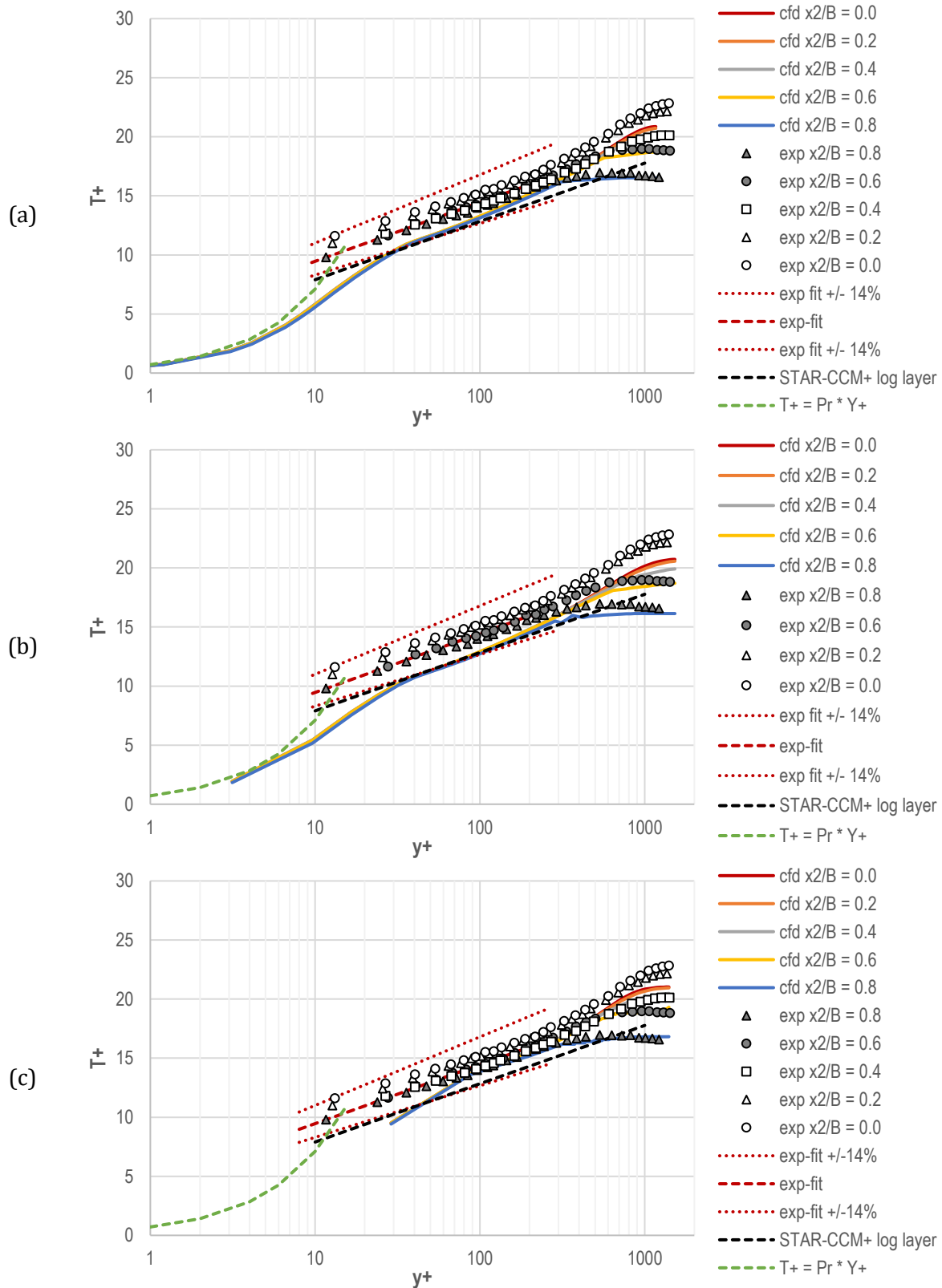


Figure 5.25. T^+ in simulations with the SKE-CUBIC turbulence model and near-wall cell size (a) $y^+ < 1$, (b) $y^+ < 5$, and (c) $y^+ > 30$, as compared to the experimental data.

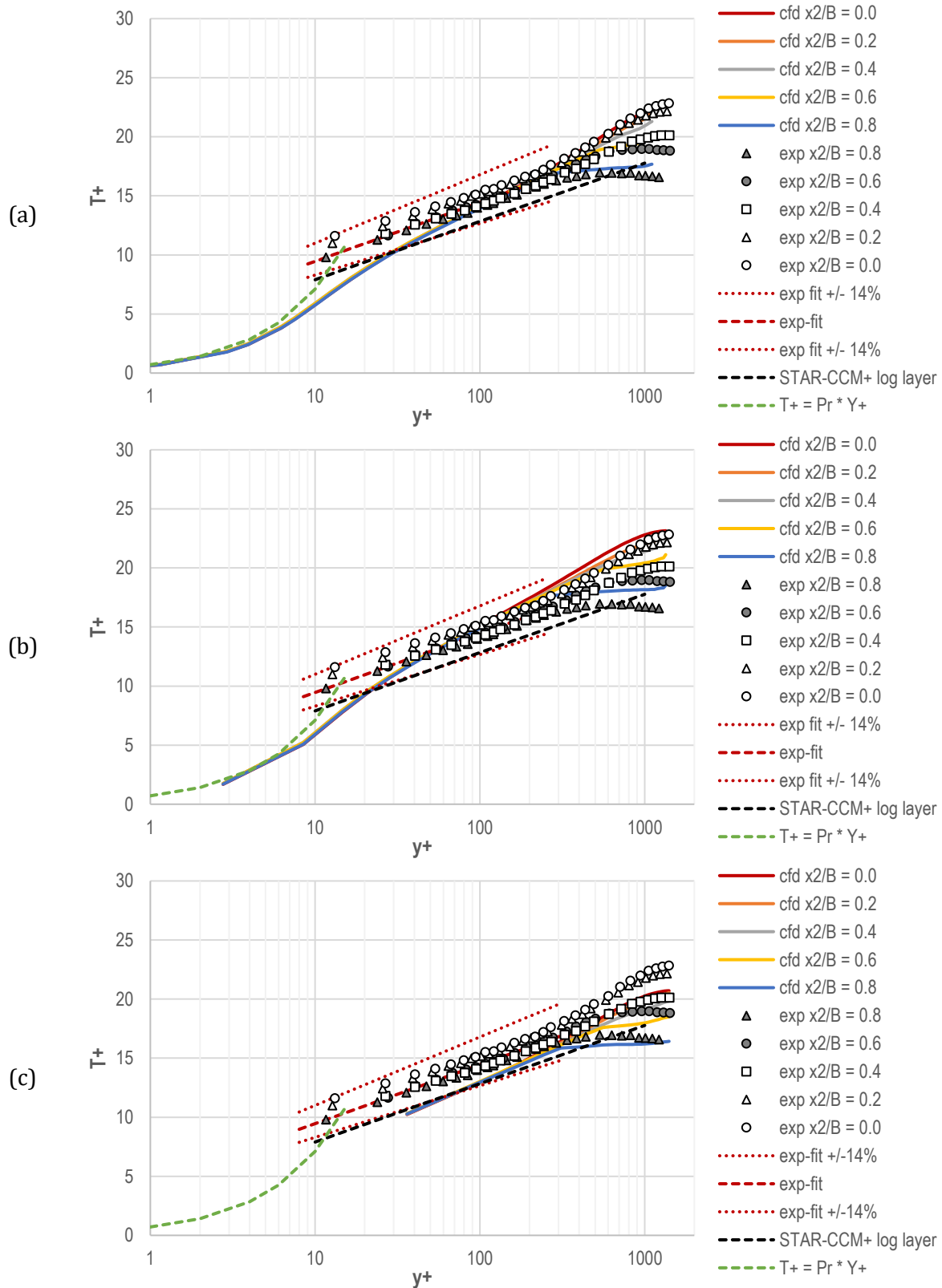


Figure 5.26. T^+ in simulations with the KW-QCR turbulence model and near-wall cell size (a) $y^+ < 1$, (b) $y^+ < 5$, and (c) $y^+ > 30$, as compared to the experimental data.

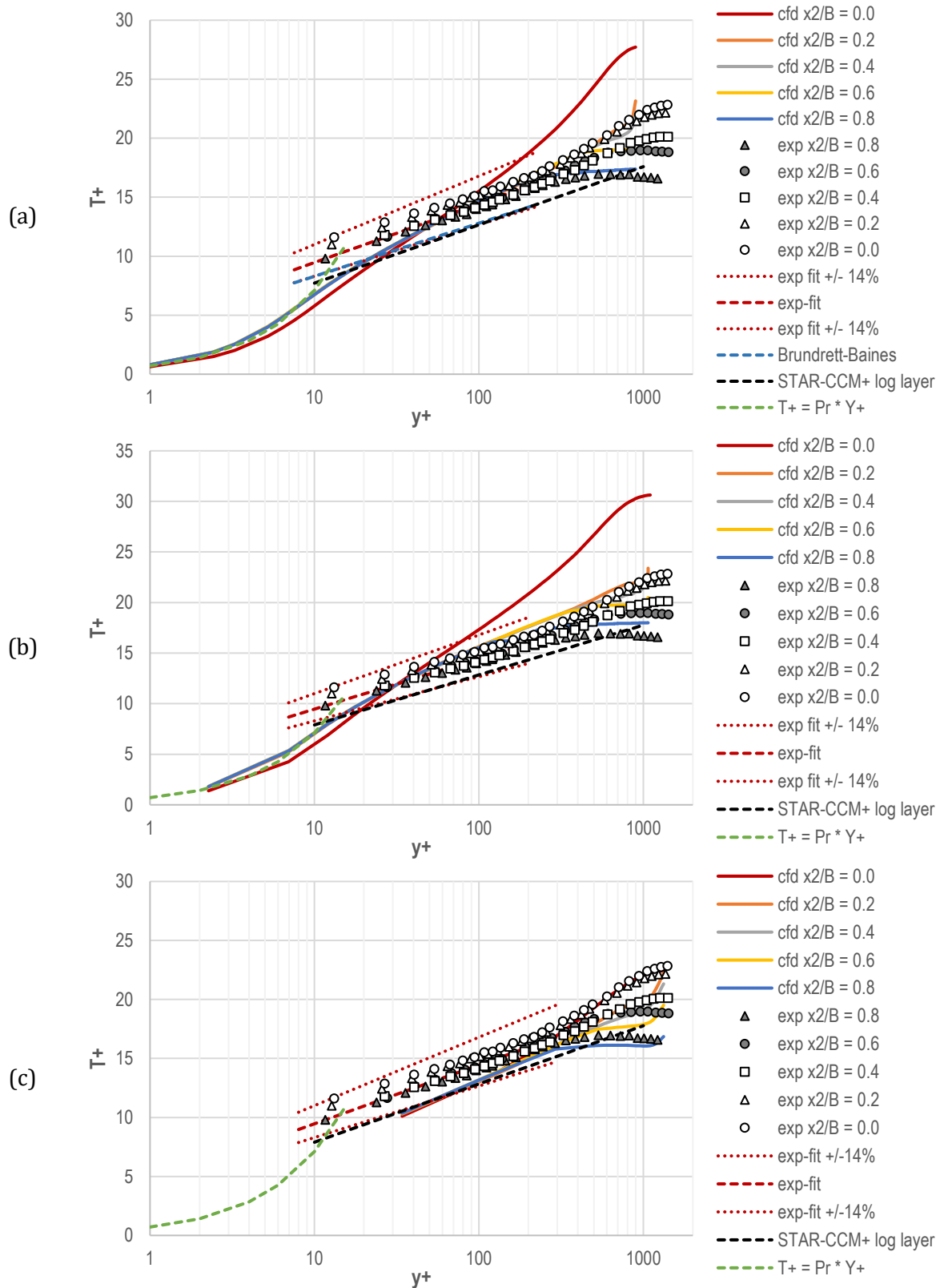


Figure 5.27. T^+ in simulations with the KW-CUBIC turbulence model and near-wall cell size (a) $y^+ < 1$, (b) $y^+ < 5$, and (c) $y^+ > 30$, as compared to the experimental data.

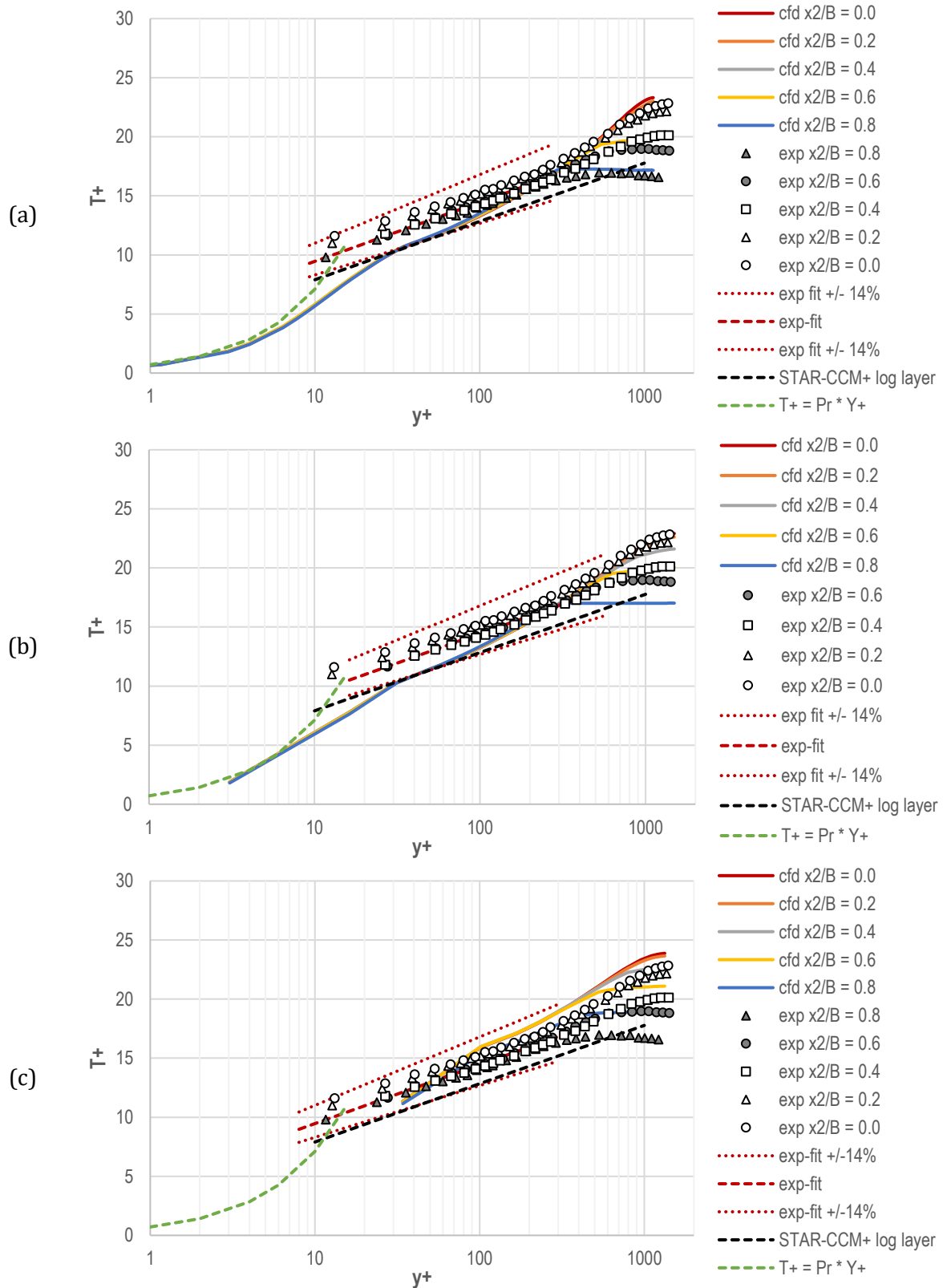


Figure 5.28. T^+ in simulations with the RST-LPS2L turbulence model and near-wall cell size (a) $y^+ < 1$, (b) $y^+ < 5$, and (c) $y^+ > 30$, as compared to the experimental data.

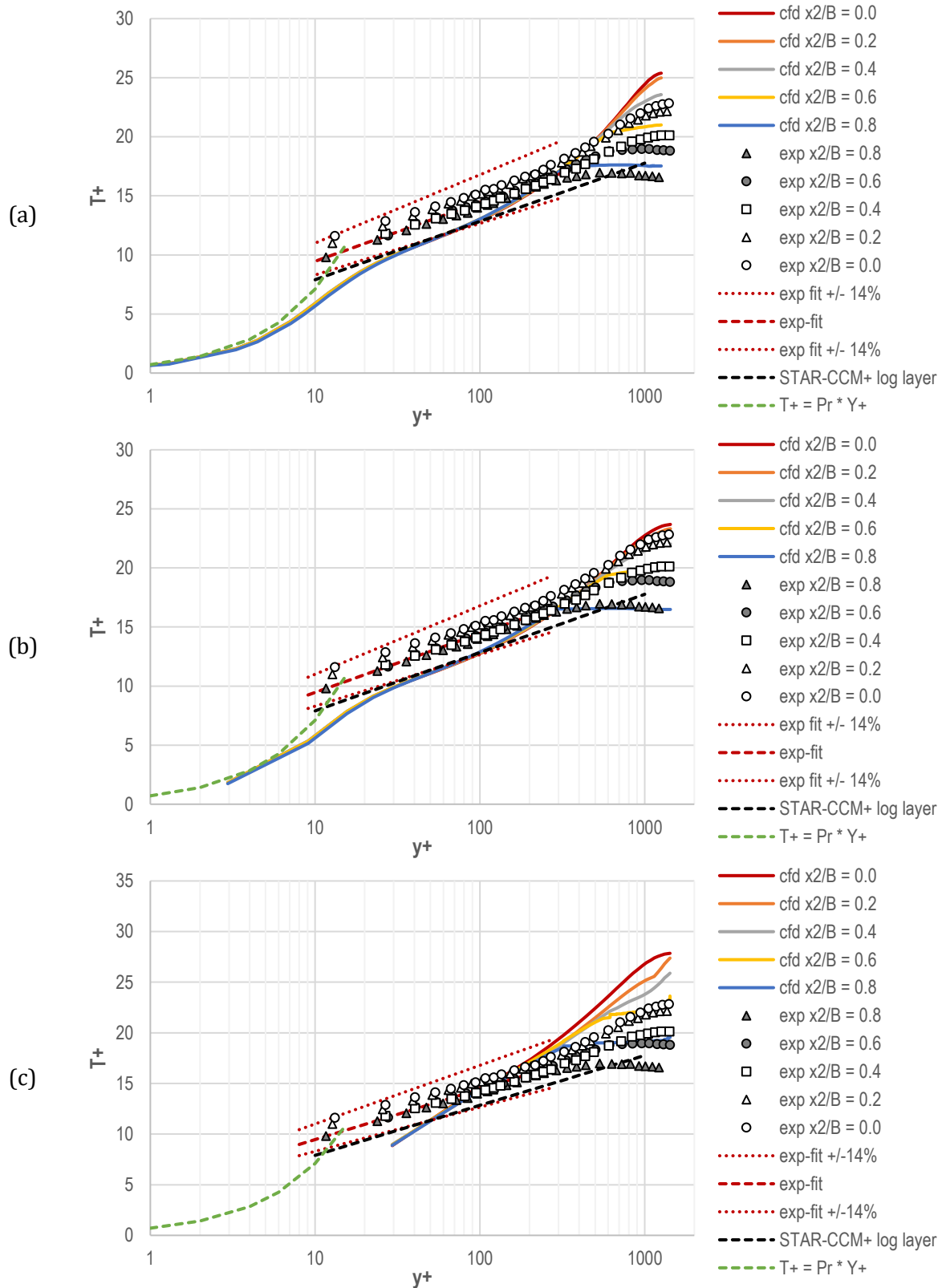


Figure 5.29. T^+ in simulations with the RST-EB turbulence model and near-wall cell size (a) $y^+ < 1$, (b) $y^+ < 5$, and (c) $y^+ > 30$, as compared to the experimental data.

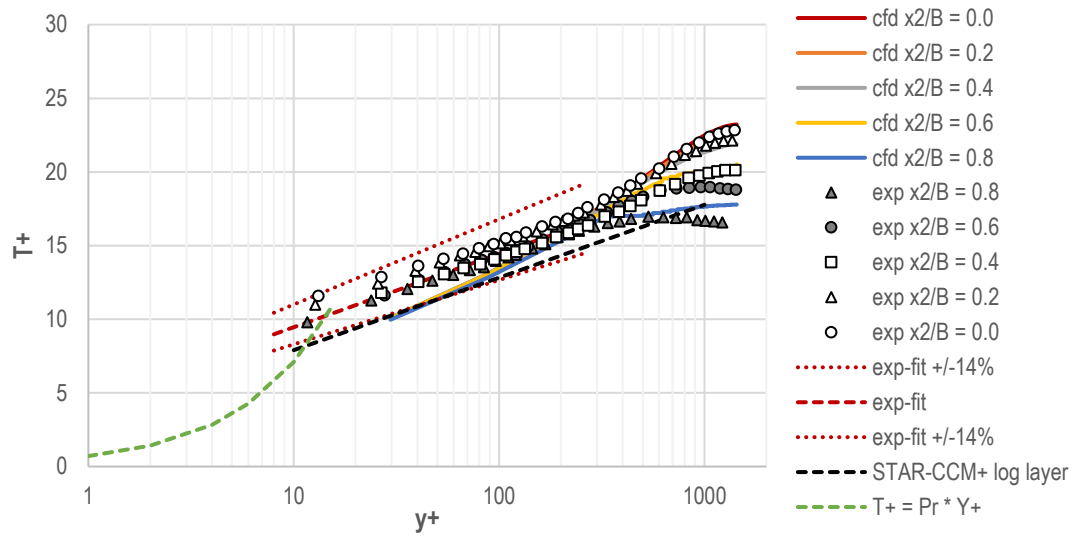


Figure 5.30. T^+ in simulations with the RST-QPS turbulence model and near-wall cell size $y^+ > 30$, as compared to the experimental data.

6 Conclusions

The study presented in this report focuses on testing and validating the turbulence models for simulating the coolant flow in the corners of the coolant channels. For that purpose, initially, several RANS turbulence models implemented in the commercial code STAR-CCM+ were used in a generic single-plate model to compare their influence on the heat transfer and temperature distribution near the edges of the coolant channels. Shape of the power distribution, which is representative of involute reactors, with power peaking near the edges, was used as an input to these simulations. The power peaking locations are usually also the locations of the minimum safety margins for involute-plate reactors. The fuel core has been positioned at a varying distance of $\sim 0.15 D_h$ to $\sim 3.0 D_h$ from the side plate forming a power peak at corresponding distances from the side plate.

Out of the tested turbulence models, for all the fuel core positions, the RST-EB model predicted the highest temperature at the cladding-coolant interface, followed by RKE, while KW-QCR predicted the lowest value. The difference between predictions obtained with the KW-QCR and RST-EB models was about 5 °C. This is not a negligible difference, and for that reason, the use of CFD models for safety analysis should not be limited to a single turbulence model. The recommendation is to test several of them (as a minimum RKE and KW-QCR as the two most robust ones, together with RS model which is the most complex one of them) and report the range in the predictions as an uncertainty of the numerical simulations.

RST-EB's prediction of the most conservative cladding temperatures is consistent with conclusions of past simulations. The quadratic KW model (KW-QCR) predicted the lowest temperatures despite being able to capture the turbulence anisotropy, unlike the linear turbulence models. The predicted results remained consistent as the size of the unfueled region was decreased. Regardless of the ability of the models to capture the secondary flows, all trends in predictions of heat fluxes and temperatures on the cladding-coolant interface looked alike.

It was shown that the relative distance between the fuel edge and the side plate has no influence on the peak temperature in the cladding, as long as that distance is larger than two D_h . The closer the edge of the fuel gets to the side plate, the higher the predicted peak temperature on the cladding-coolant interface. This behavior was confirmed with the use of three tested turbulence models: RKE, KW-QCR, and RST-EB. RKE, which is an isotropic eddy viscosity model, is not capable of predicting the anisotropic flow patterns in the corners. Thus, the effect presented here appears not to be exacerbated by the anisotropy of the flow in the corners.

To better understand the ability of various turbulence models to capture the flow patterns in that section of the coolant channel ($2D_h$ and closer to the edge), validation of these models against the selected experimental benchmarks was performed. Several experiments measuring the flow parameters in square and rectangular ducts were reviewed as benchmark candidates. It was found that the historical journal articles and reports frequently lack the raw data needed as input for equivalent numerical simulations. Thus, many landmark experiments had to be rejected as candidates for software validation benchmarks. This was especially true for the heated experiments.

Ultimately, three experiments were selected for benchmarking:

1. Launder and Ying's isothermal experiment with air,
2. Melling and Whitelaw's isothermal experiment with water, and
3. Hirota et al.'s heated experiment, with air heated via constant wall temperature.

The simulations aimed at replicating the experimentally obtained velocity profiles that in square ducts are known to be affected by secondary flows. Up to seven turbulence models have been tested for each of these experiments with four common among all of them, including: RKE, KW-QCR, RST-EB, and RST-LPS2L models. Although all tested turbulence models gave relatively good results in the simulations of the isothermal experiments, the linear eddy viscosity turbulence models (RKE, and KW) were found to be less accurate, as they inherently describe turbulence in an isotropic fashion and are not able to capture some of the turbulence effects, like the mean flow distortions in the corners that are induced by secondary flows. KW-QCR, with quadratic terms, performed significantly better than the above-mentioned linear models, but the best match between the simulated and experimental data was obtained with the RST-EB turbulence model.

Although all models struggled with replicating the isolines of velocity and temperature in the simulations of the heated experiment, it was concluded that this issue could have been caused by the normalizing method of the data used in the original papers and lack of access to the raw data from the experiments. Some of the simulation setup parameters were not listed in the original references and had to be assumed based on limited data and empirical correlation.

Scaling of the results to the wall parameters y^+ , U^+ , and T^+ provides non-dimensional data, that, by definition, should be insensitive to small differences between the assumed input to the simulations and the actual experiment setup. The definitions of these parameters rely on calculations of U^* , the friction velocity. The value of U^* is available directly in STAR-CCM+ but its use led to large discrepancies between the numerical and the experimental results. Defining U^* manually as $U^* = \sqrt{\tau_w / \rho}$ (where τ_w is the local wall shear stress and ρ is the density) was recommended by the STAR-CCM+ developers and led to predictions much closer to the experimental measurements by the authors of the historical journal articles.

Simulations of the heated experiment with the use of almost all turbulence models were able to replicate the non-dimensional U^+ and T^+ experimental measurements, including RKE (despite its inability to capture anisotropic effects of turbulence). A notable outlier was the KW-CUBIC model, which vastly overpredicted both quantities. These simulations also revealed some deficiencies of the RST-EB turbulence model, which had previously given superior matches with the experimental data from unheated experiments. For coarser grids, this model significantly overpredicted the T^+ values. The performance of RST-QPS model for this case was also tested and the model provided closer match to the experimental data. However, RST-QPS model cannot be used universally for all near wall mesh sizes as it has only been implemented in STAR-CCM+ for high- y^+ wall treatment (that is using wall functions) without resolving the viscous-affected near-wall region.

Table 6.1 attempts to summarize the performance of the used turbulence models for three simulated experiments. Qualitative grades have been assigned to each model for each of the experiments. The following grades have been used:

- “Very good performance” - when all compared results presented a close match with the experimental data for all meshes.
- “Good performance” - when some of the compared results matched the experimental data for all or two out of three meshes.
- “Not able to predict” - when the simulated results did not capture the character of the analyzed field, or the quantitative prediction was significantly different from the experimental data.

Table 6.1. Summary of turbulence models used in simulations of each experiment and their qualitative performance

Turbulence model	Simulations of the Experiment of Launder and Ying's	Simulations of the Experiment of Melling and Whitelaw's	Simulations of the Experiment of Hirota et al.
RKE	Not able to predict velocity profiles	Not able to predict velocity profiles	Good performance
SKE-CUBIC	Not used	Not used	Good performance
KW	Not able to predict the velocity profiles	Not able to predict the velocity profiles	Not used
KW-QCR	Good performance	Very good performance	Good performance
KW-CUBIC	Not used	Not used	Not able to predict the U+ and T+ profiles
RST-EB	Very good performance	Very good performance	Good performance for denser meshes; Not able to predict T+ profiles for coarse meshes
RST-QPS	Not used	Not used	Good performance within applicability range (coarse meshes)
RST-LPS2L	Very good performance	Good performance	Good performance

Overall, it can be stated that KW-QCR was the most universally applicable turbulence model, giving good predictions of the isolines as well as velocity and temperature profiles in all three benchmarks. For the instances of non-heated experiments, the RST-EB model provided the best match between the simulated and the experimental data. In the previous work [4], it provided consistently conservative results for wide ranges of Reynolds number in heated simulations. However, because of the inconsistencies in the predicted results for the Hirota et al. heated experiment, it should be used with caution.

Acknowledgment

This work was sponsored by the U.S. Department of Energy, Office of Material Management and Minimization in the U.S. National Nuclear Security Administration Office of Defense Nuclear Nonproliferation under Contract DE-AC02-06CH11357.

References

- [1] Oak Ridge National Laboratory, "High Flux Isotope Reactor," [Online]. Available: <https://neutrons.ornl.gov/hfir>. [Accessed 23 07 2018].
- [2] Institut Laue-Langevin, "The ILL High-Flux reactor," [Online]. Available: <https://www.ill.eu/reactor-and-safety/high-flux-reactor/>. [Accessed 23 07 2018].
- [3] Technical University of Munich, "Research Neutron Source Heinz Maier-Leibnitz (FRM II)," [Online]. Available: <https://www.frm2.tum.de/en/home/>. [Accessed 23 07 2018].
- [4] C. Bojanowski, A. Bergeron and J. Licht, "Involute Working Group - Validation of CFD Turbulence Models for Steady-State Safety Analysis," ANL/RTR/TM-19/5, Argonne National Laboratory, Lemont, IL, USA, 2020.
- [5] W. Gambill and R. Bundy, "HFIR Heat-Transfer Studies of Turbulent Water Flow in Thin Rectangular Channels," Oak Ridge National Laboratory, Oak Ridge, TN, 1961.
- [6] F. Incropera and D. DeWitt, Fundamentals of Heat and Mass Transfer, 4th Edition, New York: Wiley, 1996.
- [7] E. Sieder and G. Tate, "Heat Transfer and Pressure Drop of Liquids in Tubes," *Ind. Eng. Chem.*, vol. 28, no. N 12, pp. 1429-1435, 1936.
- [8] A. Bergeron, "Review of the Oak Ridge National Laboratory (ORNL) Neutronic Calculations Regarding the Conversion of the High Flux Isotope Reactor (HFIR) to the Use of Low Enriched Uranium (LEU) Fuel," ANL/RERTR/TM-12/49, Argonne National Laboratory, Lemont, 2012.
- [9] A. Bergeron, "Neutronic Conversion Analyses of the Laue-Langevin Institute (ILL) High Flux Reactor (RHF)," ANL/GTRI/TM-14/15, Argonne National Laboratory, Lemont, 2014.
- [10] A. Röhrmoser, "Core Model of New german Neutron Source FRM II," *Nuclear Engineering and Design*, vol. 240, pp. 1417-1432, 2010.
- [11] P. Jain, "(Oak Ridge National Laboratory), private communication. Email sent to A. Bergeron July 23, 2019".
- [12] F. Thomas, "(Institut Laue-Langevin), private communication. Email sent to A. Bergeron July 19, 2019".
- [13] C. Reiter, "(Technical University of Munich), private communication. Email sent to A. Bergeron July 24, 2019".
- [14] Argonne National Laboratory, "Reduced Enrichment for Research and Test Reactors," [Online]. Available: <https://www.rertr.anl.gov/>. [Accessed 07 September 2021].
- [15] C. Bojanowski, A. Bergeron and J. Licht, "Experimental Validation of CFD Turbulent Models Relevant for Involute-Plate Reactors," in *RERTR 2018, 39th International Meeting on Reduced Enrichment for Research and Test Reactors*, Edinburg, Scotland, November 4-7, 2018.
- [16] A. Bergeron, C. Bojanowski, J. Licht, K. Shehu, C. Reiter, F. Thomas, Y. Calzavara, P. Jain and D. Chandler, "Involute Working Group – Progress towards Validation of CFD for Involute-Plate Reactors Safety Analysis," in *RERTR 2019, 40th International Meeting on Reduced Enrichment for Research and Test Reactors*, Zagreb, Croatia, October 6-10, 2019.
- [17] C. Bojanowski and A. Bergeron, "Influence of Multi-Dimension Heat Conduction on Heat Flux Calculation for HFIR LEU Analysis," ANL/RTR/TM-17/18, Argonne National Laboratory, Lemont, IL, 2017.
- [18] L. Prandtl, "Turbulent Flow, Technical Memorandums, National Advisory Committee for Aeronautics," No. 435, US Department of Commerce, Washington, 1927.

- [19] J. Nikuradse, "Untersuchungen uber turbulente Stromungen in nicht kreisformigen Rohren," *Ingr-Arch*, vol. 1, no. 3, p. 306, 1930.
- [20] E. Eckert and T. Irvine, "Flow in Corners of Passages With Non-Circular Cross Sections," *Trans. ASME*, vol. 78, no. 4, pp. 709-718, 1956.
- [21] E. Brundrett and W. Baines, "The Production and diffusion of vorticity in duct flow," *Journal of Fluid Mechanics*, vol. 19, no. 3, pp. 375-394, 1964.
- [22] F. Gessner, "The origin of secondary flow in turbulent flow along a corner," *J. Fluid Mech.*, vol. 58, no. 1, pp. 1-25, 1973.
- [23] L. Hoagland, "Fully Developed Turbulent Flow in straight Rectangular Ducts - Secondary Flow, Its Cause and Effect on the Primary Flow," Massachusetts Institute of Technology, Boston, MA, USA, 1960.
- [24] B. Launder and W. Ying, "Secondary flows in ducts of square cross-section," *Journal of Fluid Mechanics*, vol. 54, pp. 289-295, 1972.
- [25] H. Leutheuser, "Turbulent flow in rectangular ducts," *Journal of the Hydraulics Division*, vol. 89, 1963.
- [26] A. Melling and J. Whitelaw, "Turbulent flow in a rectangular duct," *Journal of Fluid Mechanics*, pp. 289-315, 1978.
- [27] C. Speziale, R. So and B. Younis, "On the Prediction of Turbulent Secondary Flows, 189772," National Aeronautics and Space Administration, Hampton, VA, USA, 1992.
- [28] B. Launder, G. Reece and W. Rodi, "Progress in the development of a Reynolds-stress turbulence closure," *Journal of Fluid Mechanics*, vol. 68, no. 3, pp. 537-566, 1975.
- [29] M. Hirota, H. Fujita, H. Yokosawa, H. Nakai and H. Itoh, "Turbulent heat transfer in a square duct," *International Journal of Heat and Fluid Flow*, vol. 18, pp. 170-180, 1997.
- [30] C. Alexopoulos, "Temperature and Velocity Distributions and Heat Transfer for Turbulent Air Flow in a Vertical Square Duct," University of Toronto, Toronto, Canada, 1964.
- [31] B. Launder and W. Ying, "Prediction of flow and heat transfer in ducts of square cross section," *Heat and Fluid Flow*, vol. 3, no. 2, pp. 115-121, 1973.
- [32] A. Melling, "Investigation of Flow in Non-Circular Ducts and Other Configurations by Laser Doppler Anemometry," London, 1975.
- [33] Siemens PLM Software, "Simcenter STAR-CCM+® Documentation, Version 2019.2," 2019.
- [34] D. Tatchell, "Convection process in confined three-dimensional boundary layers," University of London, London, 1975.
- [35] H. Fujita, M. Hirota and C. Nagata, "Fully Developed Turbulent Flow and Heat Transfer in a Square Duct with Two Roughened Facing Walls," *Chemical Engineering Communications*, vol. 74, pp. 95-110, 1988.
- [36] M. Hirota, H. Fujita and H. Yokosawa, "Experimental study on Convective Heat Transfer for Turbulent Flow in a Square Duct with a Ribbed Rough wall (Characteristics of Mean Temperature Field)," *Transactions of the ASME*, vol. 116, pp. 332-340, 1994.
- [37] H. Fujita, H. Yokosawa and M. Hirota, "Secondary Flow of the Second Kind in Rectangular Ducts with One Rough Wall," *Experimental Thermal and Fluid Science*, vol. 2, pp. 72-80, 1989.
- [38] E. Brundrett and R. Burroughs, "The temperature Inner-Law and Heat Transfer for Turbulent Air Flow in a Vertical Square Duct," *Int J. Heat Mass Transfer*, vol. 10, pp. 1133-1142, 1967.
- [39] W. Jones and B. Launder, "The Prediction of Laminarization with a Two-Equation Model of Turbulence," *Int. J. Heat and Mass Transfer*, vol. 15, pp. 301-314, 1972.

- [40] W. Rodi, "Experience with Two-Layer Models Combining the k- ϵ Model with a One-Equation Model Near the Wall," in *9th Aerospace Sciences Meeting, AIAA 91-0216*, Reno, NV, Jan. 7-10 1991.
- [41] F. Lien, W. Chen and M. Leschziner, "Low-Reynolds number eddy-viscosity modelling," in *Proc. 3rd Symp. on Engineering Turbulence Modelling and Measurements*, Crete, Grece, May 27-29, 1996.
- [42] T.-H. Shih, W. Shabbir, Yang Z. and J. Zhu, "A New k-epsilon Eddy Viscosity Model for High Reynolds Number Turbulent Flows - Model Development and Validation," NASA TM 106721, NASA, 1994.
- [43] D. Wilcox, *Turbulence Modeling for CFD*, 2nd edition, DCW Industries, Inc, 1998.
- [44] F. Menter, "Two-equation eddy-viscosity turbulence modeling for engineering applications," *AIAA Journal*, vol. 32, no. 8, pp. 1598-1605, 1994.
- [45] P. Spalart, "Strategies for turbulence modelling and simulations," *Int. J. of Heat and Fluid*, vol. 21, no. 3, pp. 252-263, 2000.
- [46] S. Wallin and A. Johansson, "An Explicit Algebraic Reynolds Stress Model for Incompressible," *J. Fluid Mechanics*, vol. 403, pp. 89-132, 2000.
- [47] A. Hellsten, "New Advanced k-omega Turbulence Model for High-Lift Aerodynamics," *AIAA Journal*, vol. 43, no. 9, pp. 1857-1869, 2005.
- [48] S. Sarkar and L. Balakrishnan, "Application of a Reynolds-stress turbulence model to the compressible shear layer," ICASE Report 90-18, NASA CR 182002, NASA, 1990.
- [49] R. Manceau and K. Hanjalic, "Elliptic blending model: A new near-wall Reynolds-stress," *Physics of Fluids*, vol. 14, p. 744, 2002.
- [50] S. Lardeau and R. Manceau, "Computations of Complex Flow Configurations Using a Modified Elliptic-Blending Reynolds-Stress Model," in *Proc. of the 10th Eng. Turb. Modelling and Measurement Conf.*, Marbella, Spain, 2014.
- [51] C. Speziale, S. Sarkar and T. Gatski, "Modelling the pressure-strain correlation of," *J. Fluid Mech.*, vol. 227, pp. 245-272, 1991.
- [52] National Institute of Standards and Technology, NIST, "NIST Chemistry WebBook, SRD 69," [Online]. Available: <https://webbook.nist.gov/chemistry/fluid/>. [Accessed 17 05 2021].
- [53] E. Lemmon and R. Jacobsen, "Viscosity and Thermal Conductivity Equations for Nitrogen, Oxygen, Argon, and Air," *International Journal of Thermophysics*, vol. 25, no. 1, pp. 21-69, 2004.
- [54] E. Brundrett and W. Baines, "The production and diffusion of vorticity in duct flow," *Journall of Fluid Mechanics*, no. 3, pp. 375-394, 1964.

APPENDIX A: References for the Used Turbulence Models

As explained in other sections of this report, the goal of the CFD analysis was to assess how well standard turbulence models are able to reproduce the experimental results for corner-type geometries. With modern CFD packages, like STAR-CCM+, users have the option to select many sub-models and options to fine-tune their turbulence models. In this appendix, the turbulence models used in this analysis are listed (see Table A.1) together with the relevant references describing these models.

Table A.1. List of turbulence models in STAR-CCM+ used in the present study.

Turbulence model	Symbol used in the report	Ability to model anisotropic effects	Reference list
Standard k-epsilon, two-layer model	SKE	No	[39], [40]
Standard k-epsilon with cubic terms, two-layer model	SKE-CUBIC	Yes	[41]
Realizable k-epsilon, two-layer model	RKE	No	[42]
Realizable k-epsilon with quadratic terms, two-layer model	RKE-QUAD	Yes	[41]
SST k-omega, two-layer model	KW	No	[43], [44]
SST k-omega quadratic constitutive relation, two-layer model	KW-QCR	Yes	[45]
SST k-omega cubic, two-layer model	KW-CUBIC	Yes	[46], [47]
Reynolds stress transport elliptic blending, two-layer model	RST-EB	Yes	[48], [49], [50]
Reynolds stress transport quadratic pressure-strain relation, high y^+ model	RST-QPS	Yes	[51]
Reynolds stress transport linear pressure-strain relation two layer, two-layer model	RST-LPS2L	Yes	[40]

APPENDIX B: Material Properties

B.1 Material Properties of Fuel and Cladding

The model of the generic fuel plate (Section 2) used two solid materials, one for fuel and one for cladding. The constants for these materials are listed in Table B.1.

Table B.1 Material constants for the fuel and cladding

Material constant	Fuel core	Aluminum cladding
Density (kg/m ³)	17,200.0	2,700.0
Specific heat (J/kg-K)	903.0	903.0
Thermal conductivity (W/m-K)	15.0	150.0

B.2 Material Properties of Water

Temperature-dependent material properties were used in the model of the generic fuel plate (Section 2). The density, dynamic viscosity, specific heat, and thermal conductivity of water were defined as polynomial functions of temperature with different orders of the polynomials as follows:

$$\rho = \sum_{k=0}^{m_i} a_{i,k} T^{b_{i,k}} ; (Tr \leq T \leq Tr_{i+1}) \quad (B.1)$$

These polynomials were generated from the water properties found in [52]. In Table B.2, these quantities are defined in the following manner: the second column denotes the number of components, the third one denotes the temperature range for which the dependency is defined, the fourth one contains all the coefficients for the polynomial, and the fifth one contains the exponents of temperature associated with the coefficients. The entire function may be built of several polynomials defined for different ranges of temperature according to Equation B.1. Figure B.1 to Figure B.4 show these properties of coolant in the form of plots.

Table B.2. Properties of coolant.

	# of polynomial coefficients	Temperature range (K)	Coefficients	Exponents
Dynamic viscosity [Pa-s]	7	273, 450	6.118072E-16, -1.399347E-12, 1.330595E-9, -6.735074E-7, 1.914979E-4, -0.02902184, 1.833873	6, 5, 4, 3, 2, 1, 0
Density [kg/m ³]	5	273, 450	-4.72297E-8, 7.403817E-5, -0.04562428, 12.21753, -178.6494	4, 3, 2, 1, 0
Specific heat [J/kg-K]	6	273, 450	-5.537245E-9, 1.062099E-5, -0.008063263, 3.040666, -570.526, 46809.37	5, 4, 3, 2, 1, 0
Thermal conductivity [W/m-K]	4	273, 450	1.875566E-8, -2.772204E-5, 0.01319425, -1.358133	3, 2, 1, 0

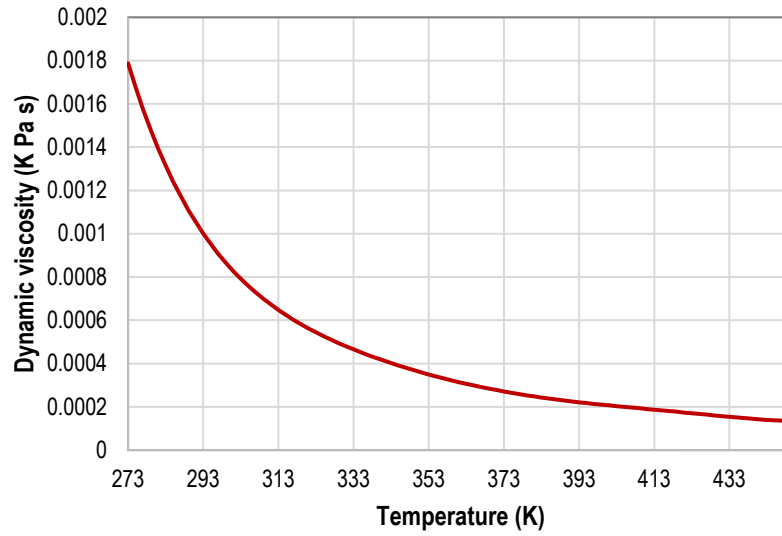


Figure B.1. Dynamic viscosity of water as a function of temperature.

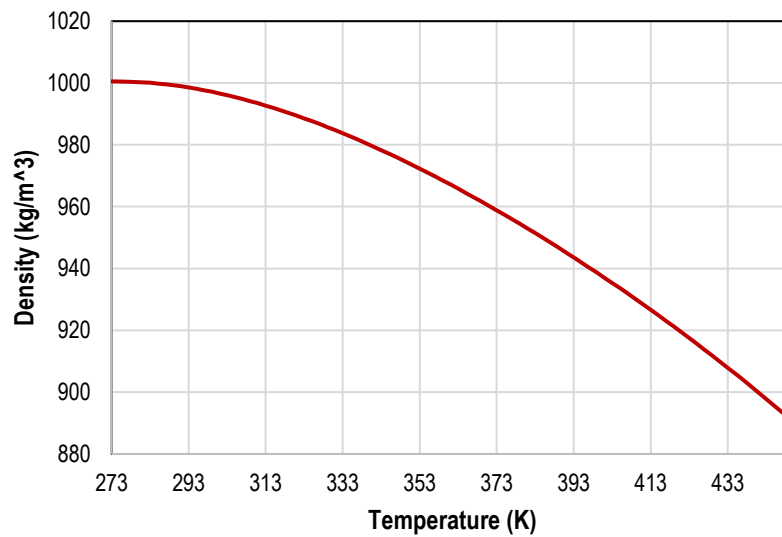


Figure B.2. Density of water as a function of temperature.

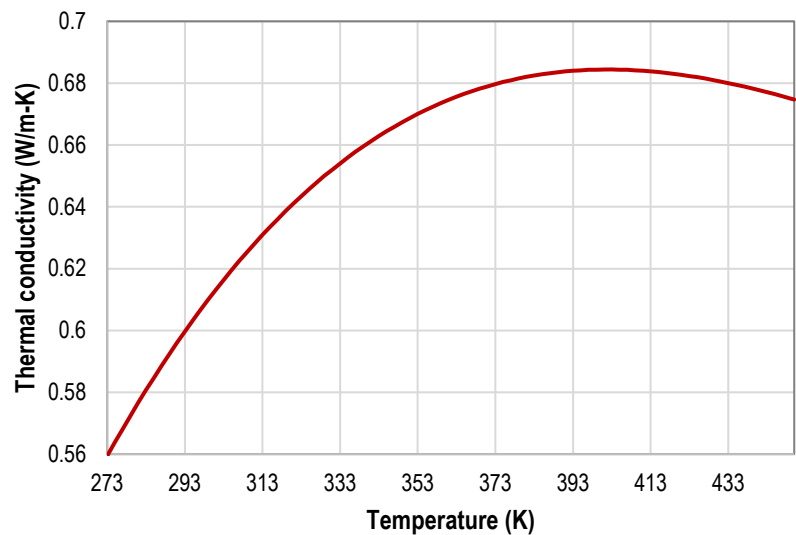


Figure B.3. Thermal conductivity of water as a function of temperature.

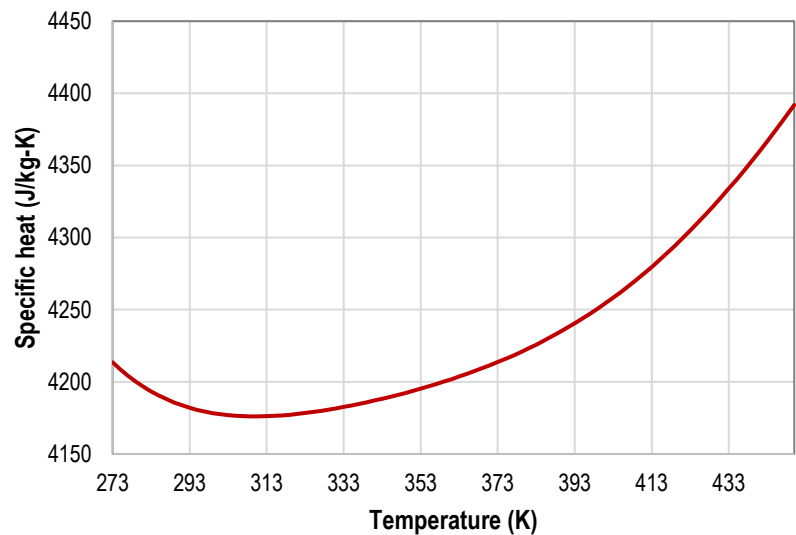


Figure B.4. Specific heat of water as a function of temperature.

B.3 Material Properties of Air

The temperature-dependent properties of air were used in the modeling of Hirota et al.'s experiment, discussed in Section 5. The data gathered here (Figures B.5 through B.8) are based on [53]. In the studied range of temperatures, between room temperature and 100 °C at a pressure of 1 bar, these quantities can be approximated with linear functions.

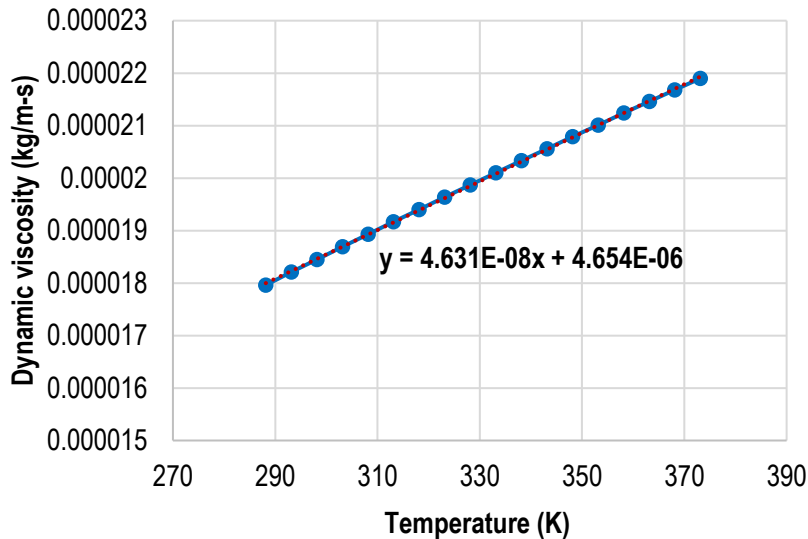


Figure B.5. Dynamic viscosity of air as a function of temperature.

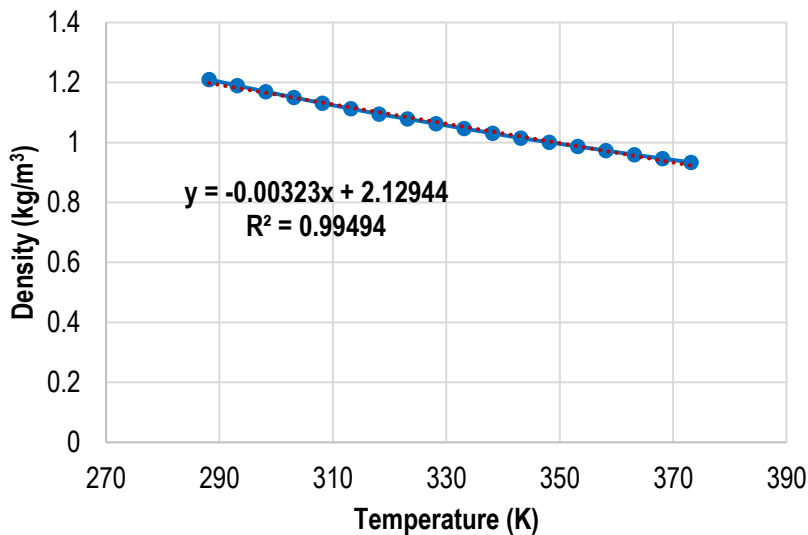


Figure B.6. Density of air as a function of temperature.

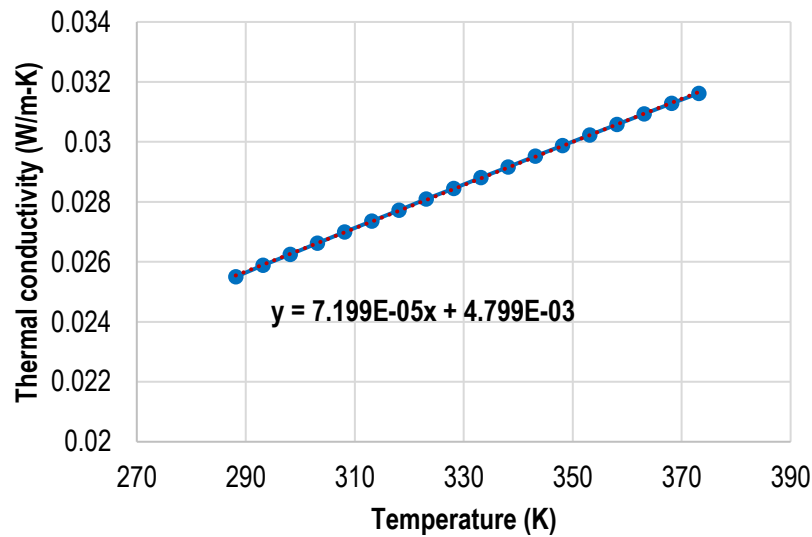


Figure B.7. Thermal conductivity of air as a function of temperature.

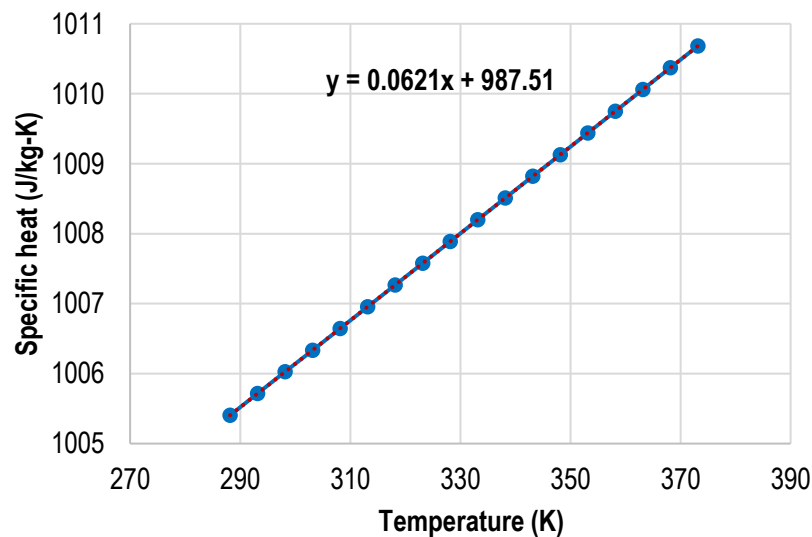


Figure B.8. Specific heat of air as a function of temperature.



Nuclear Science & Engineering Division

Argonne National Laboratory
9700 South Cass Avenue, Bldg. 208
Argonne, IL 60439

www.anl.gov



Argonne National Laboratory is a U.S. Department of Energy
laboratory managed by UChicago Argonne, LLC